

The upper crustal microseismicity image from the North Chilean subduction zone: implications for tectonics and fluid migration

Dissertation
zur Erlangung des Doktorgrades
der Naturwissenschaften
am Fachbereich Geowissenschaften
der Freien Universität Berlin

vorgelegt von

Pablo Salazar Reinoso

Berlin, 2011

Erster Gutachter: Prof. Dr. Serge Shapiro
Zweiter Gutachter: Priv. Doz. Dr. Günter Asch
Tag der Disputation: 05.07.2011

Erklärung

Hiermit versichere ich, daß ich die vorliegende Arbeit selbständig verfaßt und keine anderen als die angegebenen Hilfsmittel benutzt habe. Die Stellen der Arbeit, die anderen Werken wörtlich oder inhaltlich entnommen sind, wurden durch entsprechende Angaben der Quellen kenntlich gemacht.

Diese Arbeit hat in gleicher oder ähnlicher Form noch keiner Prüfungsbehörde vorgelegen.

Abstract

In November 2005, a temporary short-period seismic network was installed in the Chilean Precordillera, around 21°S. This set of twelve 3-component stations that form the West Fissure seismological network has been recording continuously since then, however, only the crustal microseismicity data recorded during the years 2005-2009 were processed and analyzed here.

Thus, the microseismicity studies in the forearc of the north Chilean subduction have permitted the retrieval of important tectonic features of the crust. A new image of the crustal structure and the West Fissure Fault System (WFFS) as a westward-dipping compressive structure, geometrically opposed to Nazca plate subduction, has been constrained by microseismicity.

The origin of this particular geometry is not clearly defined yet, but this could be a tectonic response to differences in the rheological behavior of the crust.

The characterization of this structure, in terms of its stress distribution and kinematics, has been obtained by a good fit with some deeper focal mechanisms and also through stress tensor analysis in the zone.

The stress tensor analysis also shows that the state of stress in the convergence margin is related to compression, whereas the extension is only a manifestation of local forces associated with the highest areas in the Andes.

Two seismic clusters have also been identified and possibly associated with a blind branch of WFFS. The study of these two clusters with a focus on their sources and possible connection with fluid migration was carried out.

It is observed that some characteristics of the two clusters found in the zone differ from each other. The central cluster has characteristics of an earthquake swarm with two phases which can clearly be identified, whereas the SW cluster has a clear main shock associated and can be separated into two subclusters (A and A', respectively).

In contrast, the similarities permit to infer that they could have a common origin. The b -values for both are characteristic of tectonic plate boundaries. The spatial spreading of the events –which is approximately confined to one plane– reveals a progressively growing of the main fracture that form the

swarm and subcluster A activities. It is also found that earthquakes themselves trigger aftershocks near the border of their rupture areas.

In addition, the spatio-temporal migration of hypocenters, as well as, spatial correlation –with areas that were interpreted as fluid migration zones– lead to believe that there is a close relation between fluids and the sources of the swarm and subcluster A.

These observations above, point to think in a stick-slip behavior of the rupture propagation, which can be explained by stress transfers and induced fluid flows due to earthquakes in a fluid-permeated critically loaded fault zone.

Zusammenfassung

Im November 2005 wurde in der chilenischen Präkordillere bei 21 Grad südlicher Breite ein temporäres, kurz-periodisches, seismisches Stationsnetz installiert. Dieses Netz mit zwölf 3-Komponenten Seismometern, die das „West Fissure seismological network“ bilden, haben seit dem kontinuierlich aufgezeichnet. Für diese Arbeit wurden die Daten krustaler mikroseismischer Ereignisse der Jahre 2005 bis 2009 prozessiert und analysiert.

Die Mikroseismizitätsstudien im „Fore-Arc“ über der Subduktionszone im Norden Chiles haben zur Entdeckung wichtiger tektonischer Eigenschaften der Kruste geführt. Durch die Lokalisierung der Mikroseismizität ergibt sich ein neues Bild für die Struktur der Kruste und das West Fissure Fault System (WFFS) als eine nach Westen gerichtete Kompressionsstruktur, die der Nazca-Platte geometrisch entgegensteht.

Die Ursache dieser speziellen Geometrie ist noch nicht genau klar, es könnte sich jedoch um die tektonische Antwort auf Unterschiede im rheologischen Verhalten der Kruste handeln.

Die Eigenschaften dieser Struktur hinsichtlich der Spannungsverteilung und der Kinematik wurden durch eine geeignete Anpassung der Herdmechanismen von tiefer liegenden Ereignissen sowie durch Spannungstensor-Analysen in dem Gebiet erlangt.

Die Spannungstensor-Analyse verdeutlicht zudem, dass der Spannungszustand am konvergenten Plattenrand mit Kompression verbunden ist, während es sich im Falle der Dehnung lediglich um eine Manifestation von lokalen Kräften handelt, die mit den höchsten Gebieten in den Anden verbunden sind.

Zudem wurden zwei seismische Cluster entdeckt, die möglicherweise mit einem blinden Ausläufer des WFFS verbunden sein könnten. Es wurde eine Analyse dieser beiden Cluster mit dem Schwerpunkt auf deren Ursprung sowie auf deren mögliche Verbindung mit Fluidmigrationen durchgeführt.

Dabei wurde beobachtet, dass sich einige Eigenschaften der beiden in dem Gebiet entdeckten Cluster unterscheiden. Der zentrale Cluster weist Eigenschaften eines Erdbebenschwarms mit zwei Phasen auf, während dem

SW-Cluster ein Hauptbeben zugeordnet werden kann. Dieser Cluster kann in zwei Subcluster aufgeteilt werden.

Demgegenüber lassen die Ähnlichkeiten darauf schließen, dass sie einen gemeinsamen Ursprung haben. Für die Ereignisse beider Cluster ergeben sich b -Werte, die für die Ränder tektonischer Platten charakteristisch sind. Die räumliche Verteilung der Ereignisse – welche ungefähr auf eine Ebene begrenzt ist – zeigt ein zunehmendes Anwachsen der Hauptfrakturen, welche zum Bebenschwarm oder zu den Aktivitäten des Subclusters A führen. Es wurde zudem festgestellt, dass Erdbeben selbst, in der Nähe der Grenze ihrer Bruchzone, Nachbeben auslösen.

Zudem führt die raumzeitliche Migration von Erdbebenherden sowie die räumliche Korrelation – mit Gebieten, die als Gebiete mit Fluidmigration bewertet wurden – zu der Annahme, dass es eine enge Beziehung zwischen Fluiden und den Ursachen Quellen für den Schwarm und das Subcluster A gibt.

Diese oben genannten Beobachtungen deuten darauf hin, dass es sich bei der Bruchverbreitung um ein „Stick-Slip“-Verhalten handelt, das durch Stress-Übertragungen und induzierte Flüssigkeitsströme aufgrund von Erdbeben in einer von Flüssigkeit durchdrungenen, kritisch geladenen Störungszone erklärt werden kann.

Resumen

En Noviembre de 2005 fue instalada una red sismológica temporal en la Precordillera Chilena alrededor de los 21°S. Este conjunto de doce estaciones de tres componentes forman parte de la red sismológica de la Falla Oeste, la cual ha estado registrando continuamente desde entonces. Sin embargo, solamente los datos de microsismicidad cortical registrados durante los años 2005-2009 fueron procesados y analizados en este estudio.

De esta manera, los estudios de microsismicidad en el antearco de la zona de subducción del norte de Chile han permitido establecer importantes rasgos tectónicos de la corteza. Así ha sido definida mediante microsismicidad una nueva imagen de la estructura de la corteza y del sistema Falla Oeste (WFFS), la cual correspondería a una estructura compresiva manteniendo hacia el occidente, geoméricamente opuesta a la subducción de la placa de Nazca.

El origen de esta particular geometría aun no está claro, pero podría corresponder a una respuesta tectónica a las diferencias en el comportamiento reológico de la corteza.

La caracterización de esta estructura, en términos de su distribución de stress y cinemática, ha sido obtenida por la buena correspondencia con algunos mecanismos focales de eventos profundos y también a través del análisis del tensor de stress en la zona.

El análisis del tensor de stress también mostró que el estado de stress en el margen convergente está relacionado con compresión, mientras que la extensión es solamente una manifestación de fuerzas locales asociadas con las áreas más altas de los Andes.

Dos clusters sísmicos han sido identificados y posiblemente asociados con ramales no expuestos de la WFFS. El estudio de estos dos clusters fue conducido con un énfasis en sus fuentes y posible conexión con migración de fluidos.

Se observa que algunas características de los dos clusters encontrados en la zona difieren del uno al otro. El cluster central tiene características de un enjambre sísmico, con dos fases que se pueden diferenciar claramente,

mientras que el cluster SW tiene asociado un claro evento principal, el cual puede ser separado dentro de dos subclusters (A y A'), respectivamente.

Al contrario, las similitudes permiten inferir que ellos pudieron tener un origen en común. Los valores b para ambos son característicos de límites de placas tectónicas. La dispersión espacial de los eventos, la cual es confinada a un plano, revela un progresivo crecimiento de la fractura principal que forman las actividades del enjambre y del subcluster A. Además es posible determinar que los terremotos mismos gatillan réplicas cerca del borde de sus áreas de ruptura.

Adicionalmente, la migración espacio-temporal de los hipocentros, como también la correlación espacial –con áreas interpretadas como zonas con migración de fluidos– conduce a creer que hay una relación estrecha entre los fluidos y las fuentes del enjambre y el subcluster A.

Estas observaciones anteriores, apuntan a pensar en un comportamiento stick-slip de la propagación de la ruptura, la cual podría ser explicada por transferencia de stress y la inducción de fluidos debido a terremotos en una zona de falla permeable y críticamente cargada.

Contents

List of Figures	iii
List of Tables	vi
1 Introduction	1
1.1 The problem	1
1.2 The scientific questions	2
1.3 Hypothesis	3
1.4 State of investigations	3
1.5 A brief overview of this study	4
2 Geotectonic setting	6
2.1 The Andean convergence system	6
2.2 Central Andes	9
2.3 The Altiplano segment	11
2.3.1 Forearc	11
2.3.2 Arc, backarc and foreland	11
2.3.3 Deformation and uplift of the Altiplano Plateau	13
2.4 West Fissure Fault System	15
3 Theoretical background of the methods used	17
3.1 Precise location technique NonLinLoc	17
3.2 Local magnitude determination	19
3.3 Focal mechanisms	19
3.3.1 Introduction	19
3.3.2 First-motion of P -waves	20
3.3.3 Amplitude ratios	21
3.4 Stress tensor analysis	23
3.5 Moment tensor analysis	24
3.6 Spectral analysis	26
3.6.1 Determination of M_0 and M_W	28
3.7 Frequency-magnitude distribution	28

3.8	Interevent-time distribution	29
3.9	Principal Components Analysis	31
3.10	3D rotation matrix	33
3.11	Spatiotemporal analysis	34
3.12	Spatiotemporal migration	35
4	Results-characterization of the West Fissure Fault System	36
4.1	Experiment set-up and data	36
4.2	The observed seismicity	40
4.3	Focal mechanisms-data processing and results	47
4.4	Stress tensors	51
4.5	Moment tensor analysis	57
4.6	Discussion of the results and comparison with other studies . .	69
5	Detecting possible fluid signals from the clusters	78
5.1	Introduction to the cluster analysis	78
5.2	Data	78
5.3	Chronological evolution of the energy release in the clusters . .	80
5.4	Statistical characteristics	82
5.4.1	Frequency-magnitude distribution	82
5.4.2	Interevent-time distribution	82
5.5	Spatial analysis	85
5.6	Spatiotemporal analysis	88
5.7	Spatiotemporal migration	94
5.8	Discussion of the results and the different clusterization models	95
5.8.1	Intrinsic differences in the earthquake clusterization . .	95
5.8.2	Mainshock-aftershock model	96
5.8.3	Ambiguities of the mainshock-aftershock model	96
5.8.4	Stick-slip model	97
5.8.5	The proposed model	98
5.8.6	Other geophysical anomalies taken in consideration . .	98
6	Conclusions	103
6.1	Tectonic implications	103
6.2	Fluid migration implications	104
	Bibliography	107
A	Focal mechanisms parameters	125
A.1	Events used in the stress tensor analysis	125
B	Location parameters	132

B.1	Events used in the swarm analysis	132
B.2	Events used in the subcluster A analysis	135
B.3	Events used in the subcluster A' analysis	139
C	Acknowledgments	141
D	Curriculum Vitae	143

List of Figures

2.1	Geotectonic setting of South America	7
2.2	Geotectonic framework of the Central Andean convergence system	9
2.3	The Altiplano segment	12
2.4	Magnitudes of crustal shortening along the Central Andes	14
2.5	The two large scale margin-parallel shear zones	16
3.1	P and S wave radiation pattern of a double couple source	20
3.2	Focal sphere of an earthquake source	21
3.3	Element of a fault plane solution	22
3.4	Schematic illustration of the data analysis scheme for two successive earthquakes	34
4.1	Local short period network around the West Fissure Fault System	37
4.2	The 2-D P -velocity model	39
4.3	Register for a shallow event	40
4.4	Register for a deeper event	41
4.5	Normalized density of event per day	42
4.6	Local seismicity around the West Fissure Fault System	42
4.7	The magnitude of the clusters is shown as a function of time	45
4.8	The correlations coefficients for the central cluster (Swarm).	46
4.9	An example of waveform similarity for the central cluster (Swarm).	46
4.10	An example of hand-picked P and S arrivals using SEISAN	47
4.11	An example of rotation of seismograms using SEISAN	48
4.12	Calculation of the focal mechanism using SEISAN	49
4.13	Focal mechanism results	49

4.14	Zones included in the stress tensor calculation	52
4.15	Regional stress tensor	52
4.16	Stress tensor for NW subarea	53
4.17	Stress tensor for the SW subarea	54
4.18	Stress tensor for the swarm subarea	55
4.19	Stress tensor for the SE subarea	55
4.20	Stress tensor for the NE subarea	56
4.21	Stress Tensor results	56
4.22	The velocity model used for inversion.	58
4.23	Grid search for moment tensor inversion in the swarm	60
4.24	Plot of depth vs correlation for the swarm	60
4.25	Grid search for moment tensor inversion in the subcluster A	61
4.26	Plot of depth vs correlation for the subcluster A	61
4.27	Comparison between the observed (black) and synthetic (red) seismograms for the stations T06, T04, T18 and T08 in the case of swarm.	62
4.28	Comparison between the observed (black) and synthetic (red) seismograms for the stations T17, T07, T10 and T15 in the case of swarm.	63
4.29	Comparison between the observed (black) and synthetic (red) seismograms for the stations T05, T20 and T19 in the case of swarm.	64
4.30	Comparison between the observed (black) and synthetic (red) seismograms for the stations T05, T20, T08 and T04 in the case of subcluster A.	65
4.31	Comparison between the observed (black) and synthetic (red) seismograms for the station T19 in the case of subcluster A.	66
4.32	Moment tensor solutions, (a) swarm and (b) subcluster A	67
4.33	The polarities of the P -wave first arrival are superimposed on the moment tensor solutions (a) swarm and (b) subcluster A	68
4.34	Local seismicity map	70
4.35	Seismicity profiles	71
4.36	Local seismicity around 23°S	72
4.37	Strain model in the Central Andes	73
4.38	Present-day tectonic regime	74
4.39	Stress tensor for the volcanic arc	75
4.40	Tectonic model	77
5.1	The magnitudes of the clusters is shown as a function of time	79
5.2	The energy evolution of the swarm as a function of earthquake index.	80

5.3	The energy evolution of the subcluster A as a function of earthquake index	81
5.4	The cumulative frequency-magnitude distribution with their b-values for (a) two phases of swarm, (b) subcluster A, and (c) subcluster A'.	83
5.5	The interevent-time probability distribution	84
5.6	The positions of the hypocenters and the fitted fault plane in three dimensional space	86
5.7	The distribution of the x-, y-, and z-values of the all hypocenters in the transformed coordinate system	87
5.8	The evolution of the area A as a function of the time relative to its initiation	88
5.9	Rupture activity of the swarm	90
5.10	Rupture activity of the subcluster A	91
5.11	The rate of foreshocks and aftershocks is shown as a function of the time for the master shock	92
5.12	The density of aftershocks activity is plotted as a function of distance to the master shock	93
5.13	Hypocenter distances measured from the first event as a function of the earthquake occurrence times	94
5.14	Reflectivity anomaly zone related to subclusters A and A'	99
5.15	Role of the fluids with respect to local seismicity and reflectivity	100
5.16	Resistivity anomaly related to swarm	102

List of Tables

4.1	List of stations of the WFFS experiment	36
4.2	Configuration of record parameters in the stations	38
4.3	Calibration parameters for WFFS stations	40
4.4	List of the parameters describing the stress tensor solutions . .	53
4.5	Precise location by NonLinLoc method	57
4.6	1D velocity model used for inversion	58
4.7	Moment tensor solutions	68
A.1	List of 228 focal mechanisms used in the stress tensor analysis	125
B.1	List of 90 events used in the swarm analysis	132
B.2	List of 182 events used in the subcluster A analysis	135
B.3	List of 38 events used in the subcluster A' analysis	139

Chapter 1

Introduction

1.1 The problem

Since the Lower Jurassic (~ 200 Ma, Andean cycle, *Coira et al.* [1982]) the Pacific coast of the South American continent has been subjected to active tectonism. Deformation has been caused by the subduction of the Pacific Nazca plate below South America. Plate convergence along the Central Andes trends NE to ENE with a moderate slab dip between 25 and 30° at a rate of 74.4 mm/yr [*Angermann et al.*, 1999]. The direction and magnitude of the kinematic plate vector changed, leading to distinct deformation stages through time [*Scheuber et al.*, 1994].

The forearc portion between the coast and the Main Cordillera is built from several major NS-directed strike-slip fault zones which have resulted from oblique collision [*Beck*, 1983; *Reutter et al.*, 1991]. These show Neogene to recent active strands resulting in significant local topography.

Deformation in the Coastal Cordillera is dominated by the Atacama Fault System (AFS) with an along strike extent of more than 1000 km. Young normal faulting producing fresh scarps marking E-W extension has been recognized in several areas along strike [e.g., *Gonzalez et al.*, 2006], in cases identified as associated with the 1995 Antofagasta earthquake or recent crustal seismicity recorded between $22.5 - 24^\circ\text{S}$ [*Comte et al.*, 1992].

Recent activity of the orogen parallel Precordillera Fault System (PFS) [*Scheuber and Reutter*, 1992] is reported to be dominated by NW-SE directed extension indicated by normal faulting along NE-SW trending normal faults along with dextral reactivation of the PFS between $20 - 21^\circ\text{S}$ [*Victor et al.*, 2004]. The West Vergent Thrust System (WVTS) located at the foot of the Precordillera is responsible for plateau uplift since the late Oligocene [*Victor et al.*, 2004].

Due to the fact that these large fault zones can generally be traced for several hundreds or even thousands of kilometres it is believed that they extend through the lithosphere [Sylvester, 1988].

Recent studies in the zone focus on the intermediate-depth seismicity associated with the subduction of the Nazca Plate beneath the South American Plate [e.g., *Haberland and Rietbrock*, 2001; *Heit*, 2005], the $M_W = 7.7$ Tarapacá earthquake on 13 June, 2005 [*Peyrat et al.*, 2006], the $M_W = 6.3$ Aroma earthquake on 24 July, 2001 [*Legrand et al.*, 2007], intracontinental seismicity associated to Central Andes Orocline [*David*, 2007] and tectonics evidence of the western Altiplano plateau [e.g., *Janssen et al.*, 2002; *Victor et al.*, 2004; *Farías et al.*, 2005].

Nevertheless, in spite of the geological, tectonic and economic importance very little is known about the seismic activity and the continuation to greater depth of these large tectonic structures. A more enigmatic topic is the role that these structures play in the ascent of fluids toward the upper crust.

1.2 The scientific questions

The scientific questions which are addressed in this thesis have relation with the behaviour of the forearc crust in the Altiplano segment of the Nazca-South America convergence margin. Thus the main question posed here exposes the problem related to the Precordillera Fault System which, since can be traced for thousands of kilometers, why does not it have, until now, any clear geophysical description that represent this huge tectonic structure in depth? Other more specific aspects that have relation with the main question exposed above are:

- Does the West Fissure Fault System (WFFS) extend through all lithosphere?
- How is the present seismic activity distributed around the WFFS?
- Is the stress field, related to the convergence, strongly changed when it is transferred to the upper crust?
- Is it possible to detect, in our data, seismic signals related to fluid migration?

1.3 Hypothesis

Earlier studies exposed numerous geological and seismological evidence that the Precordillera Fault System (PFS) has been active since Late Eocene/Early Oligocene to recent [David, 2007; Victor *et al.*, 2004; Farías *et al.*, 2005; Reutter *et al.*, 1996]. Therefore it is reasonable to think that this fault system can generate seismic activity which permits to obtain a passive seismic image in depth.

In addition, if we have in consideration the huge structural system that PFS represents in surface, it must be a tectonic feature extended through at least part or all the lithosphere, playing an important role in the stress transfer from the subducted Nazca plate to the upper crust, which could be manifested in the stress field associated to the forearc region.

On the other hand, the large history of the hydrothermal activity registered [Ossandón *et al.*, 2001] and the hot spring centers associated to this structural system (e.g., Maniña, Pica, Macaya, Chusmiza, etc.) give an idea that the PFS would be used as a fluid pathway toward the upper crust.

There are numerous studies that implemented sophisticated techniques in order to recorded a seismic pattern related to fluid migration, therefore, if the PFS is a fluid pathway perhaps it is possible to obtain this pattern of our seismic records and validate this assumption.

1.4 State of investigations

The Central Andes through its history have passed for various stages of extension, compression and transtension, these stages alternated with period of tectonic inactivity [Reutter *et al.*, 1988; Scheuber *et al.*, 1994; Sempere *et al.*, 1997]. During the Paleogene, the actual configuration of the central part of the Andes began to take form due to compression related to the subduction between Nazca and South American plates [Pilger, 1981, 1983; Pardo-Casas and Molnar, 1987].

The processes involved in the creation of the elevated plateau called Altiplano include crustal shortening, variable thickness in the crust, and different dipping angles of the subducting plate along the strike [Schmitz, 1994; Allmendinger *et al.*, 1997; Kley and Monaldi, 1998; Riller *et al.*, 2001; Riller and Oncken, 2002].

Several geophysical anomalies have been found below the Altiplano plateau as the presence of a low velocity zone (LVZ) in the upper crust [Wigger *et al.*, 1994; Yuan *et al.*, 2000, 2002], the Quebrada Blanca bright spot (QBBS) [ANCORP Working Group, 1999, 2003], and attenuation tomogra-

phy anomalies that were interpreted as possible delaminated portions of the lithosphere by *Schurr* [2000]; *Schurr et al.* [2003]. All of these anomalies have been considered by many studies which try to resolve the internal structure of the Andean plateau [*Haberland and Rietbrock*, 2001; *Victor et al.*, 2004; *Elger et al.*, 2005; *Scheuber et al.*, 2006].

Despite all these studies, many other processes are not well-understood yet and these continue to be the subject of research as the investigations which refer to the differences in constitution, tectonic shortening, topography and thickness of the crust, differences in volcanism and magmatism [*Allmendinger et al.*, 1997].

The major enigma is related to the generation of a plateau in the absence of a collision scheme [*Isacks*, 1988; *Reutter et al.*, 1988; *Allmendinger and Gubbels*, 1996]. Thus, since 1980, a series of seismological projects were conducted in order to understand the interaction of the geologic-geodynamical processes in the Central Andes [e.g., *Wigger et al.*, 1994; *Patzwahl et al.*, 1999; *Schmitz et al.*, 1999; *ANCORP Working Group*, 1999, 2003; *Graeber and Asch*, 1999; *Haberland and Rietbrock*, 2001; *Schurr et al.*, 1999; *Bock et al.*, 2000].

The identification of deep structures in the crust as well as the depth and topography of the Moho discontinuity have been provided by passive and active seismic experiments [*Beck et al.*, 1996; *Zandt et al.*, 1996; *Yuan et al.*, 2000].

On the other hand, the electrical anomalies have shown conductive materials in the area of the plateau [*Brasse et al.*, 2002] which would be associated to the processes of melting and volcanic activity in the zone. These processes have been correlated to the earthquake clusters of the subducted slab [*Schilling et al.*, 1997]. Thus, the dehydration and metamorphism of the subducted slab would be responsible for the generation of magmas and movement of fluids which would trigger seismic activity in the crust.

1.5 A brief overview of this study

The present work focus on to generate a seismic image of the North Chilean upper plate in order to understand the tectonics and fluid migration processes in the forearc region. Thus, the main topics treated here correspond to a tectonic characterization of the West Fissure Fault System and the study of the sources of seismic clusters associated to it, which –in first approximation– are correlated with fluid migration processes.

The thesis is organized in six chapters which are described as follows:

Chapter 2 gives an overview of the geotectonic setting of the Andes,

describing the Central Andes, the Altiplano segment and finally the West Fissure Fault System including its geodynamical environment, tectonics and magmatics characteristics.

In chapter 3 the theoretical background of the different methods used in this work is briefly described.

Chapter 4 describes the seismic experiment set-up and the data processing used in order to obtain an image of the seismicity in the study area. Also a characterization of the West Fissure Fault System in term of the seismicity and its kinematic behaviour is made. Here is implemented a stress field analysis based on the focal mechanisms and a moment tensor analysis of the largest event in the swarm and subcluster. The results are discussed and compared to previous results obtained around the study area.

Chapter 5 refers to several tests implemented in order to retrieve a seismic signal that permits us to understand the origin of the earthquake clusterization. The starting assumption is that these clusters were triggered by fluids and, therefore, all tests applied to the data will try to validate or dismiss this hypothesis. Thus, a chronological evolution of the energy release, moment tensor, statistical, spatial, and spatiotemporal migration analyses were performed. The last part of the chapter consists of a discussion of the results and a comparison to other studies in the area.

Chapter 6 resumes all the results and conclusions that were obtained by the analysis of this passive seismic image of the crust. They focus on the implications that the microseismicity has had in the tectonic and fluid migration processes in the crust and how the study of them can contribute to the better understanding of the stress transfer and the fluid migration phenomena and their role in the triggering of seismic activity.

Chapter 2

Geotectonic setting

2.1 The Andean convergence system

The western margin of South America is one of the largest and most active plate boundary zones. Here, the oceanic Nazca plate moves at a rate of 37.7 mm/yr to the east, while the South American continent overrides it at 36.7 mm/yr westwards with respect to a point in the Eastern Cordillera [Marret and Strecker, 2000]. This results in a slightly oblique ENE directed convergence between the two plates with a velocity of 74.4 mm/yr.

The Andes are located along this border and stretch over about 8000 km from Caribbean to Tierra del Fuego along the western margin of South America (Figure 2.1). This is characterized by the oroclinal bending of the Altiplano-Puna plateau (after Tibet, the world's second largest continental plateau).

The Andes can be subdivided into the northern, central, and southern Andes according to the active volcanic regions (northern, central and south volcanic regions).

The limits of these segments roughly correlate with the subduction of buoyant oceanic ridges (Carnegie, Nazca, Juan Fernández) that partially control the shape of the subducted slab and therefore the location of active volcanic arcs [Jordan *et al.*, 1983; Gutscher *et al.*, 2000]. Slab segments dipping more than 25° favour melting of the asthenospheric wedge that feeds the volcanic zones [Tassara *et al.*, 2007]. Volcanic gaps between them are younger than 10 Ma [Mpodozis and Ramos, 1989; Ramos, 1999] and associated with sub-horizontal, flat segments of the slab at 100-150 km depth [Cahill and Isacks, 1992] that preclude mantle magmagenesis.

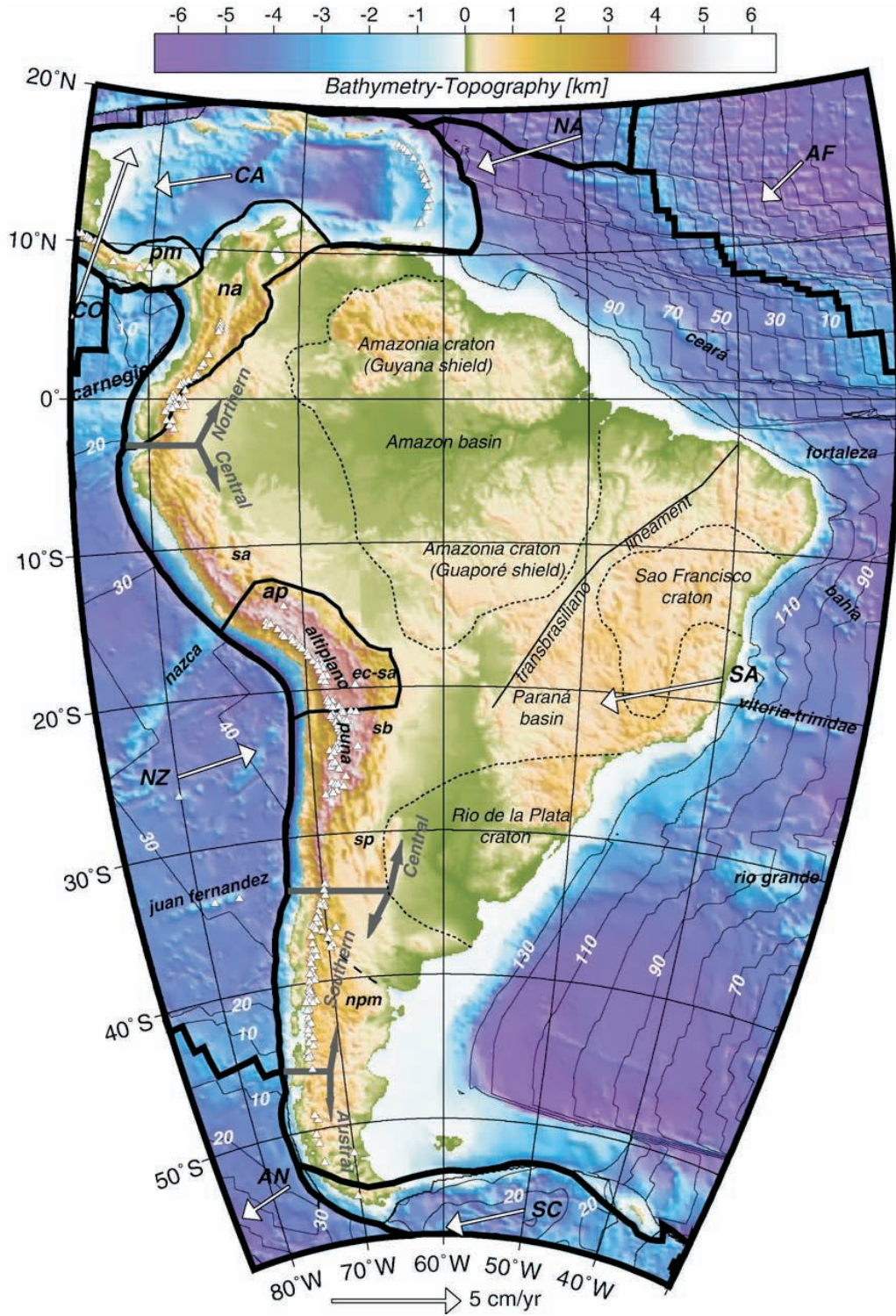
Spreading centers that separate the Nazca plate from the Cocos and Antarctic plates, currently subduct near the northern and southern limbs

of the Andean trench. Therefore, the age of the Nazca plate at the trench increases toward the Central Andes, reaching a maximum of 45 Ma [Müller *et al.*, 1997].

The Andean Cordillera is the classic example of a mountain chain formed during the subduction of an oceanic slab under a continental plate. This mountain chain rises from an over 8000 m deep deep-sea-trench to almost 7000 m high peaks, their relief is the highest on earth.

The origin of this mountain belt is attributed to contractional strain related to almost uninterrupted subduction since the Jurassic along the western margin of South America [Fariás *et al.*, 2005; Baby *et al.*, 1997; Coira *et al.*, 1982; Jordan *et al.*, 1983; Kay and Abbruzzi, 1996; Kay *et al.*, 1991, 1999; Mpodozis and Ramos, 1989; Ramos, 1988; Sempere *et al.*, 1990]. Thus, the significant westward acceleration of South America after opening of the Atlantic caused the onset of compressive deformation along its convergent margin that continues during the Cenozoic to form the Andes [Ramos, 1999].

Figure 2.1 (on the next page): Geotectonic setting of South America [from *Tassara et al.*, 2007]. Thick and thin lines are boundaries of large (SA, South America; CA, Caribbean; NA, North America; AF, Africa; SC, Scotia; AN, Antarctica; NZ, Nazca; CO, Cocos) and small (pm, Panama; na, Northern Andes; ap, Altiplano) tectonic plates from model PB2002 [Bird, 2003]. Arrows depict vectors of plate motion with respect to the hotspot reference frame from model HS3-NUVELIA [Gripp and Gordon, 2002] as calculated at the given position with the Plate Motion Calculator. Diverging grey arrows shows boundaries and names of Andean segments. Dotted lines mark the extent of Achaean to Early Proterozoic cratons [Cordani and Sato, 1999; Kröner and Cordani, 2003]. The dashed line oblique to the Southern Andes marks the northern limit of the Patagonian terrain. Over the oceans, thin lines with white numbers mark isochrons of the oceanic lithosphere [Müller *et al.*, 1997] and names depict major oceanic ridges. Some Andean morphotectonic units are highlighted; Sierras Subandinas (sa), Eastern Cordillera (ec), Santa Barbara System (sb), Sierras Pampeanas (sp), North Patagonian Massif (npm).

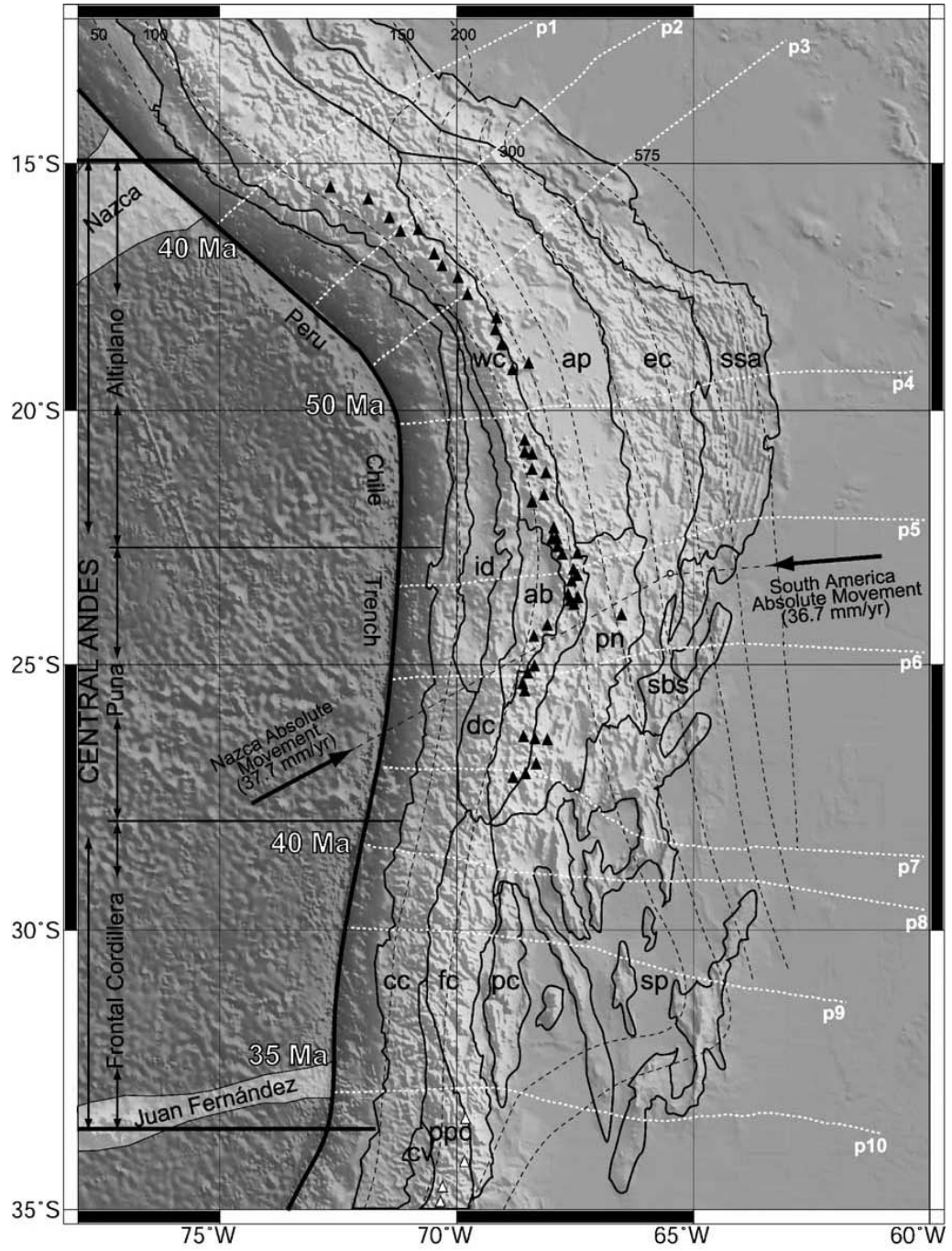


2.2 Central Andes

The Central Andes (15°-34°S) are considered here to be a continental-scale segment of the Andean convergence system. The limits of this segment coincide with the boundaries of several morphotectonic units of the continental plate [*Mpodozis and Ramos, 1989*] (Figure 2.2). These limits are also correlated with abrupt N-S changes from “flat” (< 10° dip) to “normal” (~ 30° dip) subduction in the depth range 100 to 150 km, and with the intersection of the Nazca and Juan Fernández oceanic ridges with continental margin. Based on along-strike variation of topography, volcanism, tectonic style and subduction conditions, the Central Andes can be divided into three second order segments, which are named Altiplano (15°-23°S), Puna (23°-28°S) and Frontal Cordillera (28°-34°S) [*Jordan et al., 1983; Mpodozis and Ramos, 1989; Kley et al., 1999*]. The term “main orogen” is used to refer to the sector comprising elevations higher than 3000 m (Figure 2.2).

The major present-day features of the central Andes were formed during the Cenozoic, and particularly during the last 30 Ma [e.g., *Farías et al., 2005; Allmendinger et al., 1997; Isacks, 1988; Lamb et al., 1997; Rutland, 1971; Sempere et al., 1990*]. Since then and after major plate reorganization, the Nazca and South American plates increased their velocity of relative convergence, which became almost orthogonal to the Chilean margin [*Farías et al., 2005; Pardo-Casas and Molnar, 1987; Somoza, 1998*].

Figure 2.2 (on the next page): Geotectonic framework of the Central Andean convergence system between 12° and 35°S is taken from *Tassara [2005]*. Morphotectonic units of the continental plate are depicted (partially modified from *Mpodozis and Ramos [1989]*): cc, Coastal Cordillera; id, Intermediate Depression; cv, Central Valley; dc, Domeyko Cordillera (Chilean Precordillera); wc, Western Cordillera; fc, Frontal Cordillera; ppc, Principal Cordillera; ab, Atacama Basin; ap, Altiplano; pn, Puna; pc, Precordillera; ec, Eastern Cordillera; sp, Sierras Pampeanas; ssa, Sierras Subandinas; sbs, Santa Bárbara System. Triangles are active volcanoes of the Central (black) and Southern (white) Volcanic Zones. Dashed black lines are 50 km contour lines of the subducted oceanic plate [*Cahill and Isacks, 1992*]. Nazca and South American absolute motion vectors with respect to a point in the Eastern Cordillera are from *Marret and Strecker [2000]*. The position of the Nazca and Juan Fernández oceanic ridges, as well as ages of the Nazca plate at the trench (from *Müller et al. [1997]*), are also shown. The Central Andes are subdivided into Altiplano, Puna and Frontal Cordillera segments (partially modified from *Jordan et al. [1983; Mpodozis and Ramos [1989]; Kley et al. [1999]*). Profiles used in the flexural analysis [*Tassara, 2005*] are shown by the dashed white lines labeled p1 to p10.



2.3 The Altiplano segment

2.3.1 Forearc

The Peru-Chile trench has a maximum depth of 8000 m. It is almost free of sediments and no accretionary prism is observed along the margin [e.g., *von Huene et al.*, 1999]. East of the trench, the oceanic Nazca plate subducts with a constant dip of 30° [*Cahill and Isacks*, 1992; *Creager et al.*, 1995] and the continental slope ascends steeply to the coast. The distance between the trench axis and the coast has a maximum of 170 km at the Arica bend ($\sim 18^\circ 30'S$). This geometry is correlated with the curvature of the margin, concave-seaward (Bolivian Orocline of *Isacks* [1988]).

Eastward of the coast line and along the entire margin, uplifted metamorphic (Paleozoic) and basic magmatic (Mesozoic) rocks of the Coastal Cordillera are exposed [*Reutter et al.*, 1994]. Behind this unit, the Longitudinal Valley basin is filled with Cenozoic volcanosedimentary deposits [*Hartley et al.*, 2000] (Figure 2.3).

The Domeyko Cordillera (or Chilean Precordillera) at the eastern side of the Intermediate Depression, is an Eocene magmatic and tectonic belt exhuming late Paleozoic felsic igneous rocks [*Mpodozis and Ramos*, 1989], which north of $25^\circ S$ is related to a west-verging, high-angle structural system that propagated slowly to the west during the Neogene [*Muñoz and Charrier*, 1996; *Victor et al.*, 2004; *García et al.*, 2002; *Jacay et al.*, 2002; *Fariás et al.*, 2005]. This structural system (The West-vergent Thrust System) has been described as the western tectonic limit of the Altiplano-Puna Plateau [*Muñoz and Charrier*, 1996].

The geological evolution of the forearc has been governed by eastward migration of the volcanic front from the Jurassic position in the Coastal Cordillera to its present position in the Western Cordillera. This migration has been interpreted to indicate tectonic erosion and subduction of more than 200 km of continental crust in a W-E section [*Rutland*, 1971; *Scheuber et al.*, 1994]. The migration was accompanied by an equally migrating zone of underplated mafic crust at or near the crust-mantle boundary, and intrusion into, the overlying crust [*Haschke et al.*, 2002].

2.3.2 Arc, backarc and foreland

The Central Volcanic Zone (CVZ) of the Andes ($15^\circ - 28^\circ S$) is a chain of Quaternary stratovolcanic complexes and andesitic-rhyodacitic domes of high-K calcalkaline affinities [*Allmendinger et al.*, 1997; *Kay et al.*, 1999] located on top of the Western Cordillera (max. elevations > 6000 m). This unit also

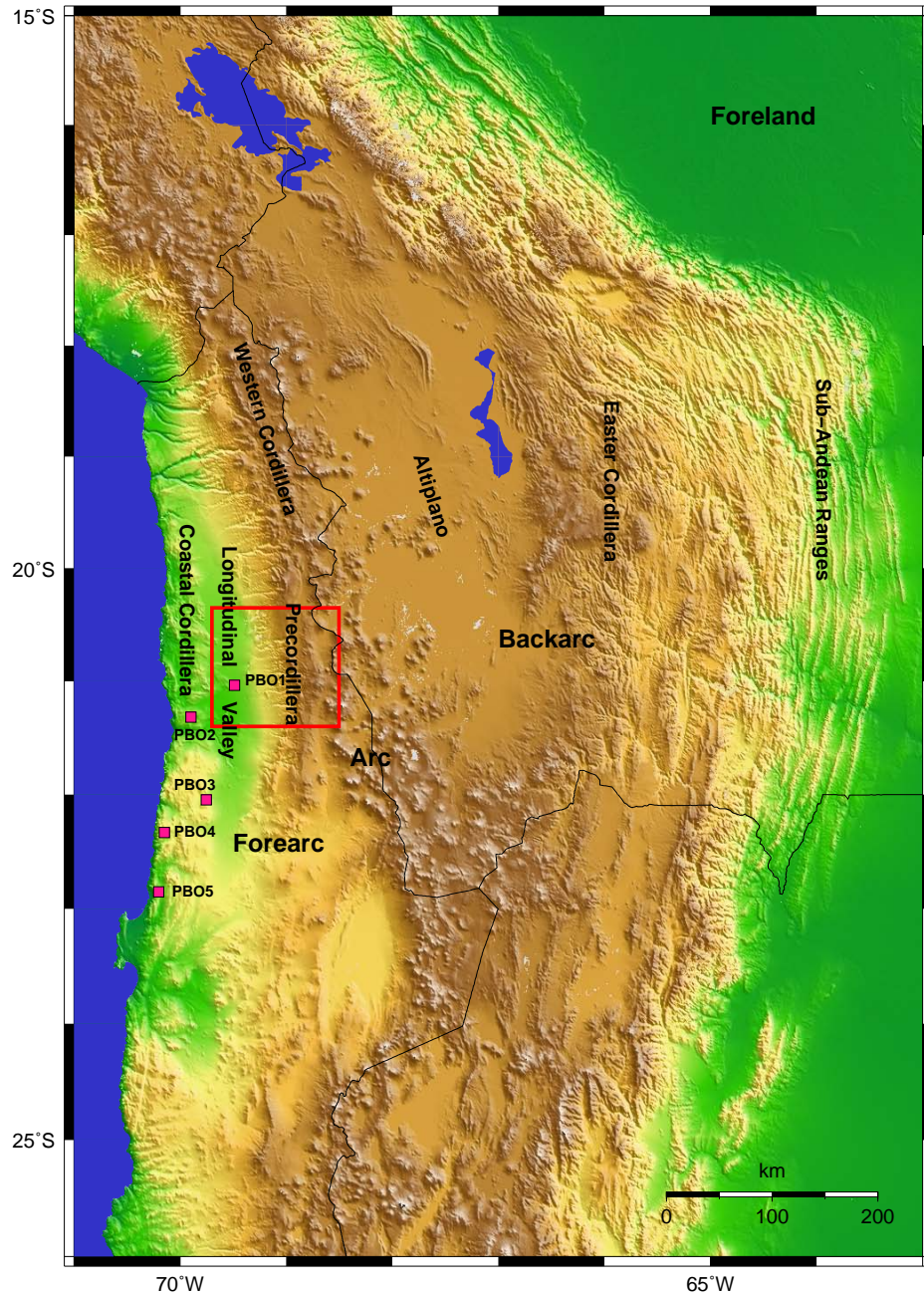


Figure 2.3: The different geomorphological units that form the Altiplano segment. Forearc: Coastal Cordillera, Longitudinal Valley, Precordillera; Arc: Western Cordillera; Backarc: Altiplano, Eastern Cordillera, Sub-Andean Ranges (Sierras Subandinas); Foreland. The red square indicates the study area. The magenta squares indicate the broad-band IPOC stations used in this study. Shaded topography from the GTOPO30 global DEM.

contains exposures of well-preserved volcanic features of middle Miocene to Pliocene ages [Wörmer *et al.*, 2000] (Figure 2.3).

Along the Altiplano and Puna further east, there are restricted outcrops of shoshonitic basalts and several large silicic complexes [de Silva, 1989]. The Altiplano is an internally drained basin filled with gently deformed Cenozoic synorogenic sediments and volcanics [Allmendinger *et al.*, 1997; Baby *et al.*, 1997; McQuarrie, 2002], located at a constant elevation of 3800 m (Figure 2.3).

The eastern boundary of the Altiplano-Puna Plateau is the Eastern Cordillera (max. elevations > 5000 m), a doubly-vergent deformation belt active until the middle-late Miocene [Heraul *et al.*, 1996; McQuarrie, 2002]. The active deformation of the Altiplano segment has been absorbed since late Miocene at the eastward-propagating thin-skinned belt of the Sub-Andean Ranges (Sierras Subandinas). The tectonic style of the active foreland deformation changes transitionally south of 23°S from the doubly-vergent thick-skinned Santa Barbara System toward the uplifted basement blocks of the Sierras Pampeanas south of 27°S . These elongated, narrow and 4000 m high ranges of crystalline Paleozoic rocks extend up to 700 km to the east of the trench axis. They were uplifted synchronously with the thin-skinned deformation of the (Argentinean) Precordillera [Ramos *et al.*, 2002].

2.3.3 Deformation and uplift of the Altiplano Plateau

The uplift of the Altiplano plateau started probably in the Miocene (23 Ma), although the exact timing is difficult to establish. The data indicate that the Western Cordillera was not more than half of its present elevation at 25 Ma, whereas the Altiplano and Eastern Cordillera may have reached 25 – 30% of their present altitude at 20 Ma and 14 Ma, respectively [Gregory-Wodzicki, 2000].

Uplift accelerated at 10 Ma during the Quechua tectonic phase, whereby the Altiplano and Eastern Cordillera rose to about 2000 – 3500 m since then. Deformation in the Eastern Cordillera is thought to have ended at ~ 9 Ma based on an undeformed erosional surface [Gubbels *et al.*, 1993]. Deformation propagated then further east into the Subandean thrust-belts, where since then all upper-crustal deformation has been accomplished.

The present-day crustal thickness (60-80 km) and surface elevation of the Altiplano is mainly considered to be a consequence of large crustal shortening [Oncken *et al.*, 2006; Farías *et al.*, 2005; Allmendinger *et al.*, 1997; Beck and Zandt, 2002; Haschke and Günter, 2003; Husson and Sempere, 2003; Isacks, 1988; Lamb and Hoke, 1997; Lamb *et al.*, 1997; McQuarrie, 2002; McQuarrie and DeCelles, 2001; Reutter *et al.*, 1988; Roeder, 1988; Schmitz, 1994;

Sheffels, 1990]. The maximum shortening is observed at the Arica bend at $\sim 18^{\circ}30'S$ (Figure 2.4). However, some discrepancy exist between the observed tectonic shortening and the amount of material needed to explain the entire crustal thickness [*Allmendinger et al., 1997; Husson and Sempere, 2003; Kley and Monaldi, 1998; Kley et al., 1999; Lamb et al., 1997; McQuarrie, 2002; Schmitz, 1994*].

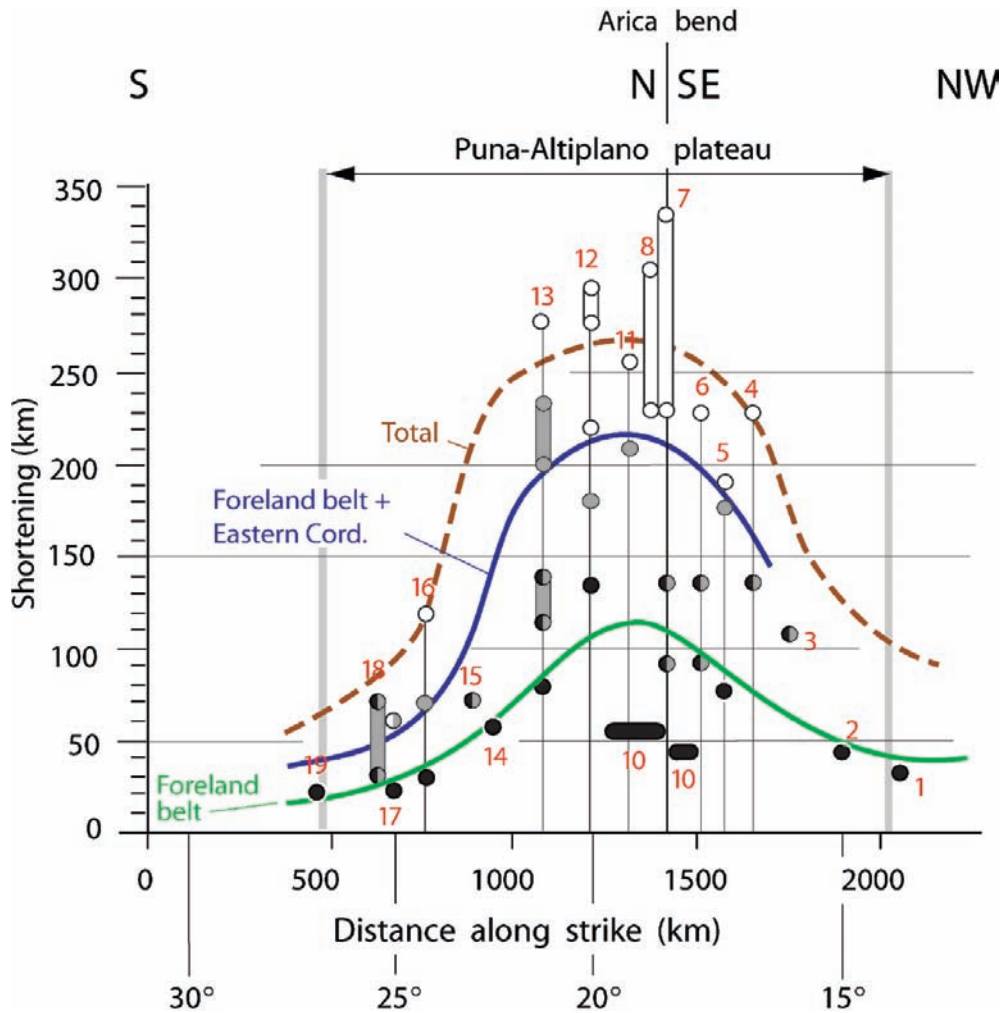


Figure 2.4: Magnitudes of crustal shortening along the Central Andes according to various published estimates (taken from *Oncken et al. [2006]*). Thin vertical lines indicate transects where the total shortening estimates have been made or can be compiled. Thick curves are the *Oncken et al. [2006]* estimates for the magnitudes and variation of shortening in the foreland belt, foreland belt plus Eastern Cordillera, and entire orogen.

In addition, geophysical and petrological studies suggest that other pro-

cesses would have been involved in crustal thickening and plateau surrection, such as magmatic addition [Gill, 1981; Hoke *et al.*, 1994; Kono *et al.*, 1989; Weaver and Tarney, 1984], lithospheric thinning and removal of the sub-crustal lithosphere [Beck and Zandt, 2002; Isacks, 1988; Lamb *et al.*, 1997; Whitman *et al.*, 1996], underplating of material removed from the forearc by subduction erosion [e.g., Baby *et al.*, 1997; Schmitz, 1994], and ductile mass transfers within the lower crust [Beck and Zandt, 2002; Gerbault *et al.*, 2002; Husson and Sempere, 2003; Kley and Monaldi, 1998]. Pre-Neogene shortening or lateral flow of lower crust from areas of excess vertical thickening may be viable options for the “missing” crustal thickness in some parts of the central Andes [Schurr, 2000].

2.4 West Fissure Fault System

Two large scale margin-parallel shear zones have been formed in the course of convergence of the Nazca and South American tectonic plates in the north Chilean Andean orogen: the Atacama Fault System (AFS) and the Precordillera Fault System (PFS) (Figure 2.5). This type of faults is connected to oblique convergence in subduction zones and is classified as “trench-linked strike-slip faults” [Woodcock, 1986]. These faults are thought to accommodate the margin parallel component of convergence within the forearc or arc region of the overriding plate [Fitch, 1972; McCaffrey, 1996].

The PFS is located in the Andean Precordillera of the north of Chile and is traceable for more than 1000 km parallel to the N-S trending continental plate margin or subduction trench [Lindsay *et al.*, 1995]. The fault system has influenced the emplacement and mineralization of a number of the largest porphyry-copper-related intrusion around the world. These faults are composed of various regional segments, each having undergone a distinct series of deformation events [Lindsay *et al.*, 1995]. In northern Chile the regional branch of the PFS is known as West Fissure Fault System (WFFS), which is well exposed as a continuous structure along a 170 km zone extending from Calama northward to Quebrada Blanca.

The WFFS is a very dynamic regional fault zone, which focused hydrothermal activity at least intermittently over millions of years which is the most important reason why the Chuquicamata and others Porphyry Cooper deposits became such a huge concentration of metal and sulphur [Ossandón *et al.*, 2001].

The fault zone has been active since the Late Eocene/Early Oligocene [Reutter *et al.*, 1996]. Most authors assume that an older dextral strike-slip motion caused by subduction-related magmatic arc tectonics of the Incaic

tectonic phase was followed by sinistral shear corresponding to a time of reduced convergence rate [Reutter *et al.*, 1996]. The youngest event is the reactivation of dextral slip under the same kinematic conditions as described for the older phase. The tectonic inversion of the fault system is also reflected in varying amounts of displacement (dextral displacement: 0.5-2 km, sinistral displacement: 35-37 km; Reutter *et al.* [1991]; Tomlinson and Blanco [1997a,b]).

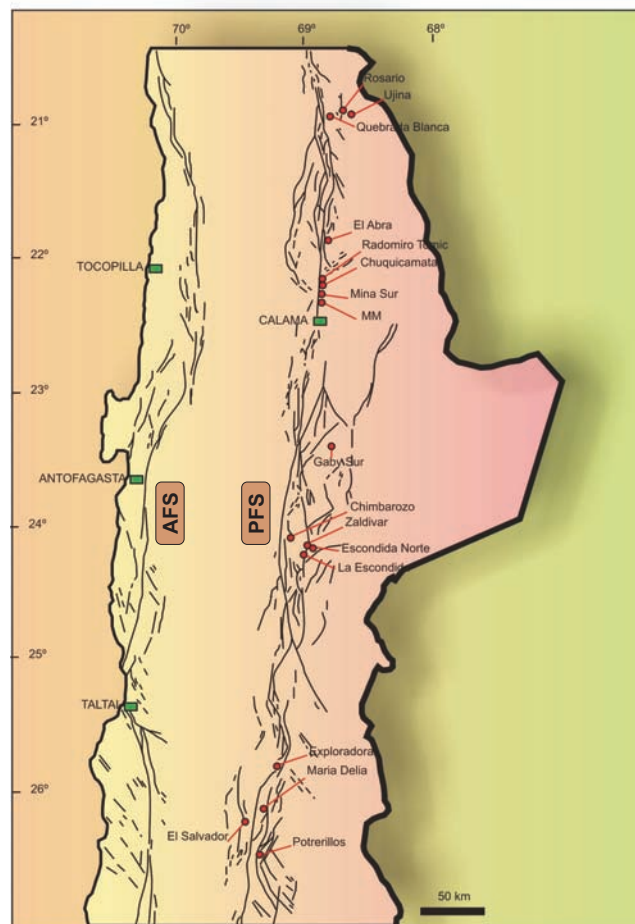


Figure 2.5: The two large scale margin-parallel shear zones (after Camus [2003]), the Atacama Fault System (AFS) and the Precordillera Fault System (PFS). The red dots indicate the location of the most important Porphyry Cooper deposits in the region, which are shown with their names. All Porphyry Cooper deposits are spatially related to PFS. The green rectangles indicate the cities in the Antofagasta region

Chapter 3

Theoretical background of the methods used

3.1 Precise location technique NonLinLoc

Seismotectonic studies concern themselves with understanding the distribution of earthquakes in space, time, size and style. Under certain circumstances, the spatial and temporal distribution of earthquakes provides information on tectonic regime and material properties of an area and on the depth of the brittle-ductile transition.

Precise earthquake hypocenter locations are thus the primary requirement to study structures that trigger seismic activity.

The seismic event locations were determined using an improved technique, namely Non Linear Localization (NonLinLoc hereinafter, *Lomax et al.* [2000, 2001]). The algorithm is based on probabilistic earthquake location; it provides a comprehensive uncertainty and resolution information.

NonLinLoc uses efficient global sampling algorithms to obtain an estimate of the posterior probability density function (PDF) in 3-D space for the hypocenter location. The algorithm follows the probabilistic formulation of inversion presented in *Tarantola and Valette* [1982]; *Tarantola* [1987], and the equivalent methodology for earthquake location [i.e., *Tarantola and Valette*, 1982; *Moser et al.*, 1992; *Wittlinger et al.*, 1993; *Lomax et al.*, 2000]. The unknown parameters for an earthquake location are the hypocentral coordinates $\mathbf{x} = (x, y, z)$ and the origin time T ; the observer data are a set of arrival times, \mathbf{t} , and a theoretical relation gives predicted traveltimes, \mathbf{h} . *Tarantola and Valette* [1982] showed that if the theoretical relationship and the observed arrival times are assumed to have Gaussian uncertainties with covariance matrices \mathbf{C}_T and \mathbf{C}_t , respectively, and if the prior information on

the origin time parameter T is taken as uniform, then it is possible to integrate the PDF over T to obtain the marginal PDF for the spatial location parameters, $\sigma(\mathbf{x})$. This marginal PDF reduces to [Tarantola and Valette, 1982; Moser et al., 1992]

$$\begin{aligned}\sigma(\mathbf{x}) &= K\rho(\mathbf{x}) \exp\left[-\frac{1}{2}g(\mathbf{x})\right], \\ g(\mathbf{x}) &= [\hat{\mathbf{t}}_0 - \hat{\mathbf{h}}(\mathbf{x})]^T[(\mathbf{C}_t + \mathbf{C}_T)^{-1}][\hat{\mathbf{t}}_0 - \hat{\mathbf{h}}(\mathbf{x})].\end{aligned}\tag{3.1}$$

In this expression K is a normalization factor, $\rho(\mathbf{x})$ is a density function of prior information on the model parameters, and $g(\mathbf{x})$ is the likelihood function (the method makes available two different likelihood function: an L2 misfit function or a function based on the equal differential-time (EDT) by Font et al. [2004]. The $\hat{\mathbf{t}}_0$ is the vector of observed arrival time \mathbf{t} minus their weighted mean, and $\hat{\mathbf{h}}$ is the vector of theoretical traveltimes \mathbf{h} minus their weighted mean, where the weights w_i are given by

$$w_i = \sum_j w_{ij}; \quad w_{ij} = [(\mathbf{C}_t + \mathbf{C}_T)^{-1}]_{ij}.\tag{3.2}$$

The PDF can be computed applying three different algorithms [Lomax et al., 2000]: grid-search, Metropolis-Gibbs sampling and Oct-Tree. In this study, a grid-search method was performed. This consist of a sequence of successively finer nested grid searches within a spatial x, y, z volume. The grid search is very time-consuming but performs a systematic, exhaustive coverage of the search region and thus can identify multiple optimal solutions and highly irregular confidence volumes.

To make the location program efficient for complicated 3-D models, the traveltimes between each station and all nodes of an x, y, z spatial grid are calculated once using a 3-D version [Le Meur et al., 1997] of the Eikonal finite difference scheme of Podvin and Lecomte [1991] and then stored on disk as traveltime grid files. The forward calculation during location reduces to retrieving the traveltimes from the grid files and forming the likelihood (misfit) function $g(\mathbf{x})$ in eq.(3.1). After the traveltimes are calculated throughout the grid, the gradients of traveltime at each node are examined to generate a grid of take-off angles for the ray from a source at each grid node to the station. These take-off angles are used for fault plane solution estimations.

A grid of PDF values obtained by the grid search, samples drawn from this grid, or samples of the PDF obtained by the Metropolis-Gibbs sampler represent the complete probabilistic spatial solution of the earthquake location problem. This solution indicates the uncertainty in the spatial location

due to Gaussian picking and traveltime calculation errors, the network-event geometry and the incompatibility of the picks. The locations uncertainly will in general be non-ellipsoidal (non-Gaussian) because the forward calculation involves a non-linear relationship between hypocenter location and traveltimes.

3.2 Local magnitude determination

The local magnitude scale is calculated by determining an amplitude attenuation scale using amplitudes and distances in the SEISAN calibration file [Havskov and Ottemöller, 2000]. The formula used to calculate local magnitude is:

$$M_L = a \cdot \log(amp) + b \cdot \log(dist) + c \cdot dist + d \quad (3.3)$$

where a, b, c, d are constants, \log is logarithm to the base 10, amp is maximum ground amplitude (zero-peak) in nm and $dist$ is hypocentral distance in km. The constants are for California [Hutton and Boore, 1987] which gives the following relation

$$M_L = \log(amp) + 1.1 \cdot \log(dist) + 0.00189 \cdot dist - 2.09 \quad (3.4)$$

3.3 Focal mechanisms

3.3.1 Introduction

Several methods for determining focal mechanisms (FM) are in use such as first motion of P -waves [Snoke, 2003], polarizations and amplitudes of S -waves [e.g., Khattri, 1973], the analysis of P/S amplitudes ratios [e.g., Kisslinger et al., 1981; Snoke, 2003] and moment tensor inversion [e.g., Stein and Wysession, 2003]. All these methods are using the radiation pattern of the seismic rays that expresses the orientation of the active fault and the slip direction (Figure 3.1). These patterns can be used to describe the kinematic processes in the seismic source.

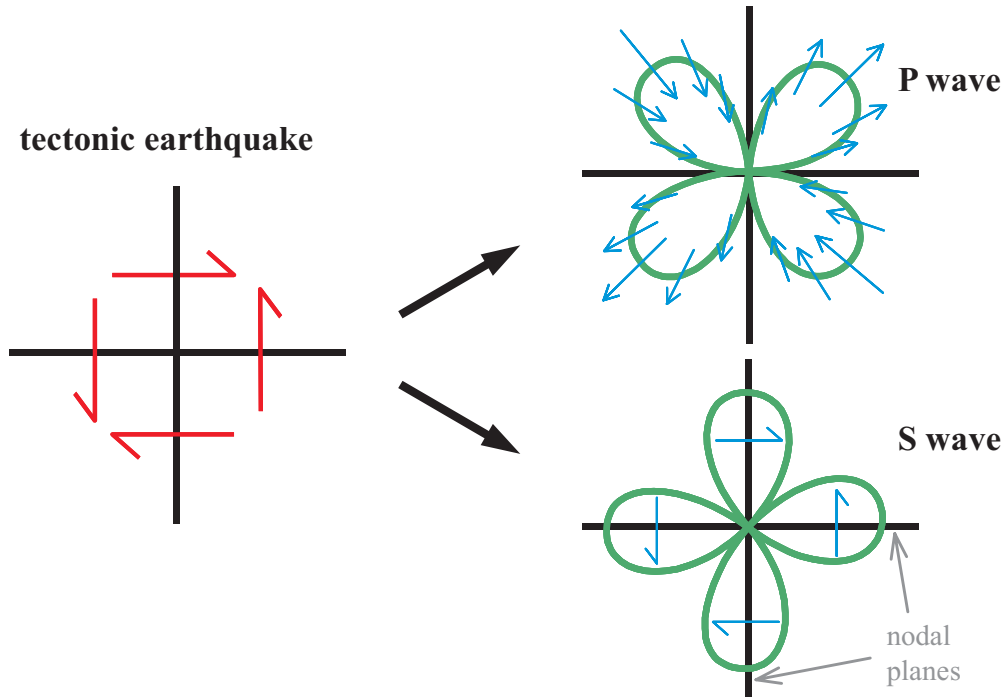


Figure 3.1: P and S wave radiation pattern of a double couple source, after [Barth *et al.*, 2008]

3.3.2 First-motion of P -waves

P -waves radiate relative to the focus with compressional or dilatational initial motion (Figure 3.1). The signal changes in direction of the fault plane and the orthogonal auxiliary plane (both are called nodal planes). Along these planes there is no radiation of P -waves. The first onset of the P -wave on a seismogram of the vertical seismometer component is used to distinguish between a compressional and dilatational first motion of the wavefront. The observed first motion is then projected backwards along the ray path onto a conceptual homogeneous unit sphere around the focus (focal sphere), which is thought to be a point source at the very beginning of the rupture event. Any P -wave ray leaving the source can be identified by two parameters: the azimuth from the source, ϕ , and the angle of emergence, i_0 (Figure 3.2). The angle of emergence is a function of the distance, Δ , between the source and the recording station, and for near stations the crustal model in use. The geographic position of the seismometer is transferred on the focal sphere to a point where the tangent to the ray at the source intersects the focal sphere.

When all available data are plotted in the lower hemisphere of the stere-

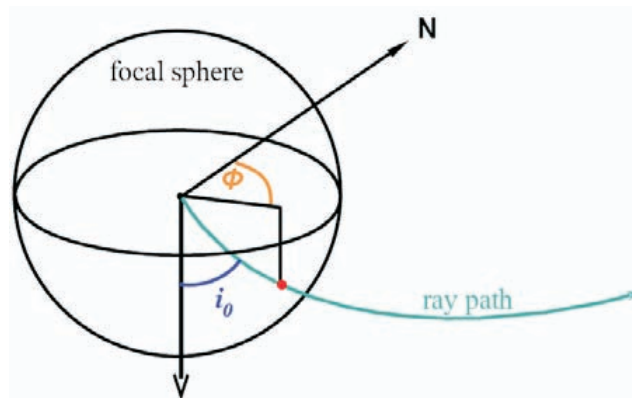


Figure 3.2: Focal sphere of an earthquake source. Shown is a ray path with azimuth ϕ and angle of emergence i_0 , after [Barth *et al.*, 2008].

ographic projection, two orthogonal nodal planes separating compressional from dilatational first motion can be drawn. The axes of the maximum shortening and maximum bisecting the quadrant are known as the P and T axes, respectively. Thus, the axes are principal strain axes that not necessarily coincide with the principal stress axes.

The P axis lies within the quadrant of dilatational motions, whereas the T axis lies within the quadrant of compressional initial motions (Figure 3.3). Both are perpendicular to the intersection of the two nodal planes. The axis formed by this intersection is called the B - or the null axis. The FM is fully described by the orientation (dip direction and dip) of the P -, T -, and B -axes.

3.3.3 Amplitude ratios

The use of body-wave amplitude data in the determination of focal mechanisms of small earthquakes recorded at regional distances has been used – more typically – when the station density is low, the velocity structure known only approximately, and the polarities of the first arrivals are often ambiguous.

It is almost always possible to find several different focal mechanisms consistent with the data. Generally, the poorer the data, the larger the number of possible solutions. The range of possible solutions can often be further constrained if one can read, to within 10%, the P and S amplitudes on vertical-component seismograms.

Although the SV is read on the radial component, Kisslinger *et al.* [1982] describes procedures for using SV/P vertical-component amplitude ratios

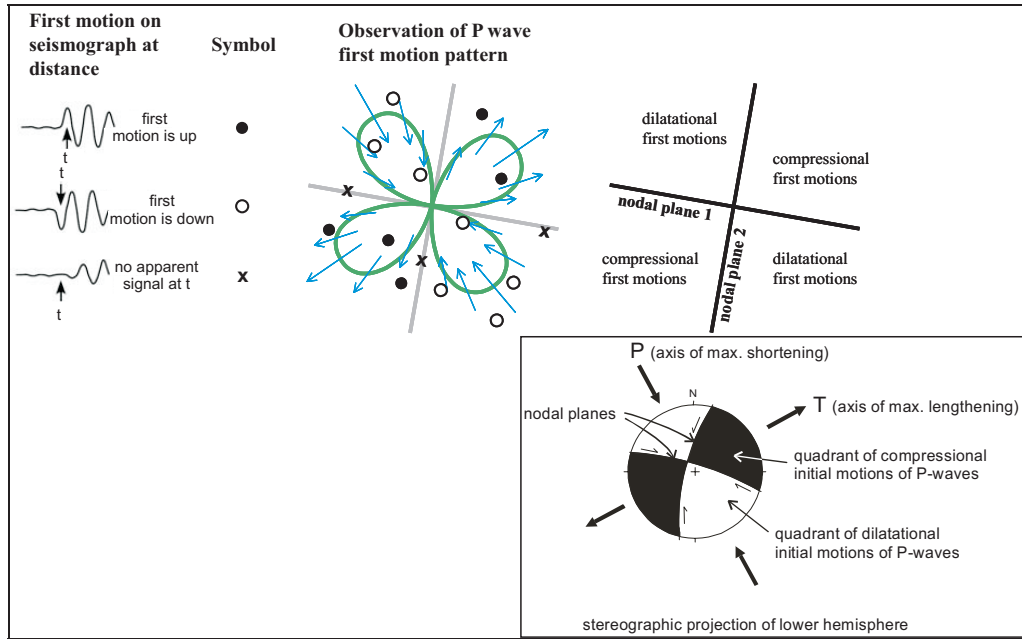


Figure 3.3: Element of a fault plane solution (see the text for more explanation, after [Barth *et al.*, 2008]).

recorded by local and regional networks to constrain focal mechanisms. This technique is also used in the SEISAN package and therefore requires a brief description here.

The ratio of the vertical component of SV to the vertical component of P , denoted $(SV/P)_z$, is the observed quantity to be analyzed. Distances are restricted so that the first arrivals are the P - and S -waves that have traveled upward from the source as direct waves. For the focal depth and velocity structures involved in the cases analyzed the distances must not be more than ~ 100 km, and generally less than ~ 60 km.

The procedure seeks a focal mechanisms (strike, dip and slip direction) such that the calculated values of $(SV/P)_z$ are in sufficiently close agreement with those observed at the set of stations. The heart of the computational scheme is the following expression relating the ratio of SV to P amplitudes at a point in a infinite, homogeneous, elastic medium to the three fault parameters and the direction to the point [Kisslinger *et al.*, 1982]:

$$(SV/P)_0 = (V_P/V_S)^3 \cot i_h \times \{1 - [(\cot \delta - \tan \delta) \sin \lambda \tan i_h \sin A + 2 \sin \lambda + \csc \delta \cos \lambda \tan i_h \cos A]/2D\} \quad (3.5)$$

where

$$\begin{aligned}
D = & \cos \lambda \cos A \sin i_h \times [-\sin i_h \sin A \sec \delta + \cos i_h \csc \delta] \\
& + \sin \lambda \sin i_h \cos i_h \sin A (\cot \delta - \tan \delta) \\
& + \sin \lambda (\cos^2 i_h - \sin^2 i_h \sin^2 A)
\end{aligned} \tag{3.6}$$

and δ is the dip of the fault, λ is the direction of slip, measured in the fault plane from the strike, A is the azimuth to the station, measured from the strike of the fault ($= A_S - A_f$, where A_S is the earthquake-station azimuth and A_f is the fault strike), i_h is the take-off angle of the ray to the station at the source, and V_P and V_S are the P - and S -wave velocities, respectively.

The ratio $(SV/P)_0$ for waves leaving the source must be converted into $(SV/P)_z$ at the surface of the Earth, where the observations are made. The wave amplitudes must be propagated through the velocity structure and corrected to the vertical components at the surface. One of the great advantage of using the ratio of amplitudes rather than the absolute amplitudes of the waves taken separately is that the effects of transmission across internal boundaries tend to cancel.

On the other hand, if one has data from three-component seismographs, the SH to P amplitude ratio provides almost independent data [Snoke, 2003]. For some events, one may observe clear SH and/or SV polarities at one or more stations, and the SV/SH amplitude ratio may be better constrained than a ratio including P [Snoke, 2003].

3.4 Stress tensor analysis

The focal mechanisms are used as a tool to determine the direction and shape of the stress tensor [Rivera and Cisternas, 1990]. A stress tensor, for example induced from the movement of tectonic plates, acting in a homogeneous, elastic and isotropic medium without friction and without pre-existing faults will have a maximum shear stress of $(\sigma_1 + \sigma_3)/2$, where σ_1 and σ_3 with $\sigma_1 > \sigma_3$ are the biggest and smallest eigenvalues of the stress tensor (positive stress for compression). Hence, faults will be generated with an orientation of 45° from the extreme eigen stress directions. Let us now call P and T as the axes corresponding to the eigen directions of the seismic moment tensor \mathbf{M}_{ij} of the earthquake, respectively, associated with the eigenvalues $+M_0$ and $-M_0$ (the scalar seismic moment). By definition, the P and T axes are always at 45° from the nodal planes. In such simple case, the directions P and T will be the same as the σ_1 and σ_3 axes, respectively.

Nevertheless, the medium is often pre-fractured and friction exists on faults. Hence, the eigen directions P and T of the seismic moment tensor

are usually different from the eigen directions σ_1 and σ_3 of the stress tensor. It means that a unique stress tensor can allow faults of many different orientations to act simultaneously.

Since only kinematic data are used (polarities of P -waves and corresponding azimuth and incidence), the absolute amplitude of the stress tensor cannot be determined. We assume that all earthquakes of different magnitudes will be equally representative of the stress tensor. Hence, we discard the earthquake magnitudes in the stress tensor analysis. This means focal mechanisms may change within the range allowed by the unique stress tensor.

The shape factor is defined by *Rivera and Cisternas [1990]* as: $R = (\sigma_z - \sigma_x)/(\sigma_y - \sigma_x)$, where σ_x , σ_y , and σ_z are the principal stresses (with $\sigma_y > \sigma_x$). The σ_z is close to the vertical in order to interpret the shape factor R in a tectonic sense. R varies from $-\infty$ to $+\infty$.

The relationship of the non-ordered eigen values σ_x , σ_y , and σ_z with respect to the ordered eigen values $\sigma_1 > \sigma_2 > \sigma_3$ depends on R as follows:

1. $R < 0$, triaxial compression, with $\sigma_y > \sigma_x > \sigma_z$ then $\sigma_y = \sigma_1$, $\sigma_x = \sigma_2$ and $\sigma_z = \sigma_3$.
2. $0 < R < 1$, shear, with $\sigma_y > \sigma_z > \sigma_x$ then $\sigma_y = \sigma_1$, $\sigma_z = \sigma_2$ and $\sigma_x = \sigma_3$.
3. $1 < R$, triaxial extension, with $\sigma_z > \sigma_y > \sigma_x$ then $\sigma_z = \sigma_1$, $\sigma_y = \sigma_2$ and $\sigma_x = \sigma_3$.

Focal mechanisms depend on the orientations of the pre-existing faults. In case 1, we can expect reverse and strike-slip faults. In case 2, we have to consider different cases. If a vertical fault pre-exists, strike-slip mechanisms are expected. If one pre-existing fault dips in the y -axis, reverse mechanisms are expected. If the pre-existing fault dips in the x -axis, normal fault mechanisms are expected. Hence, in this case, strike-slip, reverse and normal fault mechanisms may be expected simultaneously. In case 3, only normal and strike-slip fault mechanisms are expected. The particular case of $R = 0$ corresponds to the uniaxial compression, $R = 1$ to the uniaxial extension, $R \rightarrow -\infty$ to a radial compression, and $R \rightarrow +\infty$ to a radial extension.

3.5 Moment tensor analysis

Waveforms are related to the source and medium properties by means of the Moment Tensor (MT) and the Green's tensor. Assuming knowledge of the Earth's elastic structure, as well as position of the source and station,

synthetic Green's functions can be calculated. When considering regional stations dominated by interference of crustal phases, full (=complete) elastodynamic Green's functions must be used. The same is true if the near-field effects are to be analyzed at local stations. In horizontally layered one-dimensional 1D crustal models, the full Green's functions can be calculated basically by any frequency wavenumber or reflectivity method. Then, the MT retrieval is a linear inverse problem, formally overdetermined and solved by the least-squares method. If the source position and time are also to be determined, the least-squares method is complemented by a spatiotemporal grid search.

The full moment tensor has a deviatoric and volumetric part. Retrieval of the volumetric part is very problematic, although not impossible [e.g., *Frohlich, 1994; Campus and Faeh, 1997; Dregger and Woods, 2002*]. Fortunately, the inverse problem remains linear if limited to the deviatoric moment tensor. The deviatoric tensor can be decomposed into the double-couple (DC) and non-double-couple (non-DC) component. The decomposition is non-unique [e.g., *Jost and Hermann, 1989*]; a very common decomposition is that into the DC and CLVD part, also followed in this study. Here, CLVD stands for the compensated linear vector dipole. The DC and non-DC (=CLVD) parts have relative size $(1 - 2f)$ and $(2f)$, respectively, where 1 , $f - 1$, and $-f$ are the normalized MT eigenvalues. The term $100(1 - 2f)$ is referred to as the double-couple percentage, DC%. Usefulness of the non-DC component as a physical parameter of tectonic earthquakes is highly limited due to many masking effects, such as incomplete structural information, sparseness of networks, curvature of faults, source complexity, and anisotropy [*Sileny et al., 1996; Julian et al., 1998; Yunga et al., 2005; Roessler et al., 2007; Vavrycuk, 2007*]. When the size of the deviatoric moment tensor and orientation of its eigenvectors are relatively stable, they can be characterized by the scalar moment, strike, dip, and rake.

The computer code ISOLA is used combining the computational speed of Fortran and the users' comfort of Matlab [*Sokos and Zahradník, 2008*]. It makes use of the inverse-problem formulation of *Kikuchi and Kanamori [1991]*, based on six elementary MTs. Their equation (6) is used to quickly evaluate the correlation between observed and synthetic waveforms. The Green's functions are calculated by the discrete-wavenumber method [*Bouchon, 2003*]. The match between the observed and best-fitting synthetic data is characterized by the overall variance reduction: $varred = 1 - E/O$, where $E = \sum(O_i - S_i)^2$, $O = \sum(O_i)^2$, with O and S standing for the observed and synthetic data, along with summation over all samples, components, and stations. The code also allows complex rupture histories described by multiple point-source subevents, each one represented by a delta function [*Zahradník*

et al., 2005].

The least-squares equations are characterized by eigenvectors and eigenvalues of the corresponding matrix (avoid confusion with the MT eigenvalues). Small eigenvalues indicate that the matrix is close to singularity, hence the MT inversion becomes ill conditioned. What is small and what is large depends on the problem under study.

3.6 Spectral analysis

The spectral analysis used in SEISAN [Havskov and Ottemöller, 2000] is based on the Brune [1970] model and various assumptions about the geometrical spreading and anelastic attenuation.

The theoretical displacement spectrum $d(f)$ [Brune, 1970] is:

$$d(f) = \frac{G(r, h) \cdot D(f) \cdot M_0 \cdot KK}{(1 + f^2/f_0^2) \cdot (4 \cdot \pi \cdot \rho \cdot V^3)} \quad (3.7)$$

where $G(r, h)$ is geometrical spreading, r is epicentral distance, h is hypocentral depth, $D(f)$ the diminution function due to anelastic attenuation, M_0 is the seismic moment, f is the frequency, ρ the density, V the velocity at the source, f_0 the corner frequency and KK a factor of $2.0 \cdot 0.6$ to correct for free surface effect and radiation pattern.

The diminution function $D(f)$ is written as

$$D(f) = P(f) \cdot \exp\left(\frac{-\pi \cdot f \cdot trtime}{(q_0 \cdot f^{q_\alpha})}\right) \quad (3.8)$$

where $trtime$ is the travel time from the origin time to the start of the spectral window and

$$P(f) = \exp(-\pi \cdot \kappa \cdot f) \quad (3.9)$$

is meant to account for near surface losses [Singh *et al.*, 1982] with the constant κ having a value of the order 0.02 s. Anelastic attenuation Q is assumed to be frequency dependent following the relation

$$Q = q_0 \cdot f^{q_\alpha} \quad (3.10)$$

The geometrical spreading has been defined to be dependent on the wave type with several possibilities, all made equivalent to a distance called geo-distance (GD) such that geometrical spreading is expressed as $1/GD$. There are several possibilities for GD :

P-waves:

GD is the hypocentral distance

$$HD = \sqrt{(r \cdot r + h \cdot h)} \quad (3.11)$$

so body wave spreading is assumed.

S-waves:

The geometrical spreading has been made dependent on distance and depth. At short distances, the geometrical spreading is assumed to be body wave spreading. For distances beyond the Herrmann-Kijko distance (default of 100 km) and a shallow focus, the following relation is used:

$$G(r, h) = \begin{cases} \frac{1}{r} = \frac{1}{GD} & \text{for } r < 100 \text{ km} \\ \frac{1}{\sqrt{100-r}} = \frac{1}{GD} & \text{for } r > 100 \text{ km} \end{cases} \quad (3.12)$$

which is commonly used [*Herrmann*, 1985; *Herrmann and Kijko*, 1983]. This relation assumes surface wave dispersion for epicentral distances larger than 100 km. In SEISAN 100 km is the default.

The above relation breaks down if the depth is large or comparable to the epicentral distance and in that case body wave spreading is again assumed. In order to get a smooth transition from surface wave to body wave spreading, it is assumed that the relation changes nearly linearly from surface wave spreading to body wave spreading between the depth GEO-DEPTH1 to GEO-DEPTH2. For depth less than GEO-DEPTH1 (default 50 km), Herrmann-Kijko spreading is assumed, for depth larger than GEO-DEPTH2 (default 100 km), body wave spreading is assumed with the transition in between.

From the spectral parameters, source radius and stress drop can be calculated as follows:

$$\text{source radius} = 0.35 \cdot \frac{V_S}{f_0} \quad (3.13)$$

where f_0 is the corner frequency and V_S the *S*-velocity at the source.

$$\text{stress drop} = \frac{0.44 \cdot M_0}{(\text{source radius})^3} \quad (3.14)$$

3.6.1 Determination of M_0 and M_W

The spectral analysis is used to determine the seismic moment M_0 , source radius and stress drop. First the attenuation and instrument corrected displacement spectrum are made, then, the flat spectral level Ω_0 , and corner frequency f_0 are determined and finally the seismic moment, source radius and stress drop can be calculated.

The general parameters are:

V: Velocity used (km/s) (V_P or V_S)

ρ : Density (g/cm^3)

Dist: Hypocentral distance (km)

q_0 : q_0 for spectral amplitude correction

q_α : q_α for spectral amplitude correction

κ : kappa

The spectral parameters are calculated using the relations [*Havskov and Ottemöller, 2000*],

$$M_0 = \frac{4 \cdot \pi \cdot \rho \cdot V^3 \cdot 10^\Omega}{(G(r, h) \cdot KK)} \quad (3.15)$$

where V is the seismic wave velocity at the source (P or S if P - or S -spectrum respectively) and Ω the spectral flat level on the attenuation corrected displacement spectrum.

$$M_W = 2/3 \cdot \log_{10}(M_0) - 6.06 \quad (3.16)$$

which is equivalent to the relation

$$M_W = 2/3 \cdot \log_{10}(M_0) - 10.73 \quad (3.17)$$

if the moment is in dynes-cm [*Kanamori, 1977*]. The moment is calculated in Nm, the source radius in km and the stress drop in bars.

3.7 Frequency-magnitude distribution

Physical background

Earthquake frequency-magnitude distribution relationship is a way to examine seismic activity in a area. The frequency-magnitude distribution is described by the Gutenberg-Richter law [*Gutenberg and Richter, 1956*],

$$\log_{10} N = a - bM \quad (3.18)$$

where N is the number of earthquakes with magnitudes greater than or equal to M . The b -value describes the ratio of occurrence of small to large earthquakes. Globally, the b -value is ~ 1 [e.g., *Stein and Wysession, 2003*], meaning a 10-fold decrease in seismic activity associated with an increase in each subsequent unit magnitude M . The b -value varies significantly between individual fault zones [e.g., *Schorlemmer et al., 2005; Wesnousky, 1994; Schorlemmer and Wiemer, 2005*], and even within a particular space and time range [*Nuanmin et al., 2005*]. The b -value can vary with the material heterogeneity [*Mogi, 1962*]. *Warren and Latham [1970]* found a relationship of the b -value with the thermal state of the rock. *Scholz [1968]* is the first to recognize that the b -value has a clear relationship with the stress in a volume rock. Thus, the b -value decreases with the increased stress in the rock.

3.8 Interevent-time distribution

The interevent-time is defined as the time between consecutive events, once a window in space, time and magnitude has been selected. In this way, the i -th recurrence time is defined as

$$\Delta t_i \equiv t_i - t_{i-1}, \quad i = 1, 2, \dots \quad (3.19)$$

where t_i and t_{i-1} denote, respectively, the time of occurrence of the i -th and $i - 1$ -th earthquake in the selected space-time-magnitude window. Note that following *Bak et al. [2002]*, once the window has been selected, no further elimination of events is performed and then, all events are equally considered, independently of their hypothetical consideration as mainshocks, aftershocks or foreshocks.

The interevent-time is a variable quantity and it is convenient to work with its probability density [*Corral, 2006*]. The probability density, in the case of interevent-times, is defined as the number of recurrence times within a small interval of values, normalized to the total number of recurrences and divided by the length of the small interval (to remove the dependence on it);

$$p(\Delta t) \equiv \frac{\text{Prob}[\Delta t \leq \text{interevent-time} < \Delta t + d\Delta t]}{d\Delta t}, \quad (3.20)$$

where Prob denotes probability, Δt refers to a precise value of the interevent-time, and $d\Delta t$ is the length of the interval. Strictly, $d\Delta t$ should tend to zero, but in practice is a compromise necessary to reach statistical significance

for each interval, as the number of data is not infinite. Moreover, as there are multiple scales involved in the process (from seconds to years) it is more convenient to consider a variable $d\Delta t$, with the appropriate size for each scale.

For a spatial region of arbitrary coordinates, shape and size, independent of tectonic divisions or provinces, only events with magnitude M larger than a threshold value M_c are selected (naturally, the value M_c has to be high enough to guarantee the completeness of the data). This means that the interevent-time density, $p(\Delta t)$, depends on M_c and on the size, shape, and coordinates of the region. In order to stress this dependence a subscript w (from window) is added to the density, which turns out $p_w(\Delta t)$.

If for a given window, its mean seismic rate is defined as the number of earthquakes divided by the time period covered by the windows, i.e.

$$\lambda_w \equiv \frac{\text{number of events in } w}{\text{time extent of } w}, \quad (3.21)$$

then, stationarity imposes that the mean rate is roughly constant for different windows and a unique seismic rate λ can be defined for a long period [Corral, 2006].

When the x -axis is rescaled as $\lambda_w \Delta t$ and the y -axis as $p_w(\Delta t)/\lambda_w$, all the different densities of different windows collapse onto a single curve. This data collapse allows to write the recurrence-time probability density in the form of scaling law [Corral, 2006],

$$p_w(\Delta t) = \lambda_w f(\lambda_w \Delta t), \quad (3.22)$$

where the scaling function f is the same for all the different M_c 's. Then, the above mentioned qualitative similarity between the recurrence-time distributions becomes clearly quantitative.

The functional form of f turns out to be close to a generalized gamma distribution and considering that $\tau = \lambda_w \Delta t$, then, the formula 5.16 can be written as:

$$p(\tau) = C \cdot \tau^{\gamma-1} e^{-\tau/\beta} \quad (3.23)$$

In this case the constant C in the eq. 5.17 is given by $C = (\beta^\gamma \Gamma(\gamma))^{-1}$, where $\Gamma(x)$ is the gamma function. The parameter β is determined simply by calculating the mean $\bar{\tau}$ and the variance σ_τ^2 of the interevent times, namely, $\beta = \sigma_\tau^2 / \bar{\tau}$ and $\gamma = \bar{\tau} / \beta$. Due to the normalization of the interevent times, the mean is $\bar{\tau} = 1$ and we have $\beta = \sigma_\tau^2$ and $\gamma = 1/\beta$.

This distribution was claimed to be universal for stationary seismicity [Corral, 2006]; that is, it should hold from worldwide to local scales and

for all magnitudes ranges. However, the condition of stationarity implies a selection of regions where aftershock activity is not dominant [Hainzl *et al.*, 2006].

Based on some general assumptions, Molchan [2005] could theoretically show that, in agreement with the equation (5.17), the distribution decays exponentially for large interevent-times and that the value $1/\beta$ is the fraction of mainshocks among all seismic events. His only assumption is that the seismicity consists of a Poissonian background activity and triggered aftershocks that are supposed to follow the Omori law. Thus, equation 5.17 can only be universal if the fraction of mainshocks within the activity is constant and close to 60% (for $\beta = 1.58$). However, the existing estimations of the mainshocks vary between 10% and over 90% for different regions and seem to be inconsistent with a single universal number [e.g., Reasenber, 1985; Kagan, 1991]. If the fraction of mainshocks is not universal, then the constant $1/\beta$ in equation 5.17 should vary for different regions. In this case, analyzing the interevent-time distribution could yield a nonparametric estimate of the mainshock rate [Hainzl *et al.*, 2006].

3.9 Principal Components Analysis

Principal Components Analysis (PCA) can be used to fit a linear regression that minimizes the perpendicular distances from the data to the fitted model. This is the linear case of what is known as Orthogonal Regression or Total Least Squares.

PCA is based on the statistical representation of a random variable. Following to Gonzalez and Woods [1992] suppose we have a random vector population \mathbf{x} , where

$$\mathbf{x} = (x_i, \dots, x_n)^T \quad (3.24)$$

and the mean of that population is denoted by

$$\mu_{\mathbf{x}} = E\{\mathbf{x}\} \quad (3.25)$$

and the covariance matrix of the same data set is

$$\mathbf{C}_x = E\{(\mathbf{x} - \mu_{\mathbf{x}})(\mathbf{x} - \mu_{\mathbf{x}})^T\} \quad (3.26)$$

The components of \mathbf{C}_x , denoted by c_{ij} , represent the covariances between the random variable components x_i and x_j . The component c_{ii} is the variance of the component x_i . The variance of a component indicates the spread of the component values around its mean value. If two components x_i and x_j

of the data are uncorrelated, their covariance is zero ($c_{i,j} = c_{j,i} = 0$). The covariance matrix is, by definition, always symmetric.

From a sample of vectors x_1, \dots, x_M , we can calculate the sample mean and the sample covariance matrix as the estimates of the mean and the covariance matrix.

From a symmetric matrix such as the covariance matrix, we can calculate an orthogonal basis by finding its eigenvalues and eigenvectors. The eigenvectors \mathbf{e}_i and the corresponding eigenvalues λ_i are the solutions of the equation

$$\mathbf{C}_x \mathbf{e}_i = \lambda_i \mathbf{e}_i, \quad i = 1, \dots, n \quad (3.27)$$

For simplicity we assume that the λ_i are distinct. These values can be found, for example, by finding the solutions of the characteristic equation

$$|\mathbf{C}_x - \lambda \mathbf{I}| = 0 \quad (3.28)$$

where the \mathbf{I} is the identity matrix having the same order as \mathbf{C}_x and the $|\cdot|$ denotes the determinant of the matrix. If the data vector has n components, the characteristic equation becomes of order n . This is easy to solve only if n is small. Solving for eigenvalues and corresponding eigenvectors is a non-trivial task, and many methods exist. One way to solve the eigenvalue problem is to use a neural solution to the problem. The data is fed as the input, and the network converges to the wanted solution.

By ordering the eigenvectors in the order of descending eigenvalues (largest first), one can create an ordered orthogonal basis with the first eigenvector having the direction of largest variance of the data. In this way, we can find directions in which the data set has the most significant amounts of energy.

Suppose one has a data set of which the sample mean and the covariance matrix have been calculated. Let \mathbf{A} be a matrix consisting of eigenvectors of the covariance matrix as the row vectors. By transforming a data vector \mathbf{x} , we get

$$\mathbf{y} = \mathbf{A}(\mathbf{x} - \mu_{\mathbf{x}}) \quad (3.29)$$

which is a point in the orthogonal coordinate system defined by the eigenvectors. Components of \mathbf{y} can be seen as the coordinates in the orthogonal base. We can reconstruct the original data vector \mathbf{x} from \mathbf{y} by

$$\mathbf{x} = \mathbf{A}^T \mathbf{y} + \mu_{\mathbf{x}} \quad (3.30)$$

using the property of an orthogonal matrix $\mathbf{A}^{-1} = \mathbf{A}^T$. The \mathbf{A}^T is the transpose of a matrix \mathbf{A} . The original vector \mathbf{x} was projected on the coor-

dinate axes defined by the orthogonal basis. The original vector was then reconstructed by a linear combination of the orthogonal basis vectors.

Instead of using all the eigenvectors of the covariance matrix, we may represent the data in terms of only a few basis vectors of the orthogonal basis. If we denote the matrix having the K first eigenvectors as rows by \mathbf{A}_K , we can create a similar transformation as seen above

$$\mathbf{y} = \mathbf{A}_K(\mathbf{x} - \mu_{\mathbf{x}}) \quad (3.31)$$

and

$$\mathbf{x} = \mathbf{A}_K^T \mathbf{y} + \mu_{\mathbf{x}} \quad (3.32)$$

This means that we project the original data vector on the coordinate axes having the dimension K and transforming the vector back by a linear combination of the basis vectors. This minimizes the mean-square error between the data and this representation with given number of eigenvectors.

If the data is concentrated in a linear subspace, this provides a way to compress data without losing much information and simplifying the representation. By picking the eigenvectors having the largest eigenvalues we lose as little information as possible in the mean-square sense. One can e.g. choose a fixed number of eigenvectors and their respective eigenvalues and get a consistent representation, or abstraction of the data. This preserves a varying amount of energy of the original data. Alternatively, we can choose approximately the same amount of energy and a varying amount of eigenvectors and their respective eigenvalues. This would in turn give approximately consistent amount of information in the expense of varying representations with regard to the dimension of the subspace.

3.10 3D rotation matrix

When changing the point of view in a 3D geometry system, each point must be rotated and translated according to the current position and orientation of the person doing the viewing. This is sometimes called the camera position, or point of view (POV). Rotation and translation are usually accomplished using a pair of matrices, which will be called the Rotation Matrix R and the Translation Matrix T . These matrices are combined to form a Transform Matrix Tr by means of a matrix multiplication. Here is how it is represented mathematically [Gruber, 2000]:

$$R \cdot T = Tr \quad (3.33)$$

$$R = \begin{bmatrix} R_{11} & R_{12} & R_{13} & 0 \\ R_{21} & R_{22} & R_{23} & 0 \\ R_{31} & R_{32} & R_{33} & 0 \\ 0 & 0 & 0 & 1 \end{bmatrix} \quad (3.34)$$

$$T = \begin{bmatrix} 1 & 0 & 0 & X \\ 0 & 1 & 0 & Y \\ 0 & 0 & 1 & Z \\ 0 & 0 & 0 & 1 \end{bmatrix} \quad (3.35)$$

$$Tr = \begin{bmatrix} R_{11} & R_{12} & R_{13} & R_{11}X + R_{12}Y + R_{13}Z \\ R_{21} & R_{22} & R_{23} & R_{21}X + R_{22}Y + R_{23}Z \\ R_{31} & R_{32} & R_{33} & R_{31}X + R_{32}Y + R_{33}Z \\ 0 & 0 & 0 & 1 \end{bmatrix} \quad (3.36)$$

3.11 Spatiotemporal analysis

Following to *Hainzl and Fisher* [2002], the way to perform the analysis is (Figure 3.4): for the i th earthquake occurring at time t_i within the cluster sequence ($i = 1, \dots, N$), the areal extent of the activity (A_i) is measured by the convex envelope enclosing the earthquake epicenters $j = 1, \dots, i$ in the fault plane. As result, the time series $A(t_i)$ is obtained.

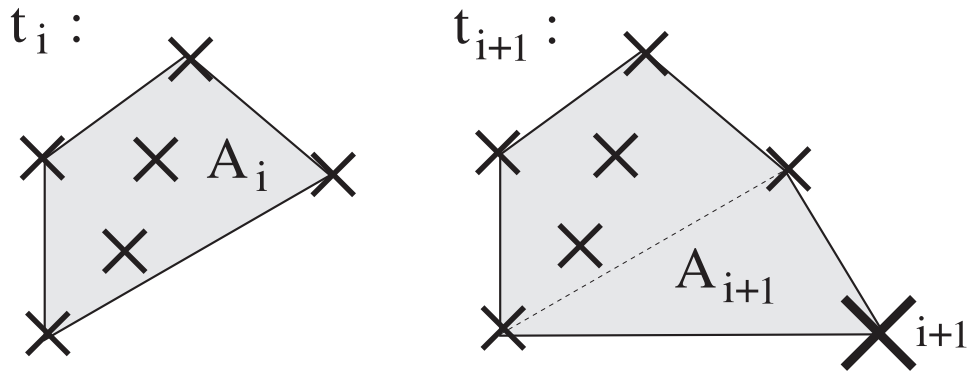


Figure 3.4: Schematic illustration of the data analysis scheme for two successive earthquakes after *Hainzl and Fisher* [2002]: the zone of the clusters activity is estimated by the are A enclosed by the convex envelope of epicenters (crosses).

3.12 Spatiotemporal migration

Physical background

Following to *Shapiro et al.* [1997] for explaining the physical background it is assumed that the state of stress in the crust is close to a critical one, that is the crust is in a failure equilibrium. Therefore, small perturbations of this state can lead to induced microseismicity. An increase of the pore pressure caused by fluid injection changes the effective normal stress as well as the friction coefficients of the rock mass. Thus, the temporal onset of the microseismicity relative to the beginning of the injection is interpreted as the time delay, Δt , necessary for the pore-pressure diffusion to cause a sufficiently large perturbation, Δp , of the pressure at a given distance, L , to trigger seismic events. The necessary value of Δp is a strongly fluctuating quantity and, therefore, the following rough estimate is usually used:

$$D \approx L^2/\Delta t \tag{3.37}$$

Chapter 4

Results-characterization of the West Fissure Fault System

4.1 Experiment set-up and data

To monitor the seismicity, a temporary seismic network covering an area of about 50 x 50 km was installed in November 2005 (Table 4.1, Figure 4.1). It has been recording continuously since then, and operation was maintained until November 2009. The network is located at around 21°S because of a series of geophysical observations at this latitude [*ANCORP Working Group*, 1999, 2003; *Yuan et al.*, 2000]. The seismic short-period network consists of twelve 3-component instruments (1 Hz MARK L4-3D seismometers and EDL PR6-24 data logger) which record continuously at a sample rate of 200 or 100 Hz, respectively, and in high/low gain (see Table 4.2 and 4.3).

Table 4.1: List of stations of the WFFS experiment

Station code	latitude [dd°mm.m']	longitude [dd°mm.m']	elevation [m]	recording started	recording finished
T04	20°56.022'	69°00.973'	2550	31.10.2005	14.11.2009
T05	20°55.997'	68°52.202'	3650	31.10.2005	14.11.2009
T06	20°53.756'	68°49.675'	4300	01.11.2005	08.12.2006
T07	20°55.436'	68°43.302'	4850	01.11.2005	07.11.2009
T08	20°47.767'	68°53.960'	3850	02.11.2005	20.07.2008
T09	20°59.339'	68°49.795'	4350	03.11.2005	30.12.2005
T10	21°05.050'	68°51.660'	3550	03.11.2005	06.12.2006
T11	21°03.716'	69°29.032'	900	04.11.2005	27.01.2006
T15	21°02.130'	69°29.265'	900	11.02.2006	12.06.2006

Continued on the next page

Station code	latitude [dd°mm.m']	longitude [dd°mm.m']	elevation [m]	recording started	recording finished
T17	20°39.195'	69°07.156'	2100	28.01.2006	15.11.2009
T18	20°42.711'	68°55.371'	3760	03.02.2006	18.08.2009
T19	20°50.578'	68°44.838'	4290	04.02.2006	08.12.2006
T20	20°44.803'	68°46.570'	4390	10.02.2006	18.08.2009
T21	21°01.711'	68°48.006'	4390	10.02.2006	09.03.2006
T22	21°01.729'	68°45.678'	4600	16.06.2006	24.11.2008
T23	20°36.547'	68°47.765'	4260	08.12.2006	18.08.2009
T24	20°48.455'	69°04.843'	2820	10.12.2006	08.11.2009
T25	20°49.214'	69°43.725'	4200	05.12.2007	07.11.2009
T26	21°12.409'	69°10.886'	1667	08.11.2008	13.03.2009

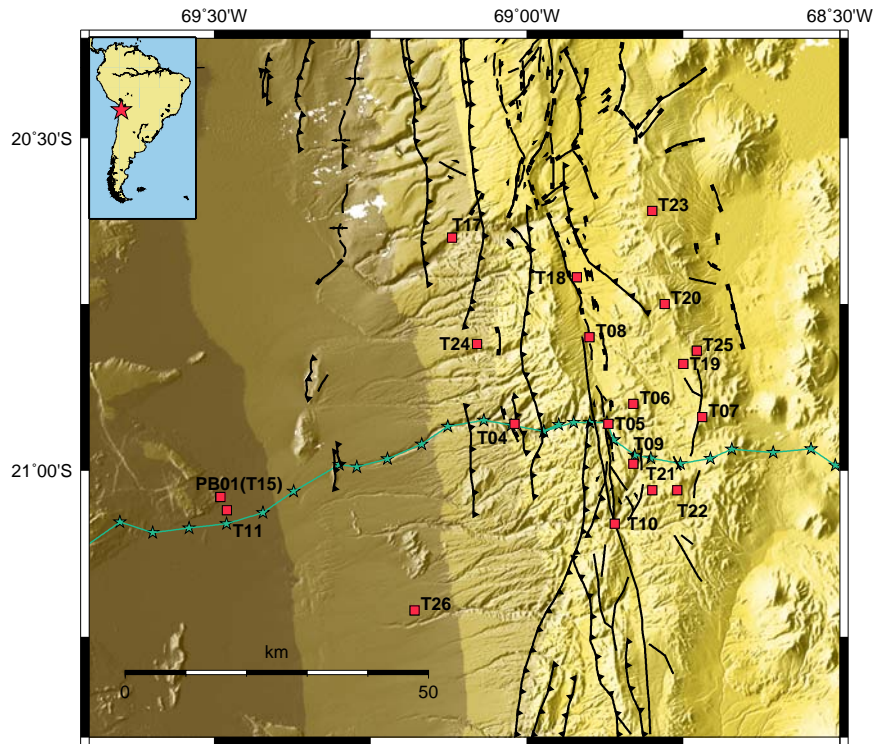


Figure 4.1: Local short period network around the West Fissure Fault System (WFFS). On the map the stations locations are plotted by red squares –the broad band station (PB01) from the IPOC network is in the same place that T15– and WFFS by black lines after *Reutter et al.* [1994], *Camus* [2003], *SERNAGEOMIN* [2003] and *Victor et al.* [2004]. The W-E crooked green line indicates the ANCORP profile with shot points (green stars).

Table 4.2: Configuration of record parameters in the stations of the WFFS network. The date (mm.yy) indicate the maintenance and change of hard disk, the configuration parameters can change with the next change in the hard disks.

Stations	10.2005	11.2005	01.2006	06.2006	12.2006	10.2007	12.2007	08.2008	11.2008	08.2009
T04	L	H	L	H	L	H	H	H	H	H
T05	L	H	H	H	H	H	H	H	H	H
T06	-	H	H	-	-	-	-	-	-	-
T07	-	H	H	H	H	H	H	H	H	H
T08	-	H	H	H	H	H	-	-	-	-
T09	-	H	-	-	-	-	-	-	-	-
T10	-	H	L	-	-	-	-	-	-	-
T11	-	L	-	-	-	-	-	-	-	-
T15	-	-	H	-	-	-	-	-	-	-
T17	-	-	H	H	H	H	H	H	H	H
T18	-	-	H	H	H	H	H	H	H	H
T19	-	-	H	L	H	-	-	-	-	-
T20	-	-	H	L	H	L	H	H	H	-
T21	-	-	H	H	-	-	-	-	-	-
T22	-	-	-	L	H	L	H	H	H	-
T23	-	-	-	-	H	L	H	L	L	L
T24	-	-	-	-	H	H	H	H	H	H
T25	-	-	-	-	-	-	H	L	H	H
T26	-	-	-	-	-	-	-	-	H	-

H: the station recorded at high gain and 200 Hz, L: low gain and 100 Hz

The activities were concentrated around the West Fissure Fault System, so far the observations until November 2009 have been processed producing detailed information related to seismicity, stress distribution, and crustal structures located there.

The continuous data streams, recorded in miniseed format, were processed in the lab detecting 1427 events within the network and its immediate vicinity.

The events were determined using NonLinLoc (see chapter 3 for further information) and the model used in the computations is a regional 2-D V_P model (Figure 4.2) inferred from active seismics [Lüth, 2000].

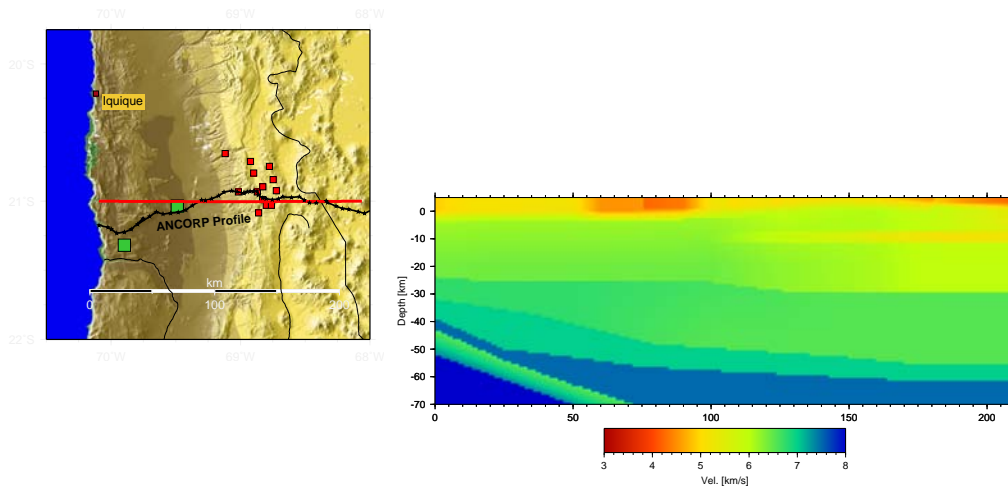


Figure 4.2: The 2-D P -velocity model by Lüth [2000]. On the left: the straight red line indicates the position of the velocity model, the black line and crosses indicate the ANCORP profile, the red squares indicate some short period stations from WFFS network, and the green squares indicate the broad band stations from the IPOC network. On the right: The cross section view of the 2-D P -velocity model, the colors indicate the different velocities (see the colors bar).

In order to investigate the seismic clusters and focal mechanisms a database was built by SEISAN package [Havskov and Ottemöller, 2000]. P and S arrivals, first motion polarities, SV/P , SH/P , SH/SV amplitudes ratio and amplitudes for local magnitude determination were hand-picked.

Table 4.3: Calibration parameters for WFFS stations

Parameter	H	L
	high gain	low gain
Natural period	1 [Hz]	1 [Hz]
Seismometer damping ratio	0.7	0.7
Sensor loaded generator const.	180 [Vs/m]	180 [Vs/m]
Recording media gain	1000000 [count/V]	1000000 [count/V]
Digitalizer sample rate	200 [Hz]	100 [Hz]
Amplifier gain	20 [dB]	0 [dB]

calibration parameters for Mark L4-3D and EDL PR6-24 data logger

4.2 The observed seismicity

The configuration of the seismological network was thought in order to record with a good quality events located around the WFFS in a range of depth that permit to cover the shallow and intermediate crust (an example of this kind of event is shown in the Figure 4.3). However the high quality records were also obtained for events that occurred below the Longitudinal Valley and the Nazca plate (Figure 4.4).

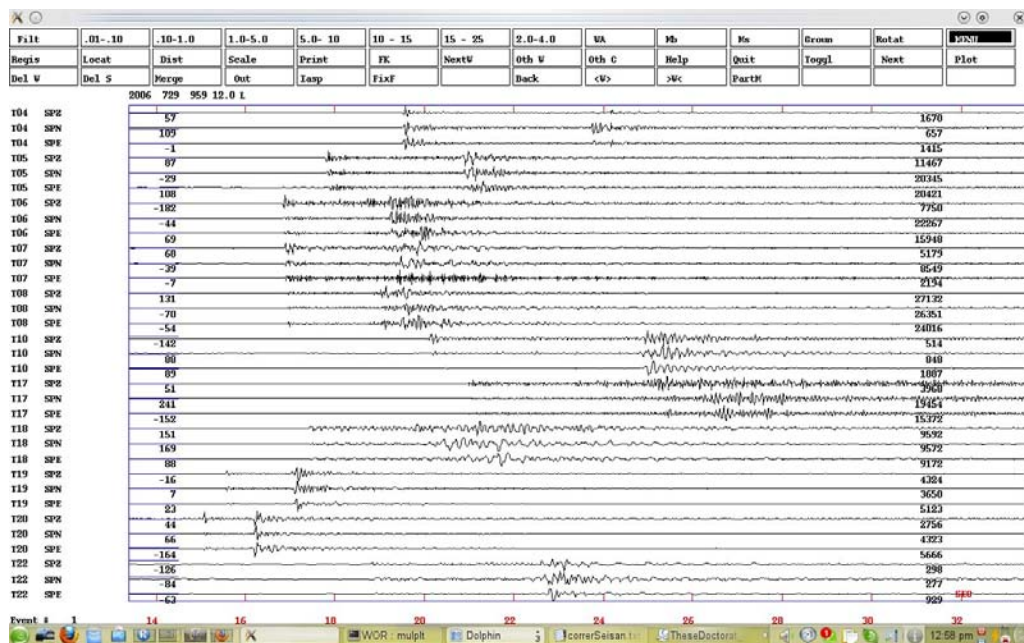


Figure 4.3: An example of a shallow event (1 km, $M_L = 1.7$) registered by the WFFS network in 2006.07.29 at the east flank of the Precordillera.

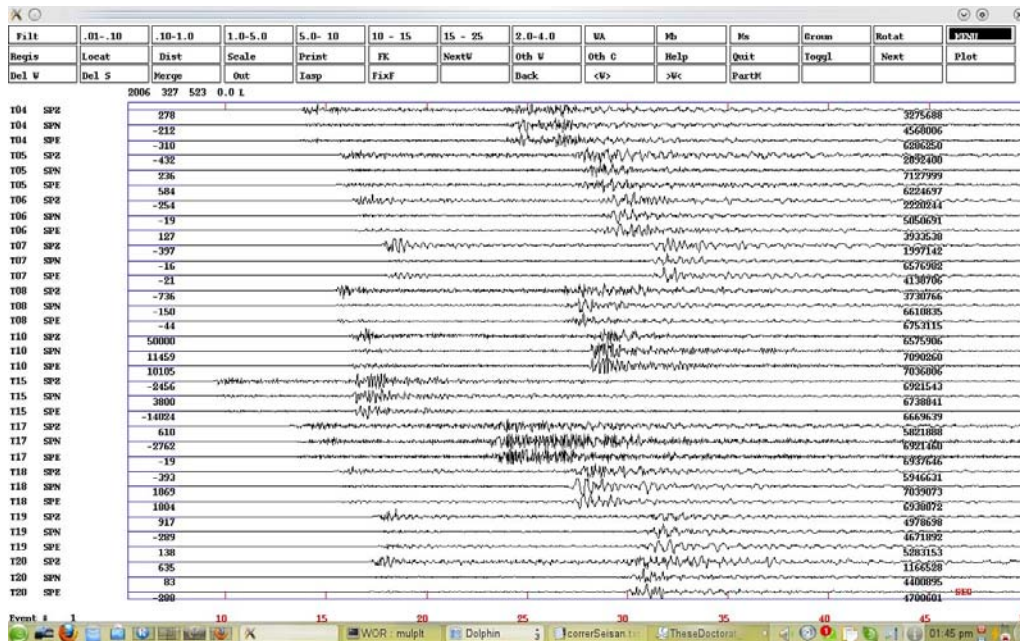


Figure 4.4: An example of a deeper event (53.8 km, $M_L = 5.5$) registered by the WFFS network in 2006.03.27 at the Longitudinal Valley near to the Nazca plate.

Thus about 1430 local seismic events with magnitudes of $-0.7 \leq M_L \leq 4.1$ and focal depths between ~ 4 km above sea level and ~ 110 km below it have been located (only few earthquakes from the subduction zone are incorporated).

A normalized density of event per day was calculated in order to determine, in a monthly average, how many events occur in a day (Figure 4.5). The normalization considered the number of events per day in a particular month, divided by the number of days in this month. Thus the average is calculated for each month given an idea of the amount of seismic activity occurred during the monitoring.

It is also possible determine the average associated to the complete period of monitoring, which reaches to 0.98 considering 48 month of registers. This average becomes smaller (0.81), if in the calculations are not considered the months associated to cluster activity (swarm and SW cluster). The significant influence that the swarm activity (phase B', see Figure 4.7 for further information) has in the value of the monthly average for April 2006 is clear (Figure 4.5), the other high values of this average are related to the swarm (phase B''), and the SW cluster (see Figure 4.7 for further information). Other months with high values are 10.2007 and 09.2008, which are not related with the cluster activity.

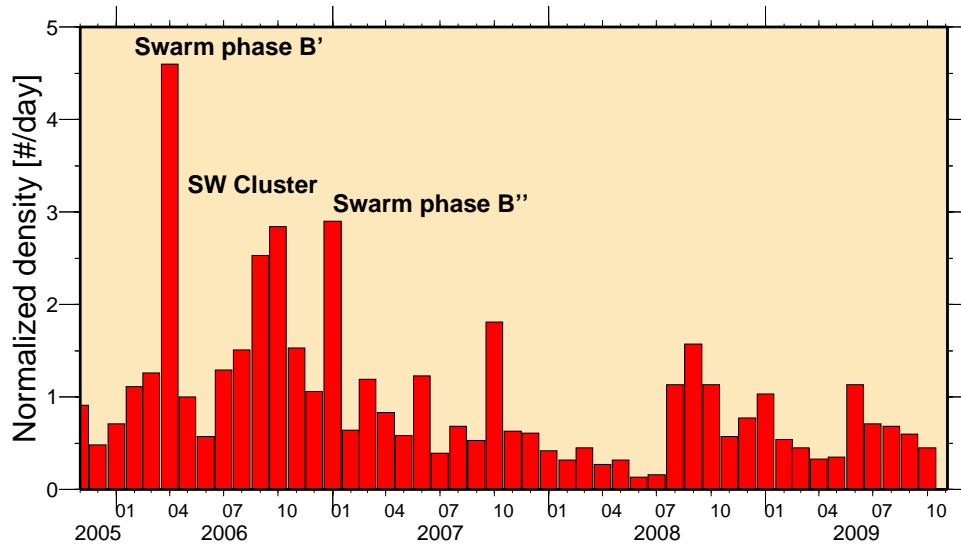
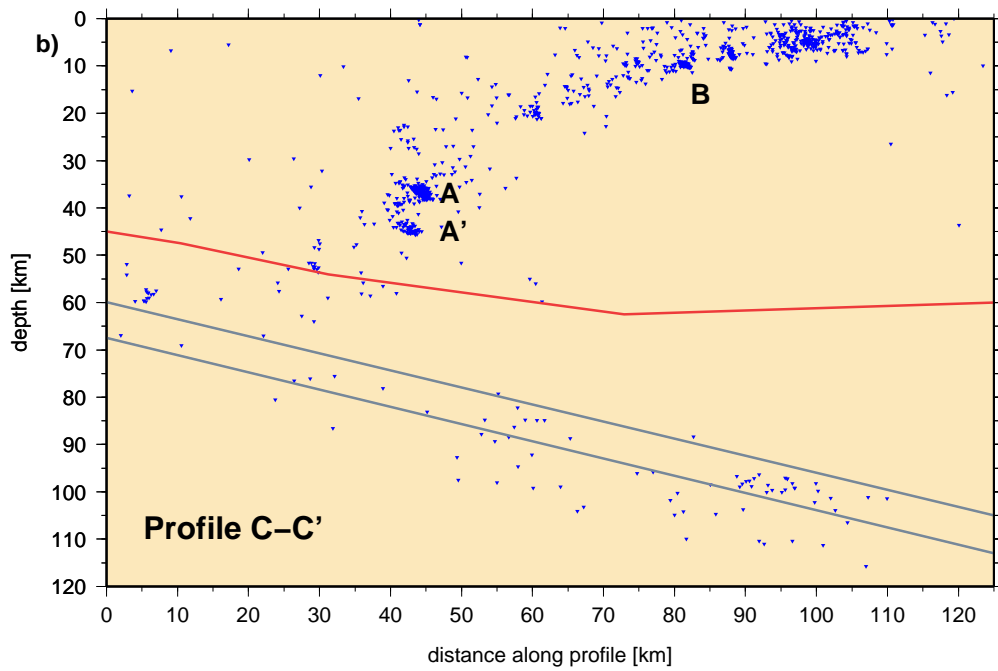
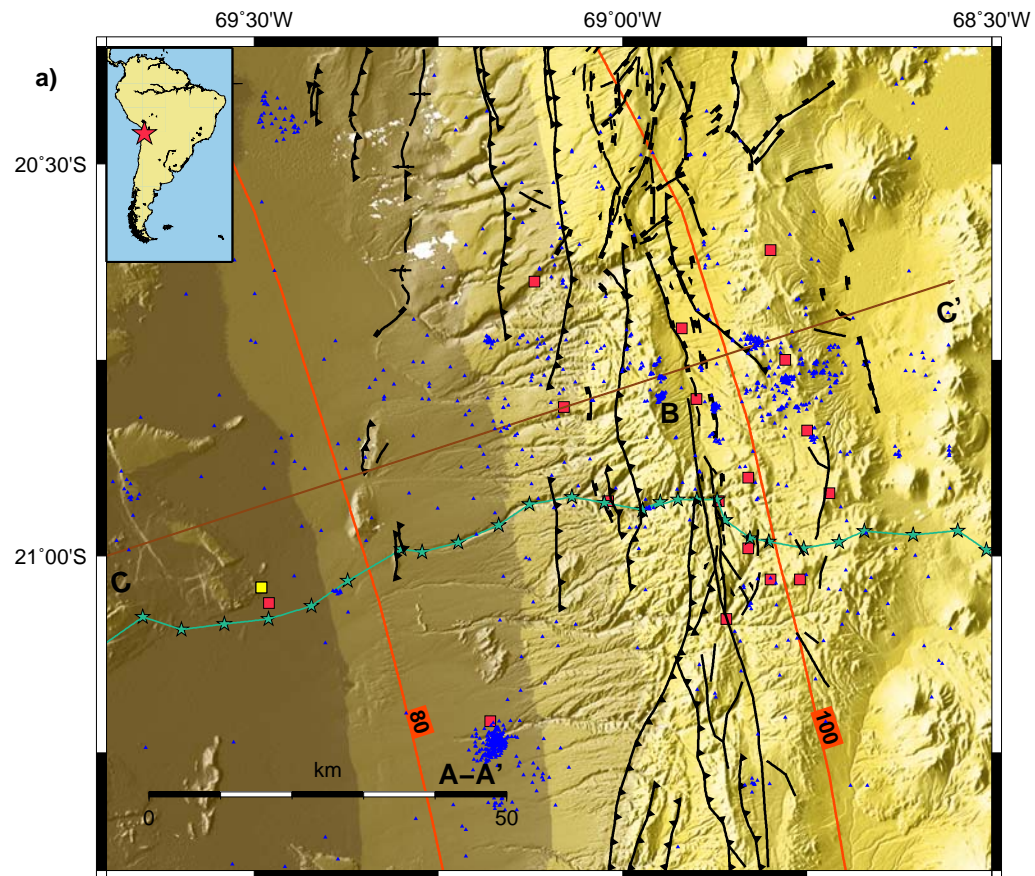


Figure 4.5: Normalized density of event per day as a function of time. Note that the major influence is due to the cluster activity (Swarm and SW cluster).

The spatial distribution of the seismicity shows that a large amount of events are concentrated in the shallow crust and partly associated with the surfaces traces of the known branches of the WFFS, however the seismicity appears scattered westward below the Longitudinal Valley, except in the northern and southern boundaries of the study area (Figure 4.6a).

The W-E section (Figure 4.6b) shows that the eastern flank of the Pre-cordillera, near to the C-C' profile shown on the map view, concentrates a high density of shallow events which are not apparently related to earthquake

Figure 4.6 (on the next page): Local seismicity around the West Fissure Fault System (WFFS) detected during 48 months of monitoring (11/2005-11/2009). On the map (a), the short period 3-D stations locations are shown by red squares, broad band stations from the IPOC network by yellow squares, and WFFS by black lines after *Reutter et al.* [1994], *Camus* [2003], *SERNAGEOMIN* [2003] and *Victor et al.* [2004]. The W-E crooked green line indicates the ANCORP profile with shot points (green stars). Earthquake locations are plotted by blue triangles; seismicity related to the Nazca subduction is partially plotted. The orange line indicates the 80 and 100 km isodepths of the seismicity in the Wadati-Benioff zone after *Schurr* [2000]. The brown line (C-C') indicates the profile N72E, which is perpendicular to the isodepth. The cluster zones are indicated by A, A' and B, respectively. The cross section (b) shows the earthquake locations projected on the C-C' profile, the red line indicates the continental Moho, and the grey lines indicate the top and bottom of the Nazca plate (both after *Yuan et al.* [2000]).



clusterization.

The scattered events below the Longitudinal Valley define in depth a distinct lower boundary of the seismicity, which is dipping to the west. An interesting point to note is the virtual absence of shallow events in the Longitudinal Valley, being the seismicity concentrated in the narrow band described above (Figure 4.6b).

Among the seismic activity, two seismic clusters were detected. The SW cluster, below the Longitudinal Valley, was separated into two subclusters (A and A') at 35 and 40 km depth, respectively. The subcluster (A) consists of 224 events occurring between 6 January 2006 and 4 July 2009, with a magnitude distribution of $0.1 \leq M_L \leq 4.1$ (Figure 4.7a and 4.7b). The subcluster (A') consists of 38 events occurring between 19 October 2006 and 13 March 2008; its magnitude distribution is $0.3 \leq M_L \leq 2.3$ (see chapter 3 for further information of magnitude determination).

The other cluster (B) in the central part at ~ 9 km depth with 185 events occurred between 23 February 2006 and 4 December 2007; its magnitude distribution is $-0.4 \leq M_L \leq 3.0$ (Figure 4.7c). It can be separated into two phases (B' and B'').

The cluster (B) exhibits characteristics of an earthquake swarm [Wigger *et al.*, 2007] with the majority of events having very high cross correlation coefficients (greater than 0.8, see Figure 4.8). As the waveform similarity is so high, these events must be located within a small volume (Figure 4.9). The maximum inter-event distance is in the order of 1 km.

It may also be speculated that this swarm was triggered by a magnitude $M_L = 5.5$ event occurring nearby at the Nazca plate; both events are very close in time.

The temporal continuity of these different clusters could be related to migration processes of fluids through the crust. A detailed study of these clusters and their relation with fluid flows from lower to upper crust will be the subject of the next chapter.

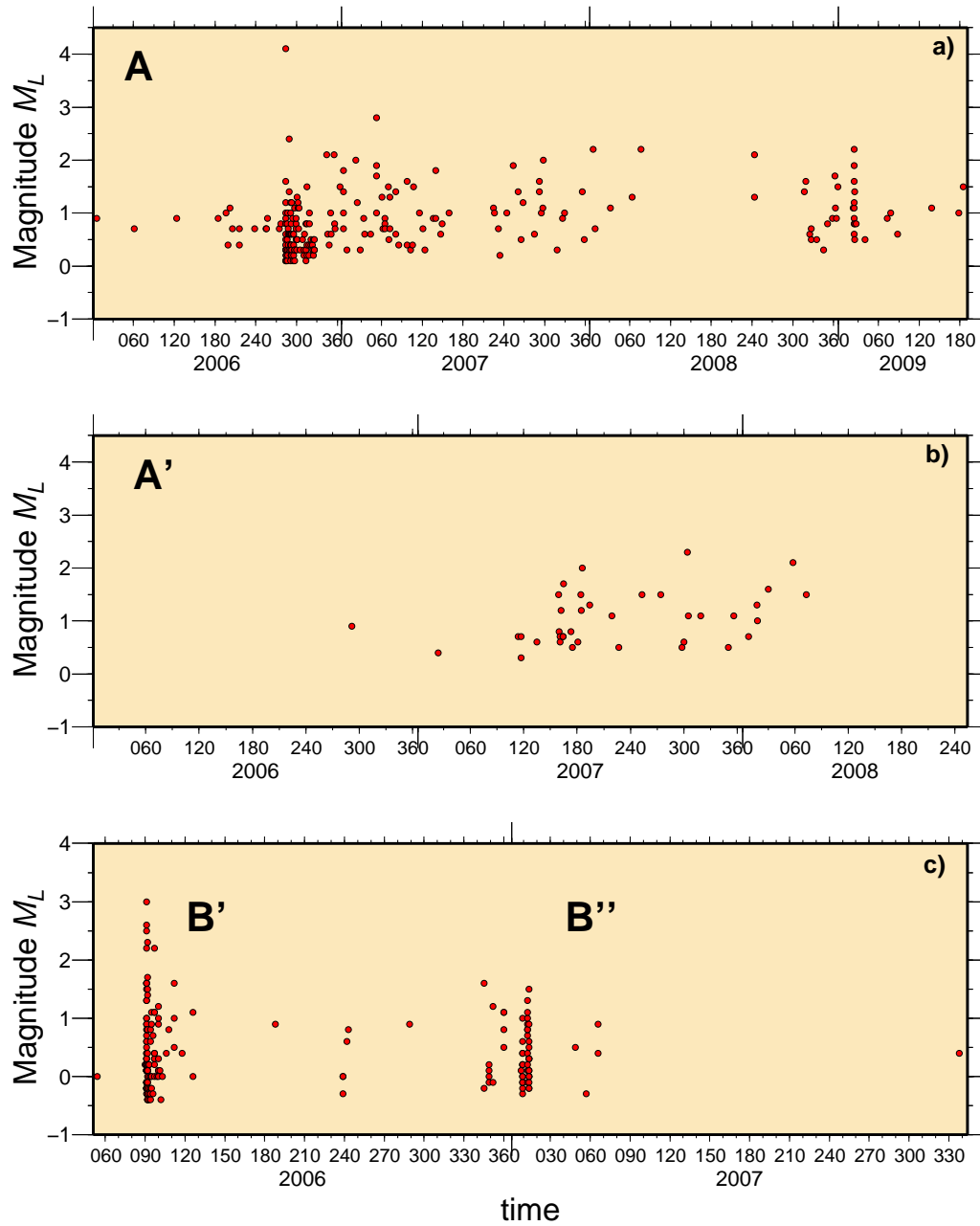


Figure 4.7: The magnitude of the clusters is shown as a function of time. Subfigures (a) and (b) show the distribution in the subclusters A and A', respectively. Subfigure (c) shows the distribution in the swarm B; the capital letters B' and B'' indicate that the swarm can be divided into two phases.

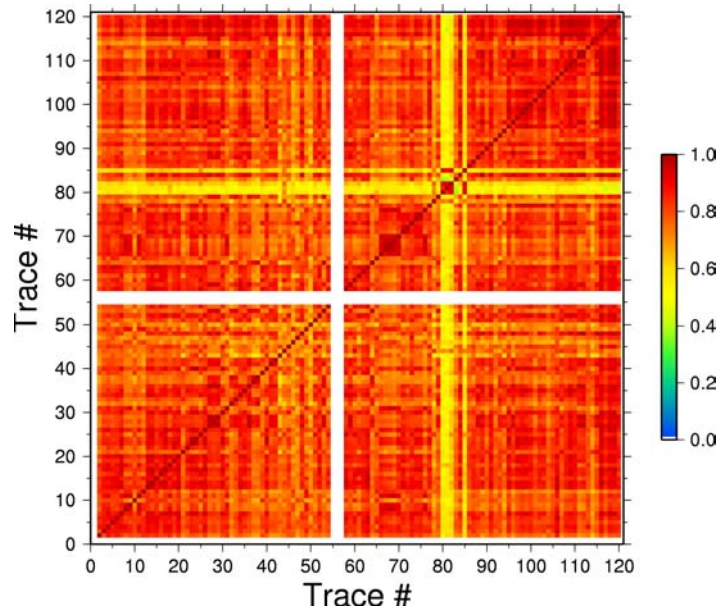


Figure 4.8: The correlations coefficients for the central cluster (Swarm).

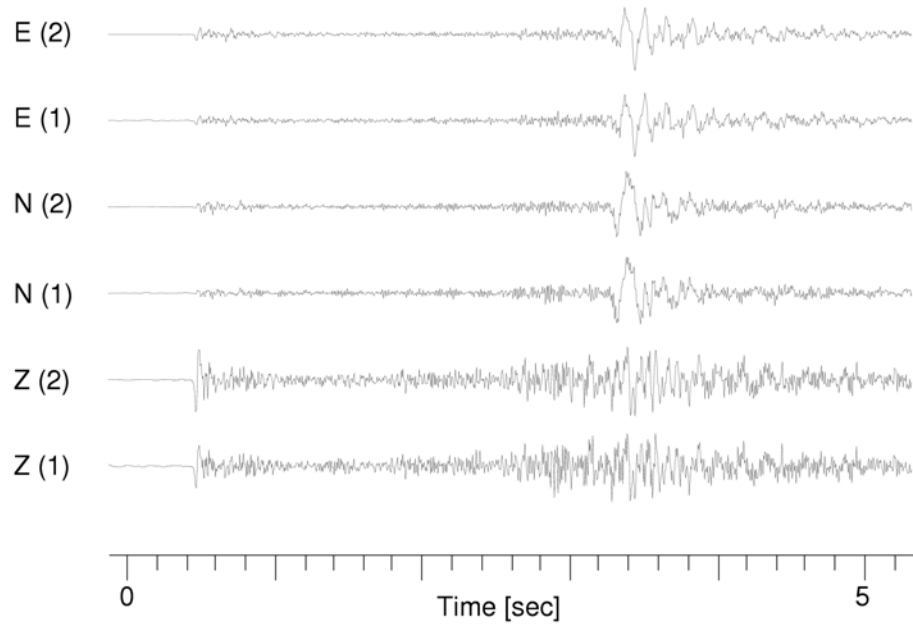


Figure 4.9: An example of waveform similarity for the central cluster (Swarm).

4.3 Focal mechanisms-data processing and results

The focal mechanisms and a stress tensor analysis were used to characterize the WFFS in term of its kinematic behavior. Using a high accuracy quality criterion, well-located events ($rms \leq 0.2$) and a minimum of 7 unambiguous P -wave polarities, a total of 228 events was selected for the calculation of the focal mechanisms.

Not only were the focal mechanisms calculated in base to the polarities of P -wave arrival, but also the amplitude ratios of SV/P , SH/P and SH/SV [Snoke, 2003] were used in the calculation (Figure 4.10, see chapter 3 for further information).

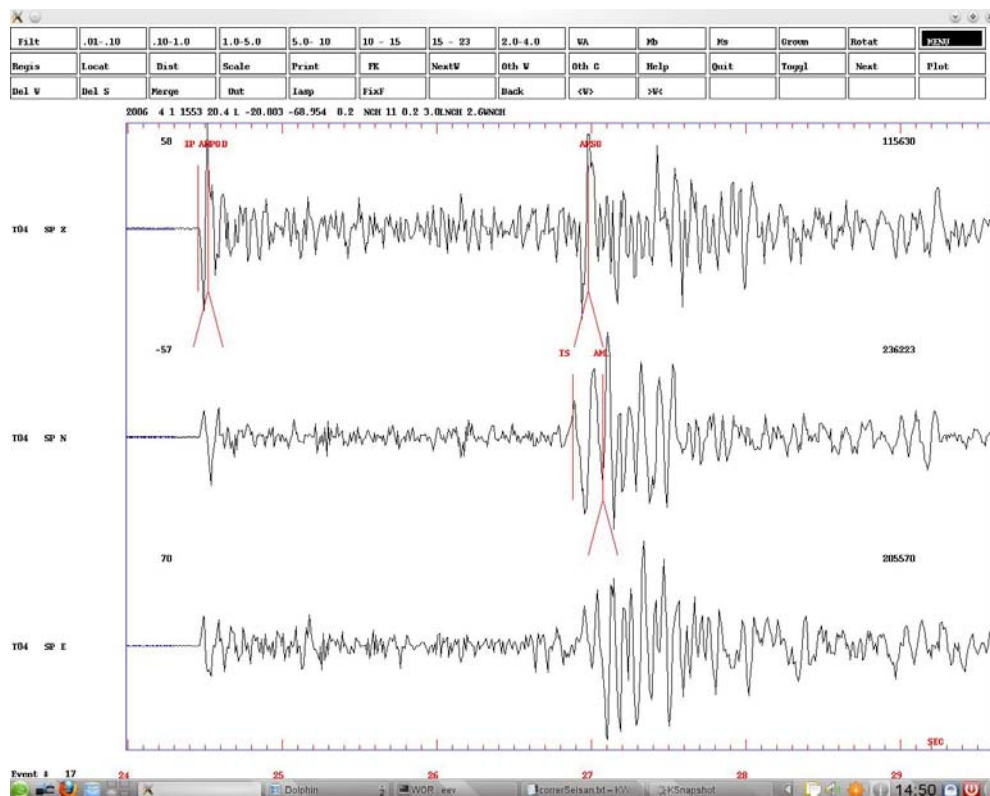


Figure 4.10: An example of hand-picked P and S arrivals for a single station using SEISAN [Havskov and Ottemöller, 2000]. IP means impulsive P , AMPG indicates amplitude for P used in the calculation of SV/P amplitude ratio, D indicates polarity (dilatation), IS indicates impulsive S , AML indicates amplitude for local magnitude, AMSG indicates amplitude for SV used in the calculation of SV/P amplitude ratio.

The amplitudes ratio were measurement after a band pass filter of 1.0–5.0 Hz were applied and a rotation of the horizontal components of the seismogram was done. The SV and SH amplitudes ratio were hand-picked on the vertical [according to *Kisslinger et al.*, 1982] or radial component, in the case of the SV , and transverse components for the SH (Figure 4.11 and 4.12, see chapter 3 for further information).

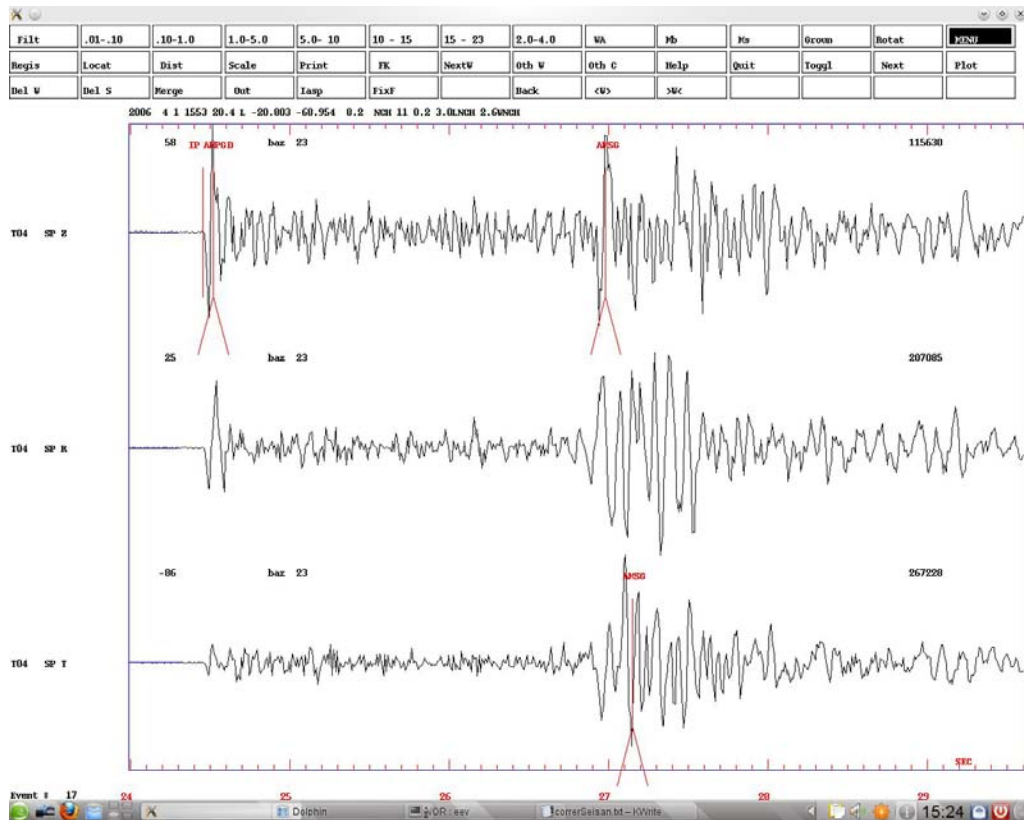


Figure 4.11: An example of rotation of seismogram in vertical, radial and transverse components for a single station using SEISAN [*Havskov and Ottemöller*, 2000]. IP means impulsive P , AMPGD indicates amplitude for P used in the calculation of SV/P amplitude ratio, D indicates polarity (dilatation), AMSG in the vertical component indicates amplitude for SV used in the calculation of SV/P amplitude ratio. AMSG in the transverse component indicates amplitude for SH used in the calculations of SH/P and SH/SV amplitude ratios.

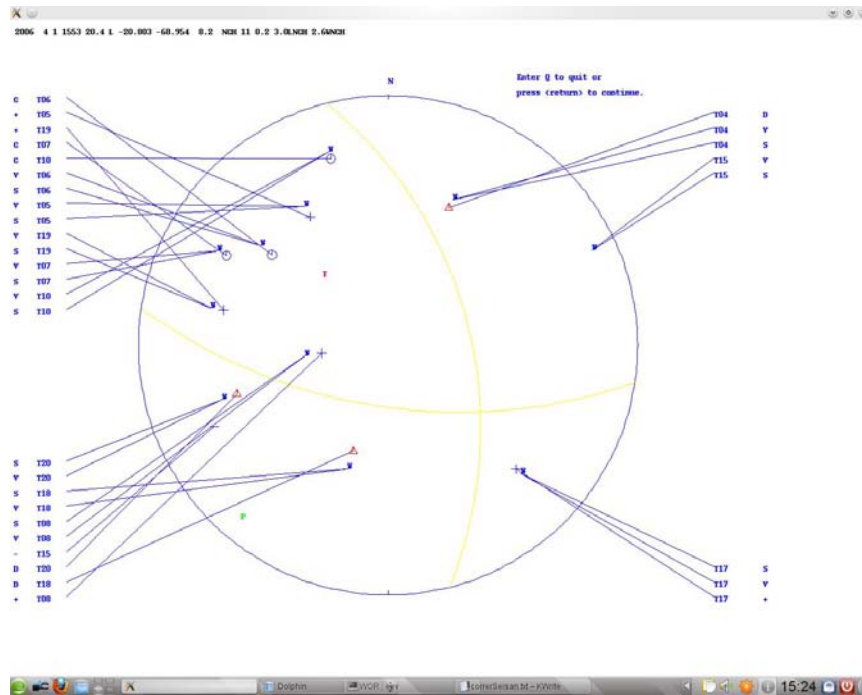
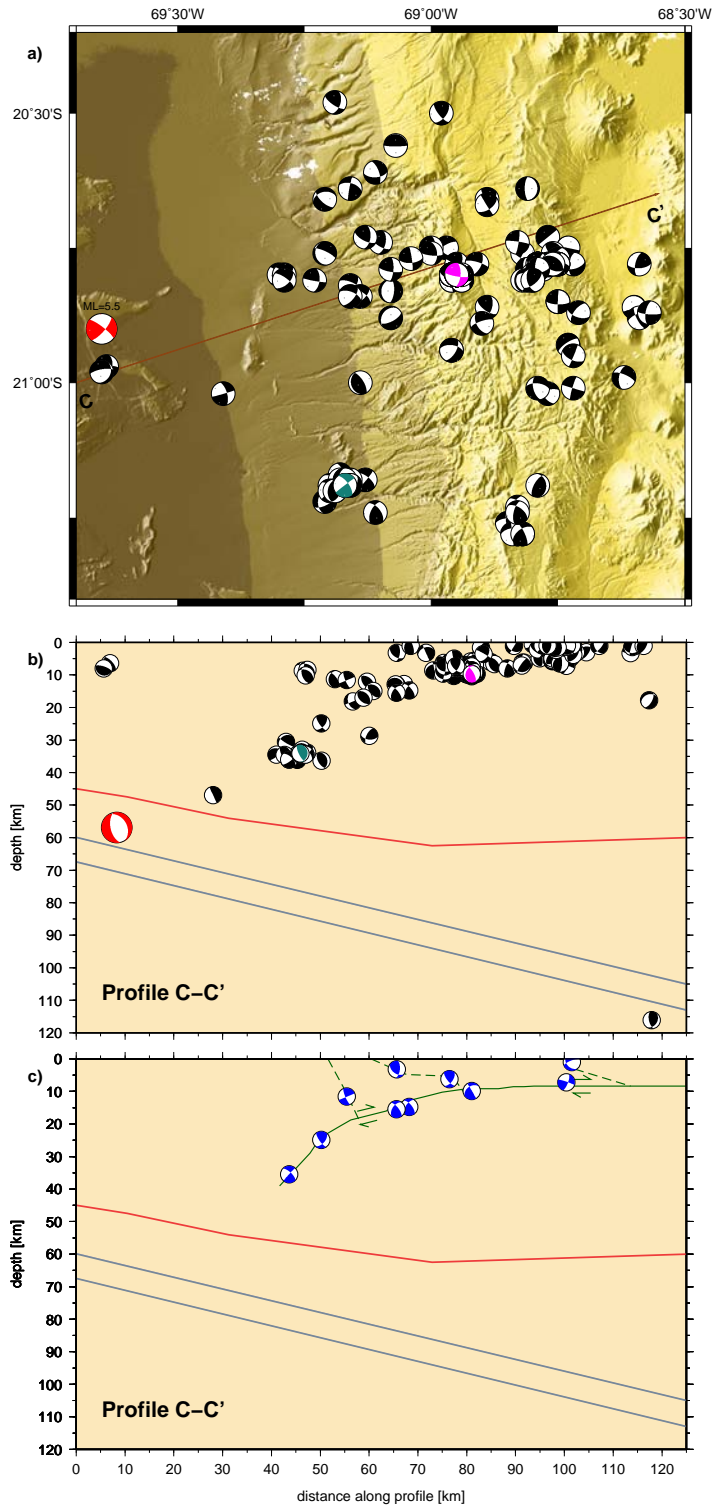


Figure 4.12: An example of calculation of the focal mechanism using SEISAN [Havskov and Ottemöller, 2000]. T indicates T -axis, P indicates P -axis. The circles and + symbols indicate stations with compression in their P -wave arrivals. Triangles and – symbols indicate dilatation in their P -wave arrivals. V indicates amplitude ratio SV/P . S indicates amplitude ratio SV/SH .

Figure 4.13a and 4.13b show the great variety in the focal mechanisms calculated, which occur without a clear particular trend, but the analysis in detail shows that the majority of the events have an oblique mechanism with many of them show almost strike-slip movements.

Figure 4.13 (on the next page): The map (a) shows the focal mechanisms (FM) calculated. The red FM indicate a $M_L = 5.5$ event near to the Nazca plate that occurred 72 hours before the swarm activity began. The biggest events for the swarm and cluster are indicated by magenta and dark green FM, respectively. The brown line (C-C') indicates the N72E profile. The cross sections (b) show the FM projected in the C-C' profile. The cross section (c) shows the FM for the deeper events which support the idea of a deep reverse structure; the green lines indicate this possible structure. Dashed green lines indicate the shallow reverse structures that have also been recognized in geological studies (see Fig. 4.40). The red line in (b) and (c) indicates continental Moho, and the grey lines in (b) and (c) indicate the top and bottom of the Nazca plate (both after [Yuan *et al.*, 2000]).



On the other hand, when the deeper events were plotted (Figure 4.13c), they show a possible reverse structure, which acts as the lower boundary of the seismicity. It is also possible to correlate some shallow focal mechanisms to the structural pattern found to the west flank of the Precordillera [Reutter *et al.*, 1994; Victor *et al.*, 2004; Farías *et al.*, 2005].

4.4 Stress tensors

The stress tensors were calculated using *Rivera and Cisternas* [1990] method, which calculate the direction and the shape of the stress tensor from already determined focal mechanisms of the earthquakes. A score of successfully predicted polarities is given to appreciate the quality of the inversion (see the chapter 3 for further information).

Recent neotectonic and geological studies in the area [Victor *et al.*, 2004; Janssen *et al.*, 2002] show that N-S trending thrust faults and monoclinial flexures dominate at the base and the western flank of the Precordillera, indicating W-E directed shortening, whereas the eastern flank of the Precordillera is dominated by normal and strike-slip faults indicating NW-SE directed extension with dextral strike-slip motion along N-S trending faults.

Owing to the complex tectonic frame and the great variety of focal mechanisms, two ways of calculating stress tensors were considered. In the first, a single stress tensor was calculated in order to explain all the focal mechanisms in the area, i.e., the regional stress tensor. For the second way, the study area was divided according to the tectonic context, and solutions were calculated for each subarea (Figure 4.14).

The single solution for the stress tensor (Figures 4.15 and 4.21, Table 4.4) shows a rotation of the principal stresses considering that the study area is in a convergence margin; the stress direction σ_2 (instead of σ_1) is very close to the horizontal and compatible with the regional plate motion direction of $\sim 80^\circ$ [Somoza, 1998]. Thus the regional stress tensor solution indicates a tensional regime for the study area.

However, analysis of the stress field for each tectonic subarea shows changes in the stress tensors. Despite of the results for the inversion of the stress tensor in the different subareas show a moderately scattering, indicating that the solutions are not well-constrained, the best solution for each subarea is in agreement with the different tectonic signatures which are produced on each side of the mean trace of the WFFS [David *et al.*, 2002; Victor *et al.*, 2004; Janssen *et al.*, 2002].

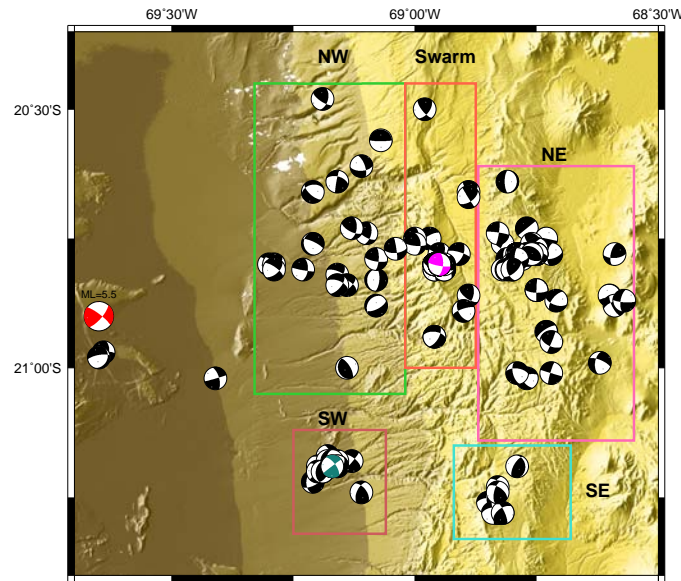


Figure 4.14: The map shows the study area divided in different zones according to the tectonic context, the focal mechanisms (FM) included in the inversion of the stress tensor is also shown. The red FM indicate a $M_L = 5.5$ event near to the Nazca plate that occurred 72 hours before the swarm activity began. The biggest events for the swarm and cluster are indicated by magenta and dark green FM.

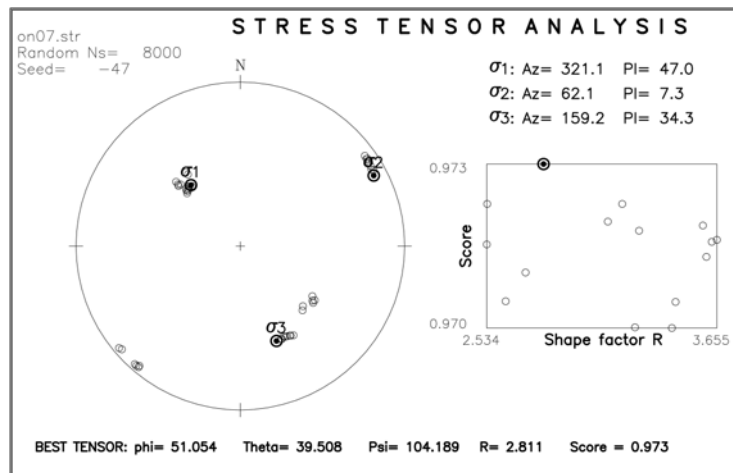


Figure 4.15: Regional stress tensor for the study area. σ_1 , σ_2 , and σ_3 indicate the principal stresses. The orientation of the eigen direction of stress tensor are defined by three Euler's angles (phi, theta and psi) using the definition of *Goldstein* [1959], angle of passage from the geographic coordinates (north, east and down-vertical) to the eigen direction of the stress tensor. Az and Pl indicate azimuth and plunge, respectively. The solution indicates a tensional regime due to σ_1 is closer to the vertical axis.

Thus, the results of the inversion show that the NW and SW subareas have a stress tensor with a major compressive stress direction σ_1 close to horizontal direction (Figures 4.16, 4.17 and 4.21, Table 4.4), compatible with the regional plate motion direction [Somoza, 1998]. The results suggest a compressive tectonic context that acts obliquely over pre-existing structures in a N-S direction, causing a transpressional regime in these structures.

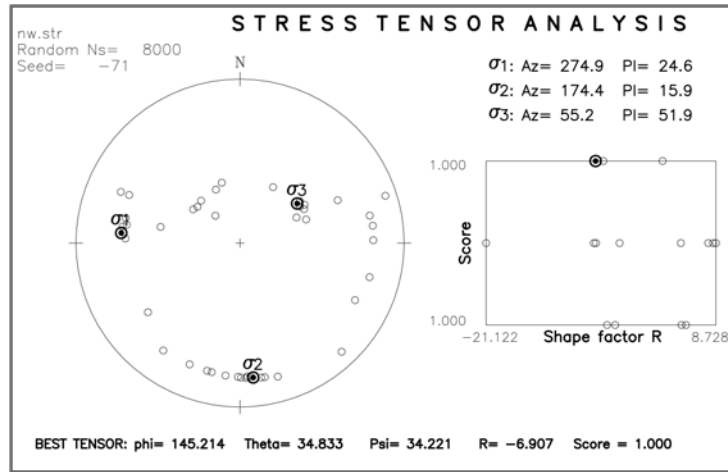


Figure 4.16: Stress tensor for the NW subarea. σ_1 , σ_2 , and σ_3 indicate the principal stresses. The orientation of the eigen direction of stress tensor are defined by three Euler's angles (phi, theta and psi) using the definition of Goldstein [1959], angle of passage from the geographic coordinates (north, east and down-vertical) to the eigen direction of the stress tensor. Az and Pl indicate azimuth and plunge, respectively. The solution indicates a compressional regime due to σ_3 is closer to the vertical axis.

Table 4.4: List of the parameters describing the stress tensor solutions

Zone	σ_1 (Az/Pl)	σ_2 (Az/Pl)	σ_3 (Az/Pl)	R	Score
Single	321.1/47.0	62.1/7.3	159.2/34.3	2.811	0.973
NW	274.9/24.6	174.4/15.9	55.2/51.9	-6.907	1
SW	227.1/30.5	132.1/6.0	31.4/51.5	-14.870	1
SE	330.3/49.7	210.5/17.4	108.5/25.6	4.796	1
NE	251.6/12.8	17.3/62.4	156.1/16.4	0.231	0.978
Swarm	326.0/48.1	221.3/9.4	122.9/32.3	6.488	1

(Az/Pl) mean azimuth/plunge

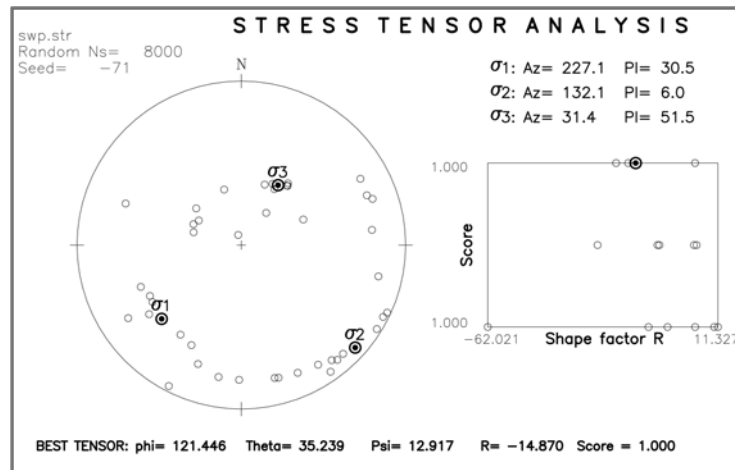


Figure 4.17: Stress tensor for the SW subarea. σ_1 , σ_2 , and σ_3 indicate the principal stresses. The orientation of the eigen direction of stress tensor are defined by three Euler's angles (phi, theta and psi) using the definition of *Goldstein* [1959], angle of passage from the geographic coordinates (north, east and down-vertical) to the eigen direction of the stress tensor. Az and Pl indicate azimuth and plunge, respectively. The solution indicates a compressional regime due to σ_3 is closer to the vertical axis.

The stress fields in the swarm and SE zones also show a rotation of the principal stress like the single solution (Figures 4.18, 4.19 and 4.21, Table 4.4), indicating a tensional regime that also acts obliquely over pre-existing structures in a N-S direction, causing a transtensional regime in these structures.

The NE subarea (Figures 4.20 and 4.21, Table 4.4) shows a stress tensor with a σ_1 stress direction compatible with the regional plate motion direction [*Somoza*, 1998]. The σ_2 is oblique to the vertical direction, indicating a strike-slip regime in the zone.

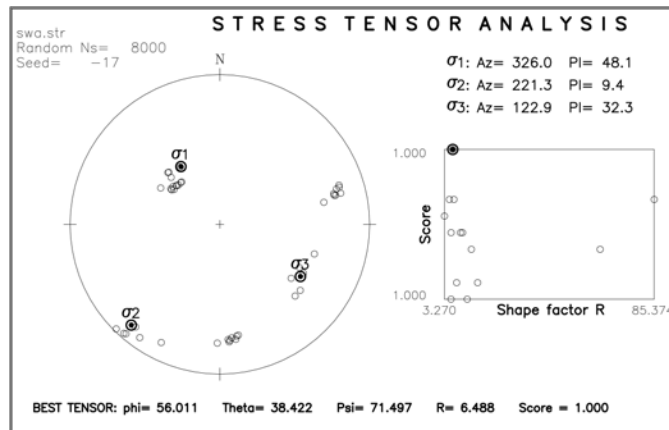


Figure 4.18: Stress tensor for the swarm subarea. σ_1 , σ_2 , and σ_3 indicate the principal stresses. The orientation of the eigen direction of stress tensor are defined by three Euler's angles (phi, theta and psi) using the definition of *Goldstein* [1959], angle of passage from the geographic coordinates (north, east and down-vertical) to the eigen direction of the stress tensor. Az and Pl indicate azimuth and plunge, respectively. The solution indicates a tensional regime due to σ_1 is closer to the vertical axis.

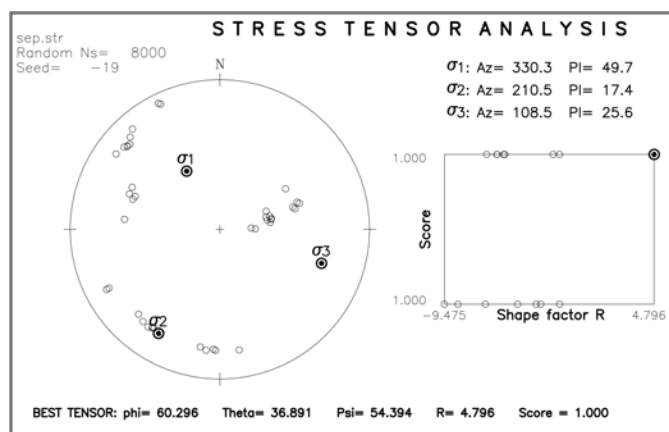


Figure 4.19: Stress tensor for the SE subarea. σ_1 , σ_2 , and σ_3 indicate the principal stresses. The orientation of the eigen direction of stress tensor are defined by three Euler's angles (phi, theta and psi) using the definition of *Goldstein* [1959], angle of passage from the geographic coordinates (north, east and down-vertical) to the eigen direction of the stress tensor. Az and Pl indicate azimuth and plunge, respectively. The solution indicates a tensional regime due to σ_1 is closer to the vertical axis.

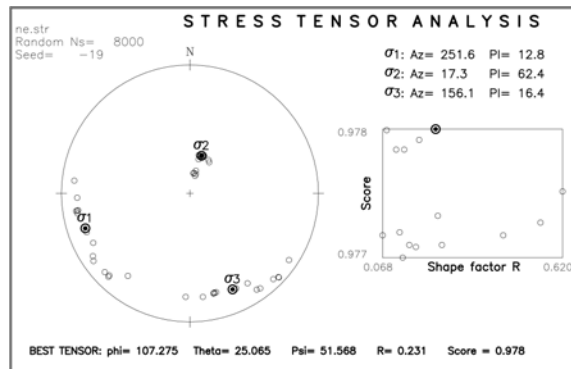


Figure 4.20: Stress tensor for the NE subarea. σ_1 , σ_2 , and σ_3 indicate the principal stresses. The orientation of the eigen direction of stress tensor are defined by three Euler's angles (phi, theta and psi) using the definition of *Goldstein* [1959], angle of passage from the geographic coordinates (north, east and down-vertical) to the eigen direction of the stress tensor. Az and Pl indicate azimuth and plunge, respectively. The solution indicates a strike-slip regime due to σ_2 is closer to the vertical axis.

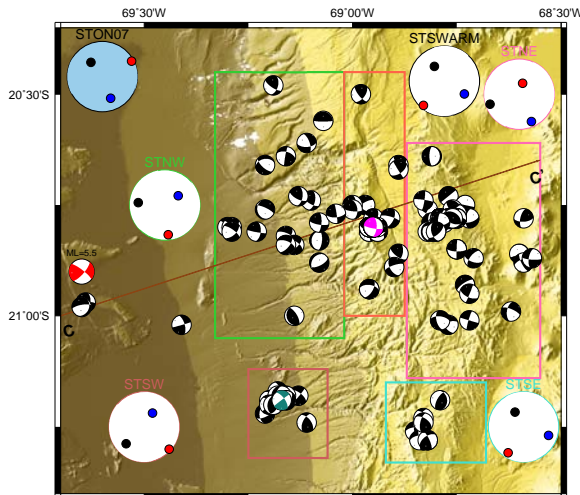


Figure 4.21: The map shows the focal mechanism (FM) and the stress tensors (ST) for the indicated zones (green NW, pink NE, red SW, dark green SE and orange SWARM) and the regional ST (blue filled circle). In the ST the black dots represent σ_1 , red dots represent σ_2 and blue dots represent σ_3 . The red FM indicate a $M_L = 5.5$ event near to the Nazca plate that occurred 72 hours before the swarm activity began. The biggest events for the swarm and cluster are indicated by magenta and dark green FM, respectively. The brown line (C-C') indicates the N72E profile.

4.5 Moment tensor analysis

For most tectonic earthquakes, material failure by shearing along a fault surface. Such seismic sources are called shear sources. They are described by double-couple (DC) components of moment tensors. In addition to DC components, non-double-couple moment tensor components have been frequently reported. They are often attributed to noisy data and/or to effects that are due to mismodelling of the wavefield by unknown earth's structure. In other cases, mainly in regions of earthquake swarm activity or in volcanic areas, they are related to volumetric source changes that may happen by additional opening or closure of the fault surface during faulting. These events are called tensile earthquake. Possible scenarios causing such phenomena include magmatic dyke intrusion or injection of high-pressure fluids into a fault during rupturing.

In order to find a possible source (or sources) for the earthquake clusterization, a moment tensor analysis was carried out.

Due to the volumetric part – in a full moment tensor inversion – is very problematic to recover, a deviatoric moment tensor inversion was performed.

The percentage of the non-double-couple components was specially taken in consideration due to they can indicate the presence of fluids in the source.

Thus, the waveform analyzed here were taken from the short-period three component WFFS network and analyzed by ISOLA code [Sokos and Zahradník, 2008]. They are representative of the largest event of both the swarm and the subcluster A (see the chapter 3 for further information).

The hypocenters determination were performed using NonLinLoc [Lomax *et al.*, 2000], which are based on the P - and S -waves arrival times and the crustal 2D velocity model of Lüth [2000](Table 4.5; see chapter 3 for further information).

Table 4.5: Precise location by NonLinLoc method

Event	Origin time [hh:mm:ss]	Lat [deg]	Lon [deg]	Depth [km]	M_L
Swarm	15:53:21.03	-20.796481	-68.947220	9.614	3.0
Subcluster A	10:23:47.69	-21.233550	-69.173173	36.897	4.1

swarm occurred 2006.04.01; subcluster A occurred 2006.10.11

Before the moment tensor inversion, the short-period (velocity) records are integrated once, in the frequency band of 0.65 – 2.1 Hz with cosine tapering applied to both ends. Complete three-component waveform are employed without separation of specific groups (e.g., P , S); these were resampled at

all stations into 8192 points, with a timestep of 0.04 s and a time length of 245.76 s.

The wave inversion uses a crustal 1D model derived from *Lüth* [2000] (see Table 4.6, Figure 4.22). The deviatoric point source inversion is selected for a series of trial source positions lying at various depths below the epicenter position determined previously (Table 4.5).

Table 4.6: 1D velocity model used for inversion

Depth km	V_p [km/s]	V_s [km/s]	density [g/cm ₃]
0.0	4.00	2.299	2.500
1.0	6.05	3.477	2.910
9.0	6.28	3.609	2.956
22.0	6.39	3.672	2.978
32.0	6.51	3.741	3.002
67.0	7.60	4.368	3.220
83.0	7.60	4.368	3.220
90.0	8.10	4.655	3.320

V_P/V_S ratio 1.78

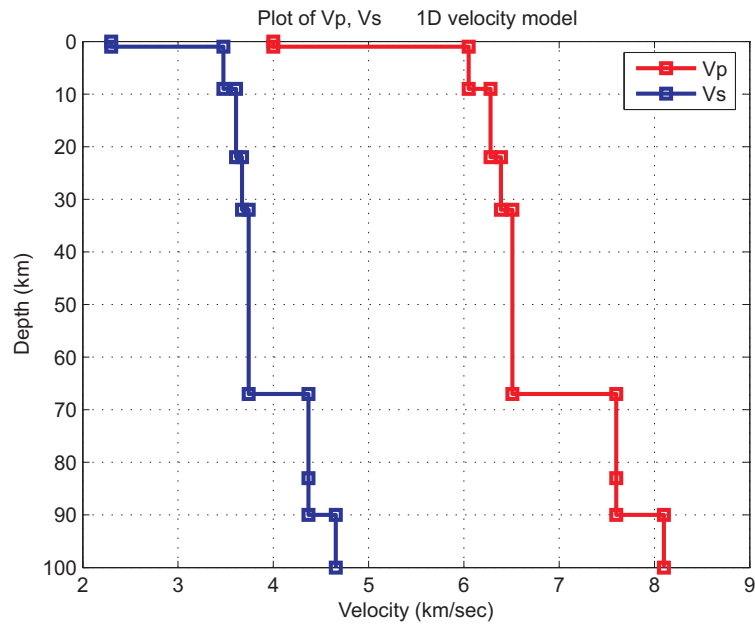


Figure 4.22: The velocity model used for inversion.

Through a grid search over set of trial source positions and time shifts is sought the trial source position and time for which the residual error of the least squared method is minimized.

The search grid for the swarm inversion is shown in the Figure 4.23, the total trial sources tested were 9, with a 2 km vertical separation, spanning depth from 5 to 21 km. The highest correlation values are found in a well-determined position in the grid (source 5 [13 km], time shift 1.2 s and correlation of 70.44%), having the other values a very low correlations.

Despite this well-constrained location in the grid, there is a misfit in the depths (13 km in the moment tensor inversion) with respect to the values calculated with the NonLinLoc method (9.614 km). This misfit can be explained due to the NonLinLoc method used a 2D velocity model, whereas the moment tensor inversion used a 1D version of this 2D velocity model.

In the Figure 4.24 also shows the dependence between correlation and depth, inclusive it is possible to see that the solutions of the moment tensor differ greatly with the depth (e.g., solutions at 11 km and 15 km).

In summary the results of the moment inversion for the swarm are well-represented by the single solution located at 13 km depth.

The last point can be corroborated by examining the good fitting between the observed and synthetic seismograms in displacement, which were compared in the frequency band of 0.65 – 2.1 Hz (Figures 4.27, 4.28 and 4.29).

The stations used in this inversion were T06, T04, T18, T08, T17, T07, T10, T15, T05, T20, and T19. The best fits, considering the three components, occurred at stations T06, T04, T08, T17, T10, and T19. The other stations misfit in one or two components.

On the other hand, the search grid for the subcluster A inversion is shown in the Figure 4.25, the total trial sources tested were 18, with a 2 km vertical separation, spanning depth from 5 to 39 km. The highest correlation values are found, as in the swarm, in a well-determined position in the grid (source 12 [27 km], time shift 3.6 s and correlation of 71.28%), having the other values a very low correlations.

A similar misfit in depth occurred in the results of the subcluster A inversion (27 km) compared with 36.897 km using the NonLinLoc method. Also it is speculated that the different velocity models used influence greatly the locations of the source in depth.

The Figure 4.26 also shows that the solutions of the moment tensor differ greatly with the depth (e.g., solutions at 25 km, 29 km, and 31 km). As in the case of the swarm, the results for the subcluster A are represented by the single solution located at 27 km depth.

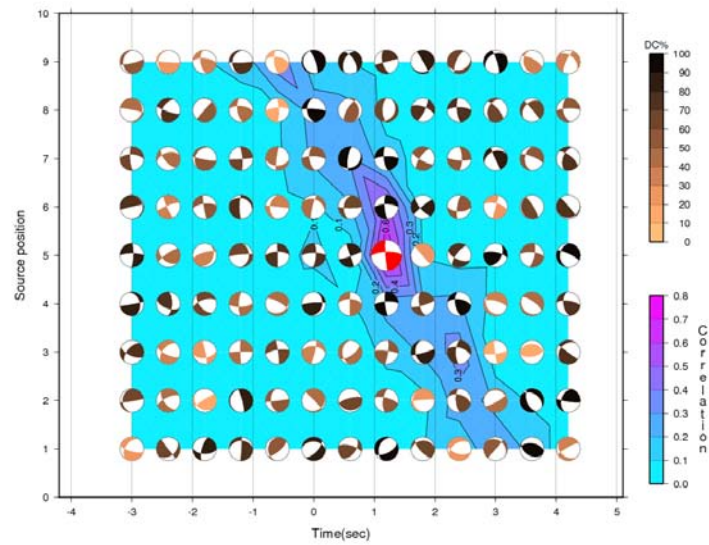


Figure 4.23: The correlation values for the swarm moment tensor inversion are shown as a 2D function of the trial source position and time. The highest correlation values are found at source 5 (13 km) and time shift of 1.2 s. The focal mechanisms (FM) indicate the solutions for the inversion for each point on the grid (colors represent the double-couple percentage, DC%). The red FM indicates the best solution.

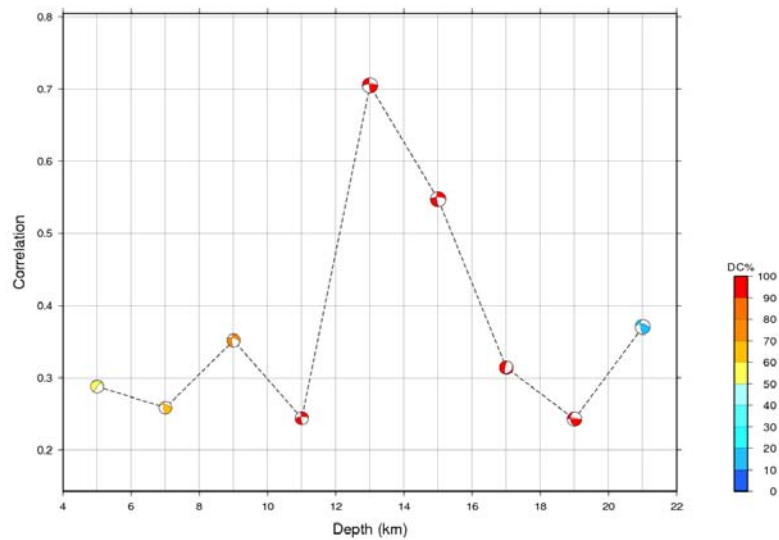


Figure 4.24: The correlation between observed and synthetic waveforms and focal mechanism as a function of the trial source depth below the epicenter calculated by NonLinLoc method (Swarm). Colors represent the DC%. It is important to remark that the solutions for the moment tensor differ greatly with the depth.

The Figures 4.30 and 4.31 show the good fitting between the observed and synthetic seismograms in displacement, which were compared in the frequency band of 0.65 – 2.1 Hz. The stations used in this inversion were T05, T20, T08, T04, and T19. The best fits occurred at stations T05, T20, and T19.

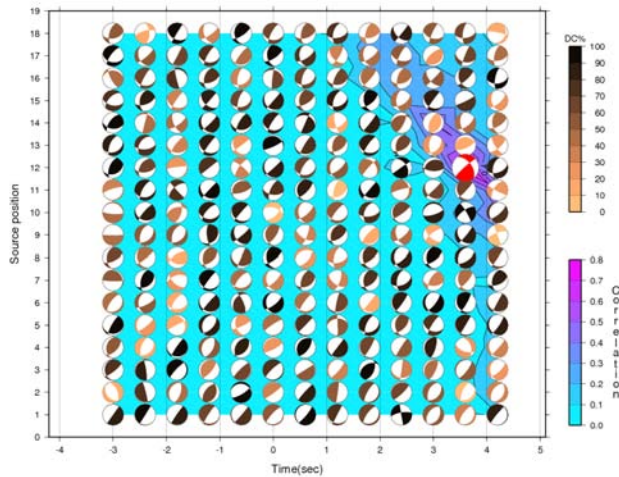


Figure 4.25: The correlation values for the swarm moment tensor inversion are shown as a 2D function of the trial source position and time. The highest correlation values are found at source 12 (27 km) and time shift of 3.6 s. The focal mechanisms (FM) indicate the solutions for the inversion for each point on the grid (colors represent the double-couple percentage, DC%). The red FM indicates the best solution.

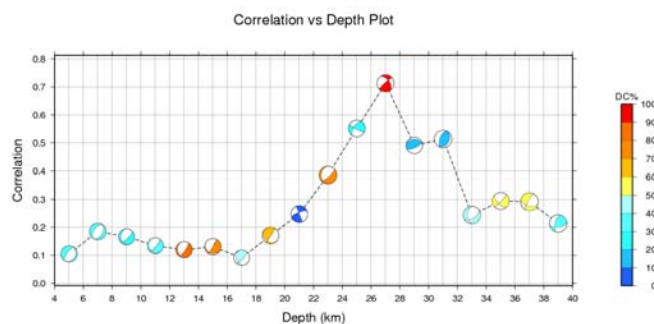


Figure 4.26: The correlation between observed and synthetic waveforms and focal mechanism as a function of the trial source depth below the epicenter calculated by NonLinLoc method (Subcluster A). Colors represent the DC%. It is important to remark that the solutions for the moment tensor differ greatly with the depth.

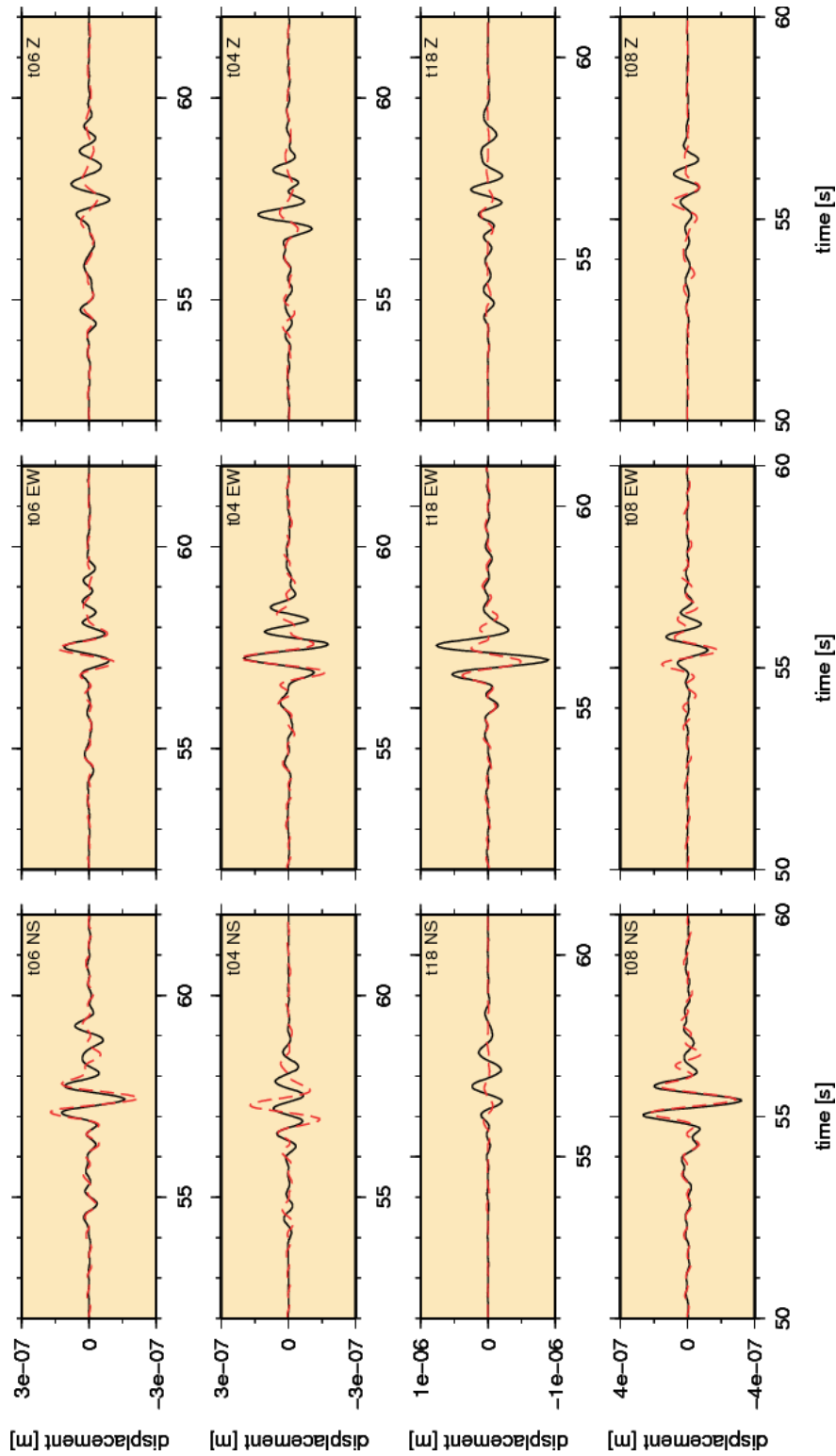


Figure 4.27: Comparison between the observed (black) and synthetic (red) seismograms for the stations T06, T04, T18 and T08 in the case of swarm. The best fits, considering the 3-components, occurred at stations T06, T04 and T08. The station T18 has a misfit in the *S*-wave in the vertical component.

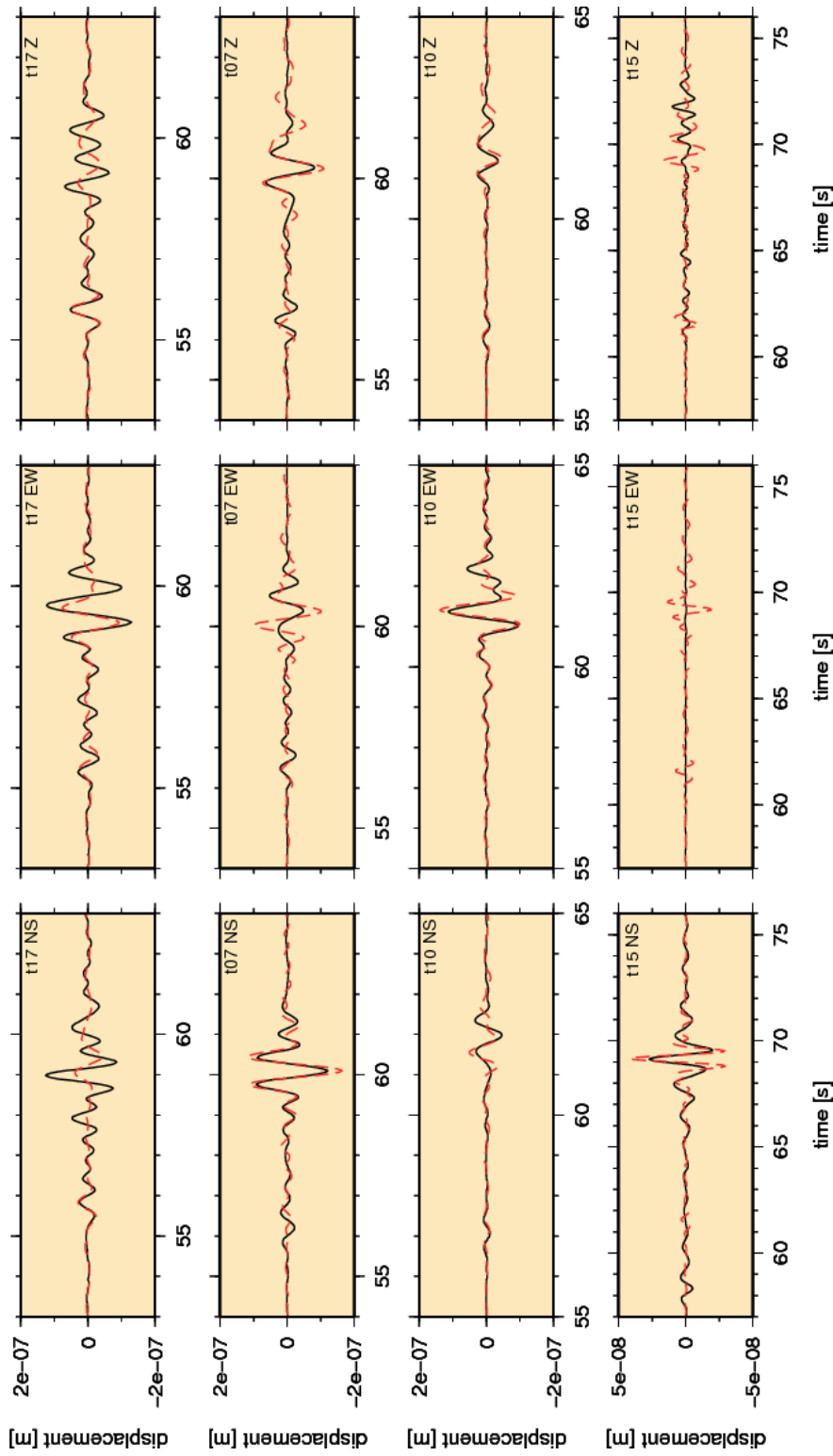


Figure 4.28: Comparison between the observed (black) and synthetic (red) seismograms for the stations T17, T07, T10 and T15 in the case of swarm. The best fits, considering the 3-components, occurred at stations T17 and T10. The station T07 has a misfit in the S-wave in the E-W component, The station T15 only has a good fit in the N-S component.

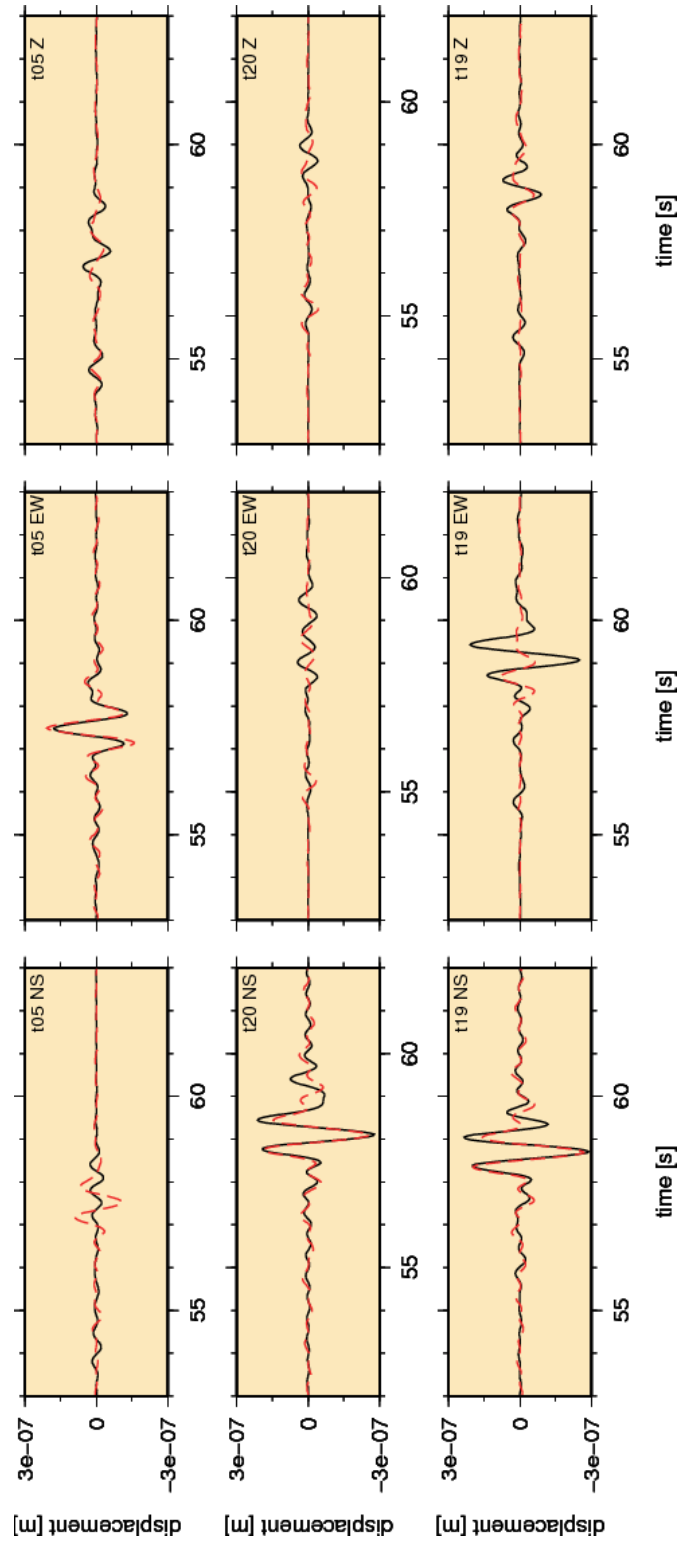


Figure 4.29: Comparison between the observed (black) and synthetic (red) seismograms for the stations T05, T20 and T19 in the case of swarm. The best fits, considering the 3-components, occurred at station T19. The station T05 has a misfit in the S-wave in the N-S component. The station T20 only has a good fit in the N-S component.

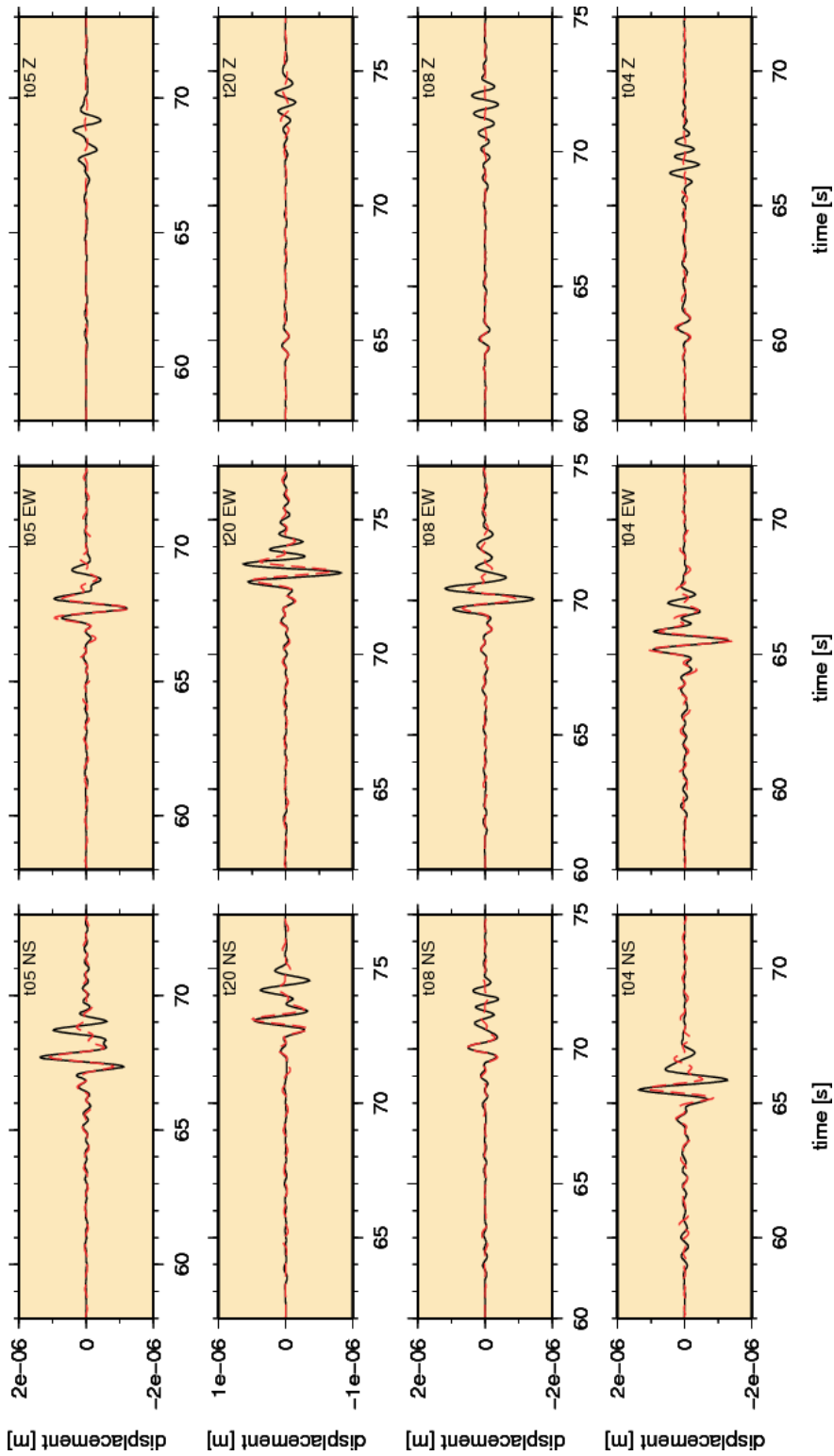


Figure 4.30: Comparison between the observed (black) and synthetic (red) seismograms for the stations T05, T20, T08 and T04 in the case of subcluster A. In general the stations have a good fit in all their components. The misfit are associated to the S-wave in the vertical components.

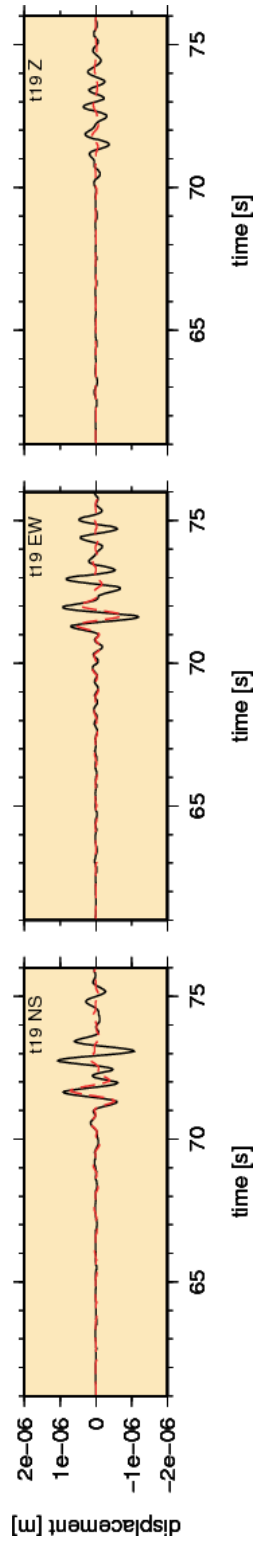


Figure 4.31: Comparison between the observed (black) and synthetic (red) seismograms for the station T19 in the case of subcluster A. Only the early arrive of the S-wave field are well-represented.

The results revealed that the double-couple (DC) percentage is 91.8% –in the case of the swarm– and 91.9% for the subcluster A, whereas the compensated linear vector dipole (CLVD) percentage is 8.2% and 8.1% for the swarm and subcluster A, respectively.

The high values of the DC for both, swarm and subcluster A, indicate that a possible sources for the cluster activity can be related to tectonic causes (associated a shear in a fault surface). However, there are a low percentage associated to CLVD component, which could be representing misfit in the velocity model or, more interesting, it could be related to tensile forces such as the presence of fluids in the sources. This last point will be investigated in the next chapter.

The moment magnitudes obtained in each case ($M_W = 2.3$ for the swarm and $M_W = 3.0$ for the subcluster A), are slightly smaller than local magnitudes calculated by spectral analysis for these events.

The results also show –in the case of the swarm– a strike-slip solution for the best double couple, being its nodal planes of 176/85/161 and 268/71/6, respectively (the numbers indicate: strike/dip/rake) see Figure 4.32a and Table 4.7. For the subcluster A, the result shows an oblique faults as the best double couple with nodal planes of 323/52/8 and 228/83/142, respectively (Figure 4.32b and Table 4.7). As we will see later, the real rupture planes are 268/71/6 for the swarm and 323/52/8 for the subcluster A.

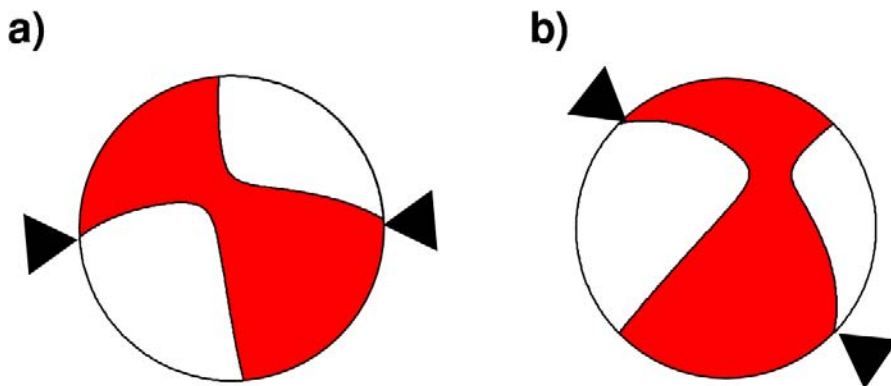


Figure 4.32: Moment tensor solutions, (a) swarm and (b) subcluster A. The black arrows indicate the real plane of rupture propagation. For further information, see spatial analysis section 5.5.

Table 4.7: Moment tensor solutions

Event	Time [s]	Moment [Nm]	Strike [deg]	Dip [deg]	Rake [deg]	DC [%]	Variance reduction
Swarm	1.2	$3.085 \cdot 10^{12}$	268	71	6	91.8	0.5
Subclus. A	3.6	$3.775 \cdot 10^{13}$	323	52	8	91.9	0.51

strike, dip and rake for real rupture planes

As a test of the quality of the solutions, the moment tensor results were superimposed to the polarities of the P -wave first arrival, for all stations that recorded the swarm and subcluster A events. The existence of a high correspondence between the moment tensor solutions and the P -wave polarities indicates that the solutions are robust (Figures 4.33a and 4.33b).

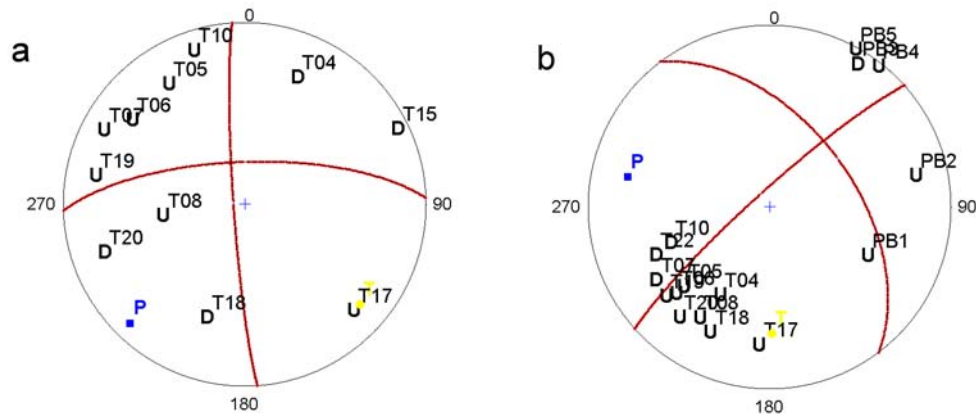


Figure 4.33: The polarities of the P -wave first arrival are superimposed on the moment tensor solutions in order to test the quality of the moment tensor solution, (a) swarm and (b) subcluster A. Only the station T08 in the case of swarm, and PB03 and PB02 for the subcluster A have a different polarity, therefore the solutions are robust. See Figure 2.3 for location of PBO stations.

4.6 Discussion of the results and comparison with other studies

At the latitude of our study ($\sim 21^\circ\text{S}$) seismic reflection studies and geophysical experiments show the presence of a $< 30\text{-km}$ -deep west dipping reflector below the Precordillera (Quebrada Blanca Bright Spot, QBBS) associated with a low-velocity zone (Figure 4.40), P to S wave conversions, and corresponding to the upper boundary of a high conductivity and high Poisson's ratios domain [ANCORP Working Group, 2003].

ANCORP Working Group [2003] favored the idea that QBBS is a petro-physical feature related to the presence of fluids or melts, or mafic intrusions into a felsic country rock. Victor *et al.* [2004] suggest that the western termination of this reflector corresponds to the downdip end of the west vergent thrust outcropping in Altos the Pica area. The discontinuity continues farther to the east, below the Altiplano and Eastern Cordillera between 15 and 30 km depth, where it is called the Altiplano low-velocity zone (here, LVZ) [Wigger *et al.*, 1994; Yuan *et al.*, 2000]. The LVZ would be related to the brittle-ductile midcrustal transition decoupling mechanically an upper rigid crust from a lower ductile crust [Yuan *et al.*, 2000; ANCORP Working Group, 2003].

On the basis of the distribution of crustal microseismicity in the study area, the existence of a west-dipping boundary (Figure 4.6b and 4.13c) is proposed, which can be related to the changes in the crustal rheology; that is, this plane may represent the brittle-ductile boundary in the crust mentioned above. Also the well-fitting geometry between the LVZ and the eastward prolongation of this west-dipping structure supports this idea.

David *et al.* [2002]; David [2007] and Farías *et al.* [2005] see a similar boundary for the northernmost part of the Chilean forearc (Figure 4.34 and 4.35). They relate this plane to the uplift of the western Altiplano, link rising magma to the recent magmatic arc, and ductile flow in the crust from the east.

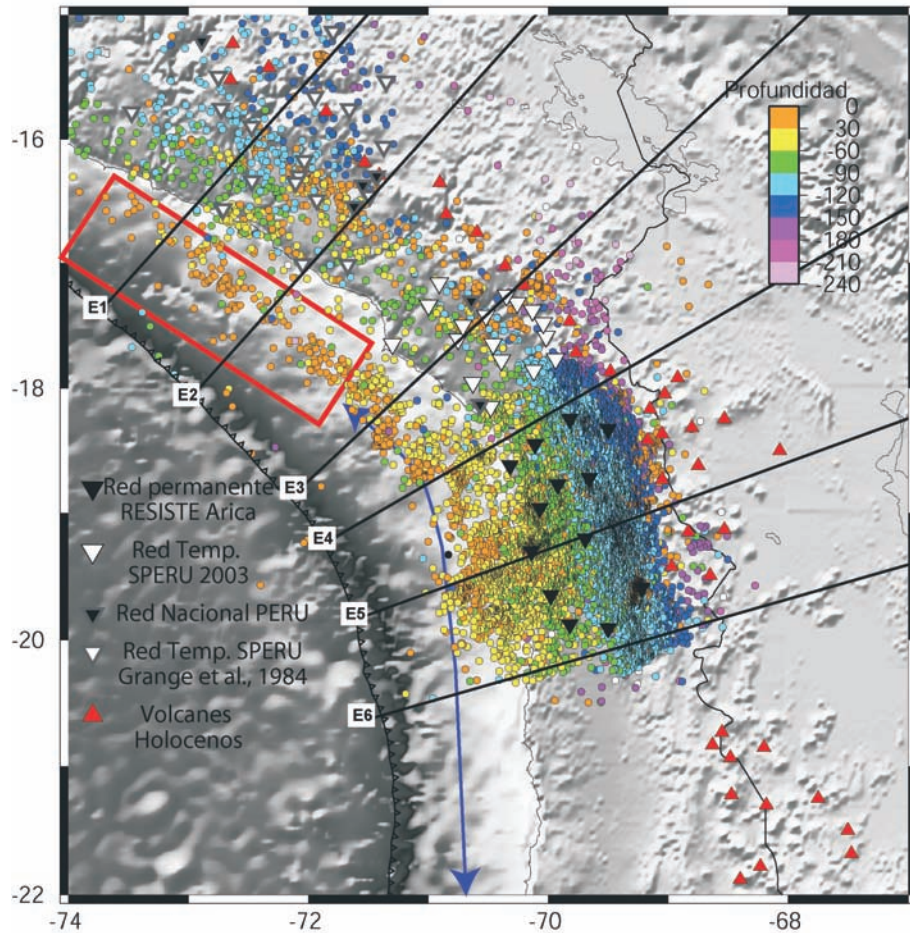


Figure 4.34: Local seismicity map $M_L \leq 4.0$, registered by the local temporal networks in 1981 and 2003 and by permanent networks during the period 1981-2004 and 1996-2006 [taken from *David*, 2007]. The red rectangle indicates the rupture area of the Arequipa earthquake. The black lines show the orientation orthogonal to the trench of the seismicity profiles. The inverted triangles indicate the different networks installed in the zone and the red triangles indicate the Holocene volcanoes.

The similar seismicity pattern is found in the south of Peru [*David*, 2007] and the Antofagasta latitude [*Belmonte-Pool*, 2002] (Figures 4.34, 4.35 and 4.36). Thus, this seismic feature is traced along the major part of the forearc of the Altiplano segment, confirming that it is an important lithospheric characteristic, which represents a rheological boundary in the crust.

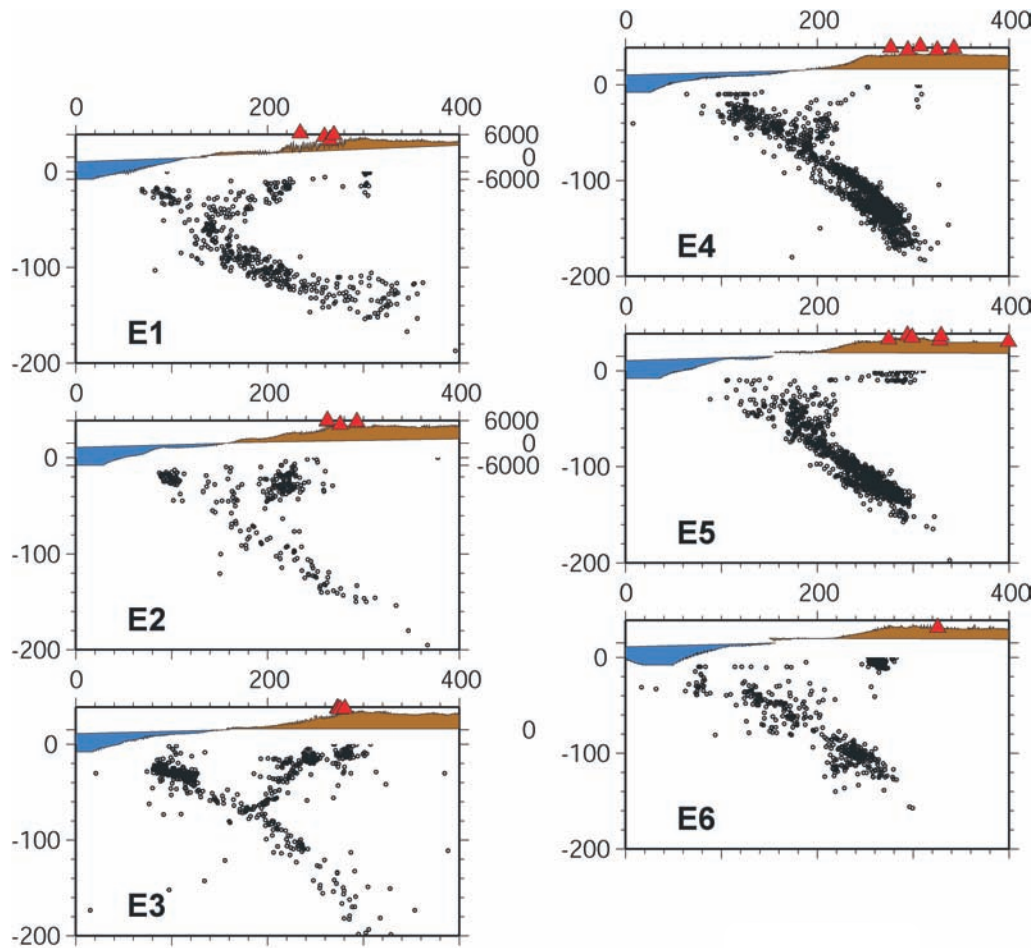


Figure 4.35: Seismicity profiles registered by the different networks that have been installed in the zone [taken from *David, 2007*], for positions of this profiles see Figure 4.34. Red triangles indicate Holocene volcanoes.

In his geometrical model, *Tassara [2005]* shows this seismicity plane [*David et al., 2002; Farías et al., 2005*] as a boundary that defines a crustal-scale triangular zone, a slab-forearc system, which, in a log term, can be interpreted as a rigid, indenter-like backstop that has resisted the westward movement of crustal material coming from the shortened eastern foreland.

Thus, the west-dipping structure found in this study could be seen as southward prolongation of the structure described by *David et al. [2002]; David [2007]* and *Farías et al. [2005]* (modeled by *Tassara [2005]*), and also described by *Belmonte-Pool [2002]* in the south of the Altiplano segment.

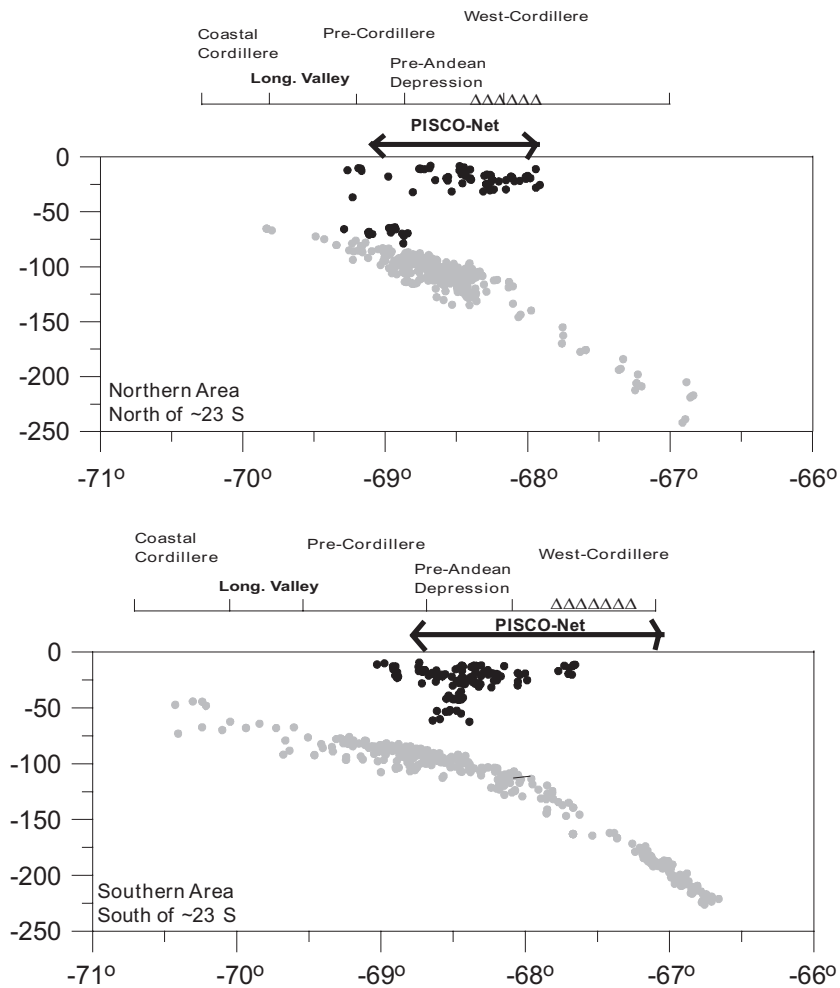


Figure 4.36: Distribution of local seismicity north and south from 23°S [taken from *Belmonte-Pool*, 2002].

Sobolev et al. [2006] in his finite strain model for the Central Andes shows the crustal structure of the overriding plate and the shear coupling at the plate interface (Figure 4.37). Thus it is possible to see clearly signatures of mega-thrust, thin-skinned deformation in the foreland, lower crustal flow, underthrusting of the shield margin and delamination of mantle lithosphere.

The most interesting point is in the forearc, where the model predicts a zone with intermediate-high deformation dipping to the west. This zone could define a possible crustal structure directly related to the west dipping structure discussed in this work.

The last point confirms that numerical models are capable of reproducing a deformation zone as result of the subduction that explain the seismicity recorded in the study area.

A new question can be putted to discussion: Is this zone related to brittle or ductile deformation?

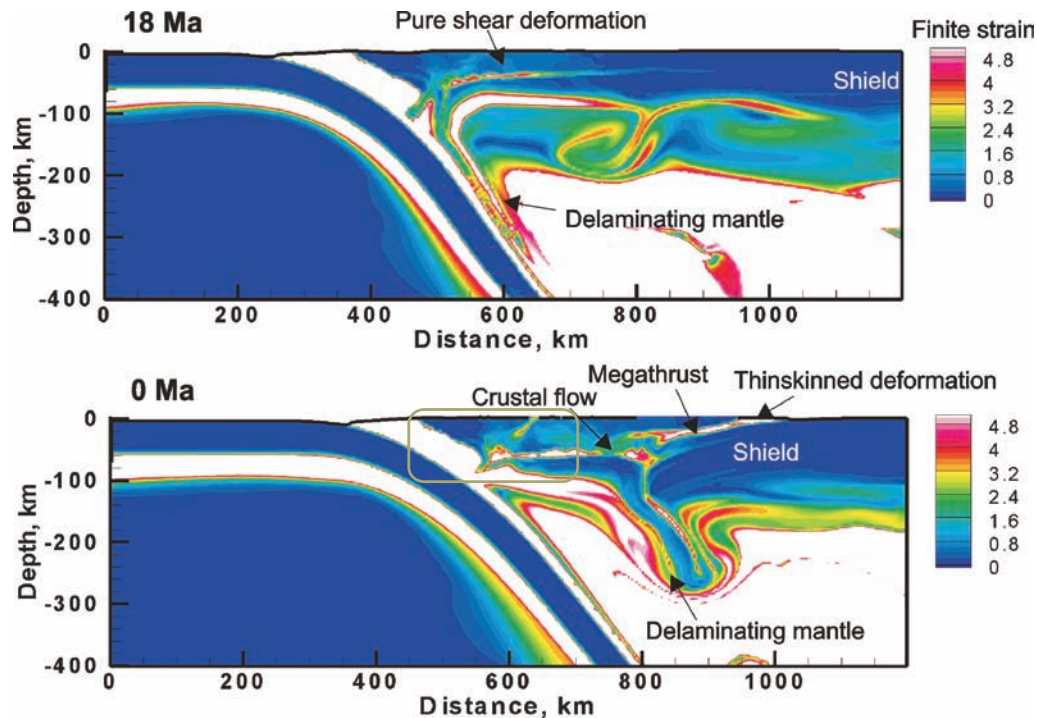


Figure 4.37: Calculated finite strain in the Central Andes' model and 18 Ma and 0 Ma [taken from *Sobolev et al.*, 2006]. Note the clear signatures of mega-thrust, thin-skinned deformation in the foreland, lower crustal flow, underthrusting of the shield margin and delamination of mantle lithosphere. Also it is possible to note a clear structure in the forearc between 200-300 km from the trench (see the light green box in the bottom section), which could represent the west dipping structure discussed in this study.

On the other hand, the deeper focal mechanisms give information on possible displacements on the seismicity plane, and might confirm the presence of a reverse structure in the lower crust, which acts as a boundary in the seismicity and could also make possible relative displacements between the lower and upper crust, facilitating the deep flow of the lower crust [*Sobolev et al.*, 2006] (Figure 4.37).

Focal mechanisms were also calculated by *David* [2007] in the northern part of the Chilean forearc, analyzing the result obtained by her in relation with the west dipping structure, it is possible correlated –in some focal mechanisms– a thrust behaviour.

Also it is possible to see a similar behaviour in focal mechanisms associated to different seismicity profiles registered in the south of Peru [Perez in David, 2007]. In the case of the results obtained by Belmonte-Pool [2002], the thrust tendency in the focal mechanisms is more difficult to see, however it is possible to find with a careful analysis of his results.

In relation to the kinematic characterization of the WFFS in the period Pliocene-Recent, in the Altos de Pica region, Victor *et al.* [2004] found evidence of N-S strike-slip motion and pull-apart basin formation with NW-SE extension bordering the Salar de Huasco, which began in the late Pliocene. This is in agreement with the results obtained in the inversion of the stress tensor for the subarea NE, which shows strike-slip motion with NW-SE extension (see (4) in the Figure 4.38). The focal mechanisms of the Aroma and Chusmiza earthquakes correlate with the strike-slip deformation observed in the Altos de Pica region [Farías *et al.*, 2005], the focal mechanism for the swarm event also correlates with the strike-slip behaviour for the Altos de Pica region (see (3) in the Figure 4.38).

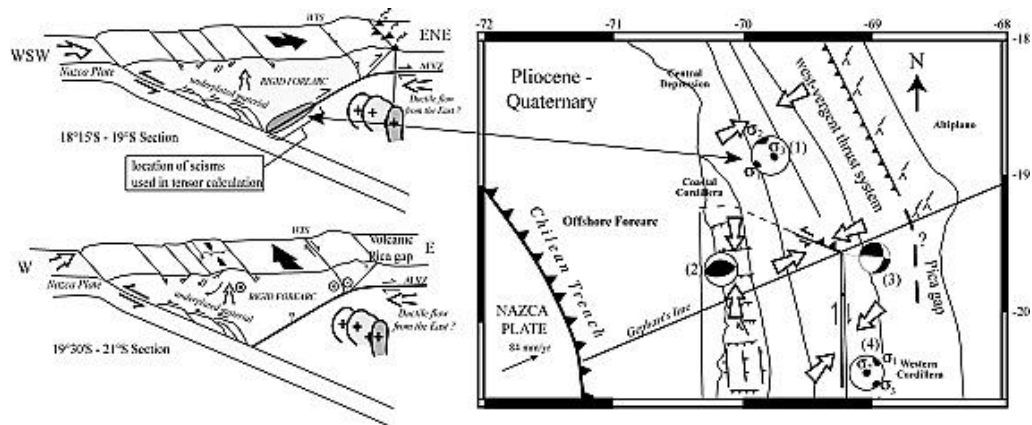


Figure 4.38: Present-day tectonic regime of the western flank of the Altiplano in northern Chile [taken from Farías *et al.*, 2005]. The stress tensor calculated north of 19°S (1) was determined by David *et al.* [2002] based on the crustal seismicity located between 30 and 60 km depth. On the basis of the kinematic analysis of E-W thrusts located in the Coastal Cordillera, Allmendinger in Farías *et al.* [2005] determined N-S shortening (2). In the eastern side of the Cordillera in Altos de Pica region, Victor *et al.* [2004] found evidence of N-S dextralmotion and pull-apart development with an NW-SE extension (4). Focal mechanisms determined by the Harvard CMT for the Aroma and Chusmiza earthquakes (3) show an equivalent strain regime as the Altos de Pica region.

The stress tensor obtained for the volcanic arc in the Arica bend region [David *et al.*, 2002], indicates an extensional regime, which is in agreement

with the results obtained in the inversion of the stress tensor for the subareas Swarm and SE. The regional stress tensor for the study area also have a good correlation with the *David et al.* [2002] result (Figure 4.39).

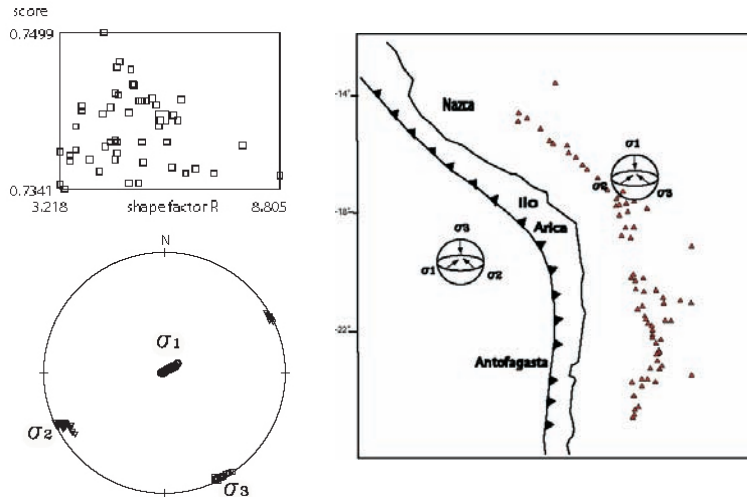


Figure 4.39: Stress tensor obtained by the inversion of the focal mechanisms in the volcanic arc of the Arica bend [taken from *David et al.*, 2002]. The result indicates a tensional regime for this area, which has a good correlation with the stress tensor inversion for the zones Swarm, SE, and Regional (Figures 4.15, 4.18, and 4.19).

In contrast, north of Arica, *David et al.* [2002] revealed that the deep forearc of the Arica region (18° - 19° S) undergoes ENE-WSW shortening associated with the activity of east vergent thrust (see (1) in the Figure 4.38).

However, the P -axis mechanism of the Arica earthquake [*Legrand et al.*, 2007], the Pliocene-Recent σ_1 direction estimated in Altos de Pica [*Victor et al.*, 2004], and the maximum stress axis calculated by *David et al.* [2002] in the Arica region have a common pattern, all of them are almost parallel to the present-day plate convergence direction. The similar pattern is found in the results of the stress tensor analysis for the subareas NW, SW and NE. In the areas where the regime is extensional (Swarm and SE), the σ_2 instead σ_1 is almost parallel to the plate convergence direction.

The apparent contradiction in the kinematic behaviour of the WFFS is not real because the compressive active tectonic regime observed in the north by *David et al.* [2002] continues southward in the areas less than about 2 km high over sea level –supporting the observations associated with the west-dipping structure mentioned above, whereas the strike-slip regime observed by *Victor et al.* [2004] is found in the high place of the Precordillera.

The most important effect of such a large-scale mass distribution is the perturbation of the vertical lithospheric stress σ_V . The average excess of this stress with respect to the reference lithostatic stress at the sea level, amounts to the weight of the topography [Tibaldi *et al.*, 2008].

In the studied area, the σ_V value became higher than the minimum horizontal stress σH_{min} assuming, first, the value of σ_2 (NE zone). Then, σ_V increased further and became higher than the maximum horizontal stress σH_{max} assuming the value of σ_1 (Swarm and SE zones). Previous studies [e.g., Meijer *et al.*, 1997; Tibaldi *et al.*, 2008] showed that a relative slight increase of average altitude of mountain belt is enough to produce a general change of dominant fault style.

Thus, the analysis of the stress tensor presented in this study reveals –at first view– that a relationship exists between topography and tectonic regime because most of the reverse faulting occurs where the topography is less than about 2 km high, whereas normal faulting is observed at elevations higher than 3 km [Meijer *et al.*, 1997; Victor *et al.*, 2004; Tibaldi *et al.*, 2008]. Such a correlation could explain the changes in the stress field in each zone.

Therefore, the state of stress of the convergence margin of northern Chile has always been related to compression, and according to the explanation above, the extension is restricted to the highest areas as a result of local stress due to forces associated with the thickened crust.

In summary, the tectonic model proposed in this study is based on the spacial distribution of the seismicity, which shows a sharp lower boundary (Figure 4.40). This lower boundary in seismicity can be correlated with reflectivity zones in the crust [Yoon *et al.*, 2003].

In the upper crust, eastward of the WFFS, this boundary correlates with the low velocity zone [Wigger *et al.*, 1994], whereas in deep, it has a close relation to the 350°C temperature isoline [Springer, 1999], these facts permit us to speculate that this boundary corresponds to a shear zone between the brittle and ductile crust.

The analysis of the deeper focal mechanisms associated to this lower boundary indicates a kinematic compatible with a reverse fault. The transpressional regime associated to the west side of the WFFS support this interpretation and it is also compatible with the shallow thrust structures found there [Victor *et al.*, 2004]. The transtensional and strike-slip regimes found in the highest areas of the Precordillera are compatible with neotectonic studies carried out in the zone [Victor *et al.*, 2004].

The seismic clusters are closely related to the structures described above, the moment tensor analysis shows that the origin of the sources is related to shearing in a fault zone. However the influence of fluid in the sources is not completely discarded.

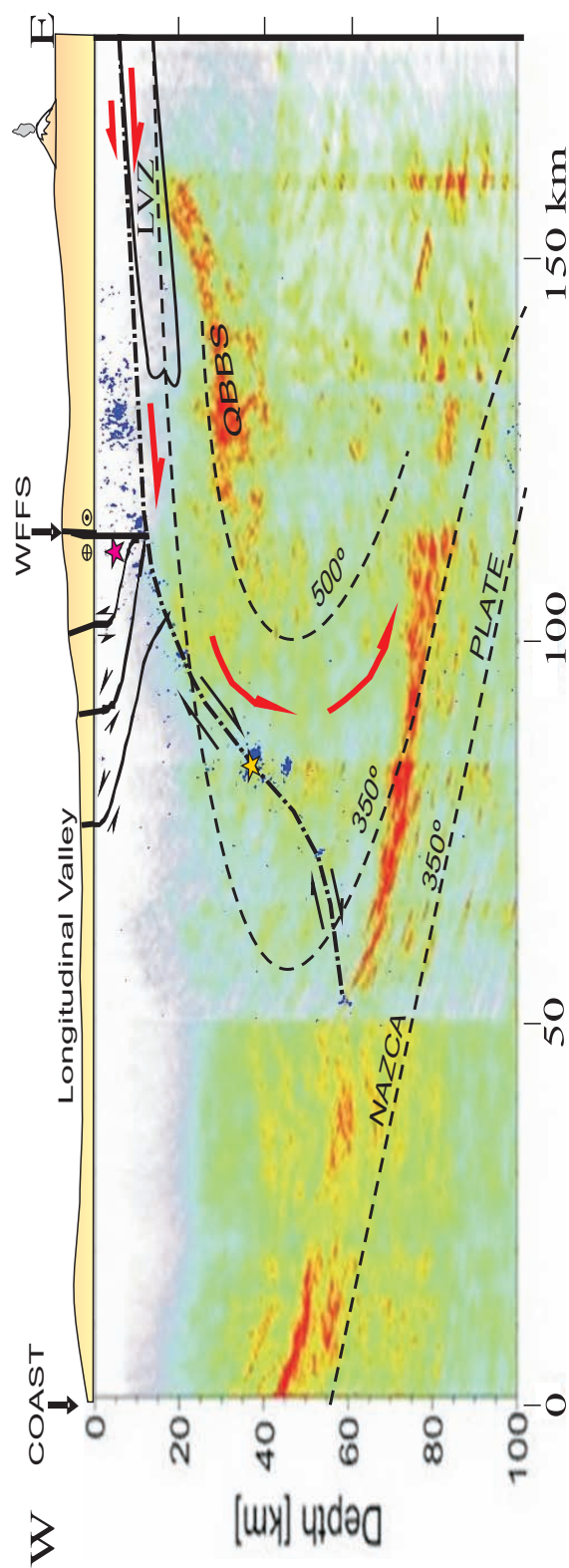


Figure 4.40: The observed seismicity (blue circles) is plotted to the Kirchhoff prestack depth migration of the western part of the ANCORP reflection seismic data set [Yoon *et al.*, 2003]. The lower limit of the seismicity is near to the 350°C temperature isoline (after Springer [1999]) and a low velocity zone (LVZ) (after Wigger *et al.* [1994]). The dashed black line dipping to the west correlates with reflectivity and the lower limit of seismicity. This seems a possible shear zone between the brittle and ductile crust ($\sim 350^\circ\text{C}$) supporting the uplift of the western flank of the Altiplano. Focal mechanisms of the lowest events (see Fig. 4.13c) support the interpretation as a shear zone. A similar structure was presented for the northernmost part of Chile by Fariás *et al.* [2005]. The thrust faults west to the WFFS (drawn after Víctor *et al.* [2004]) are compatible with the transpressional regime in this zone. The magenta and yellow stars indicate the swarm and the SW cluster, respectively. The high reflectivity zones (red) indicate the subducted Nazca plate (dipping eastward) and the Quebrada Blanca Bright Spot (QBBS; dipping to the west and below to the 500°C isothermal line). The slab-related seismicity is partially shown. The red arrows depict the flow of material from the east (after Tassara [2005]).

Chapter 5

Detecting possible fluid signals from the clusters

5.1 Introduction to the cluster analysis

An important earthquake clusterization was found in different levels of the upper crust, spatially related to the reverse structure mentioned in the chapter 4, even one of the clusters has characteristics of an earthquake swarm. The origin of crustal earthquake clusterization is often assumed to be caused by crustal structure complexities and/or fluid migration [*Shapiro et al.*, 1997; *Parotidis et al.*, 2003; *Hainzl*, 2003].

The crustal seismo-tectonic activity is investigated in order to specify the origin of the sources of the clusters. Thus, for characterizing the signals caused by the sources, high quality seismicity data from West Fissure Fault System (WFFS) are analyzed, these data were recorded during the years 2005-2009. Studying these processes, especially with regard to the importance of fluid migration and stress transfer, provides insight into the role that these phenomena have in the triggering of seismic activity in the upper crust.

5.2 Data

The events studied correspond to two seismic clusters. The SW cluster, which was divided in two subclusters (A and A') at 35 and 40 km depth, respectively. The subcluster (A) consists of 224 events occurring between 6 January 2006 and 4 July 2009 (see chapter 3). However, only 182 events are studied, which occurred until 31 August 2008 –due to their more accurate locations (Figure 5.1a). The subcluster (A') consists of 38 events occurring

between 19 October 2006 and 13 March 2008 (see chapter 4 and Figure 5.1b).

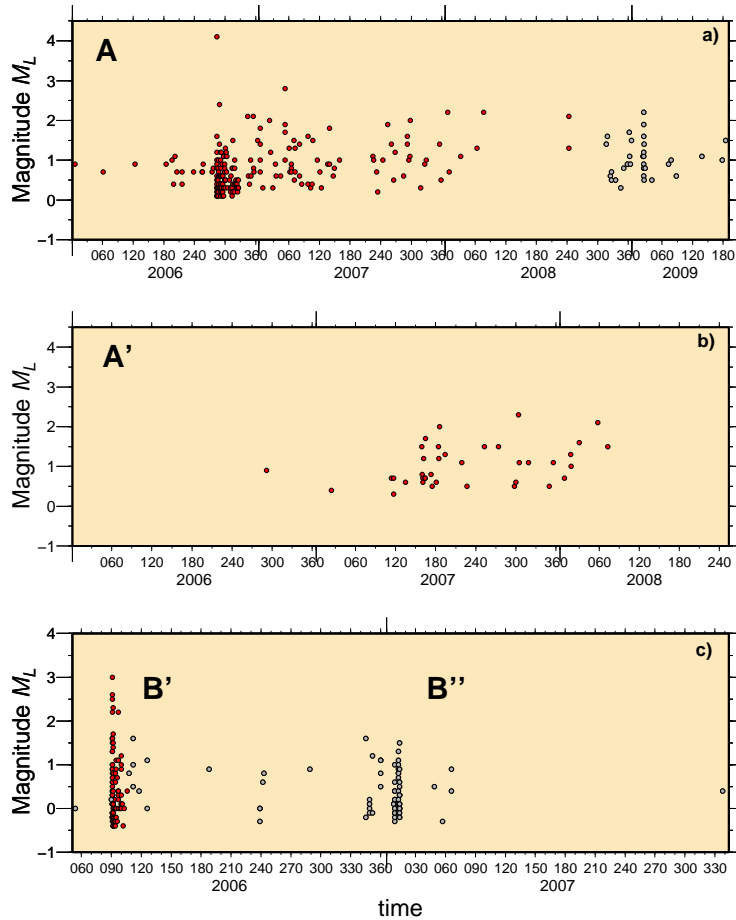


Figure 5.1: The magnitudes of the clusters is shown as a function of time. Subfigures (a) and (b) show the distribution in the subclusters A and A' respectively. Subfigure (c) shows the distribution in the swarm B, the capital letters B' and B'' indicate that the swarm can be divided in two phases. The red circles indicate the events that were used in the calculations, whereas gray circles indicate the events that were not used due to their less accurate locations.

The other cluster (B) is located in the central part at ~ 9 km depth with 185 events occurring between 23 February 2006 and 4 December 2007 (see chapter 4). It can be separated into two phases, B' and B'' respectively (Figure 5.1c). This cluster exhibits characteristics of an earthquake swarm [Wigger *et al.*, 2007], since it consists of a large number of earthquakes clustered strongly in space and time without being dominated by a single large earthquake. Only 90 events corresponding to the B' phase are studied due to their more accurate localization.

5.3 Chronological evolution of the energy release in the clusters

To understand the evolution of the energy release of the clusters in the time, an analysis of the magnitudes and energy release of the different events was carried out (see chapter 3 for further information of magnitude calculations).

Thus, in the central cluster both M_L and M_W magnitude distribution show that the sequence of earthquakes define a swarm, with no a clear mainshock associated to them (Figures 5.2a, 5.2b).

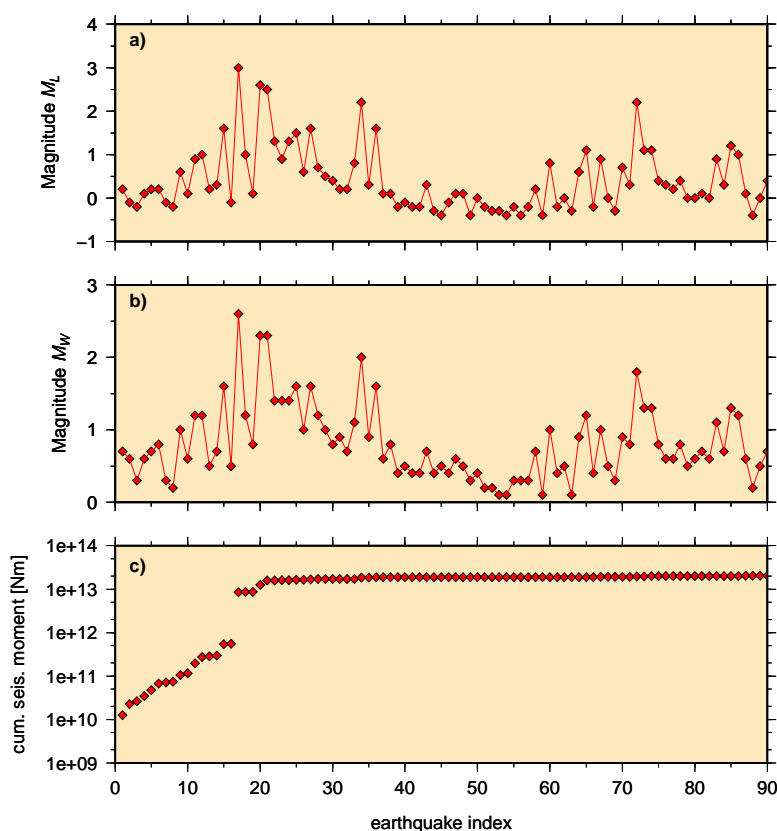


Figure 5.2: The energy evolution of the swarm as a function of earthquake index. (a) Local magnitude, (b) moment magnitude and (c) cumulative seismic moment release. It is clear to see that there is no a mainshock associated to the sequence. The jump in (c) correlates with the occurrence of the largest event in the swarm.

However, the cumulative seismic moment release indicates two different behaviors, before and after the seventeenth earthquake (the largest shock in the sequence). Thus, the behavior before of this event is characterized by a progressive and fast increase of seismic moment –which clearly shows

a trend– followed by the suddenly increase of one order of magnitude of seismic moment (which is caused by the occurrence of seventeenth event). Later on, a slow increase of the seismic moment is registered due to the fact that there are no more events with magnitudes higher than this seventeenth event (Figure 5.2c).

For the SW cluster the situation is rather different, in the sequence of earthquakes can be found both in M_L and M_W magnitude distribution a clear big event identified, which is also shown in the cumulative seismic moment release curve (Figure 5.3a, 5.3b).

The Figure 5.3c shows a similar behavior around of largest shock in the sequence as in the central cluster. However, the “jump” in the cumulative seismic moment releases reach two orders of magnitude evidencing the greater amount of energy released for this big event.

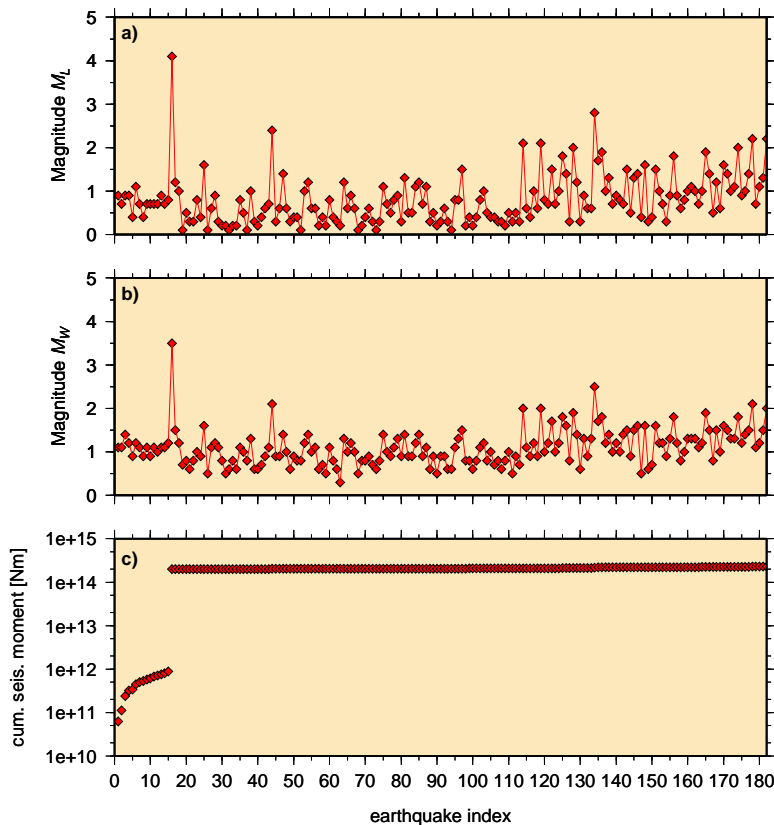


Figure 5.3: The energy evolution of the subcluster A as a function of earthquake index. (a) Local magnitude, (b) moment magnitude and (c) cumulative seismic moment release. It is clear to see that there is a mainshock associated to the sequence. The jump in (c) correlates with the occurrence of this mainshock.

5.4 Statistical characteristics

5.4.1 Frequency-magnitude distribution

The most common characterization of the earthquake populations is the cumulative frequency-magnitude distribution. In order to characterize the state of the stress in the clusters, an analysis of the b -values was carried out (see chapter 3 for further information).

The observed values of parameter b are 0.67 for the all phases of the swarm B (Figure 5.4a), 0.72 for the subcluster A, and 0.75 for the subcluster A' (Figures 5.4b and 5.4c).

In the cases of the subclusters A and A' the b -values are typical for the tectonic plate boundaries, namely $0.7 \leq b \leq 1.1$ [Karnik *et al.*, 1986; Mittag, 2000]. However –in the case of the swarm, the b -value is slightly low, which could be explained as a cycle of seismic moment accumulation.

5.4.2 Interevent-time distribution

The percentage of the mainshocks in the sequences that form the clusters can be approximated by the gamma distribution. Therefore, following to Hainzl *et al.* [2006], the interevent-time distribution will be used to estimate the percentage of mainshocks that forms the sequence of events in the swarm and subcluster A, respectively (see chapter 3 for further information).

Thus, the mainshock activity for the swarm reach to be 15% (Figure 5.5a), whereas in the subcluster A the percentage reach to 18% (Figure 5.5b). However, as it will be seen, the background seismicity percentages are very low to be responsible for the origin of all the rest of the seismicity associated with them –not all the seismicity corresponds to aftershocks related to this main shock activity. Thus, this higher percentage which is not explained by background seismicity should be related not only to aftershocks but also to the interaction of a non-stationary external forcing (e.g. fluids). The interaction of this external force would explain the long-term seismic activity found in the swarm and subcluster A.

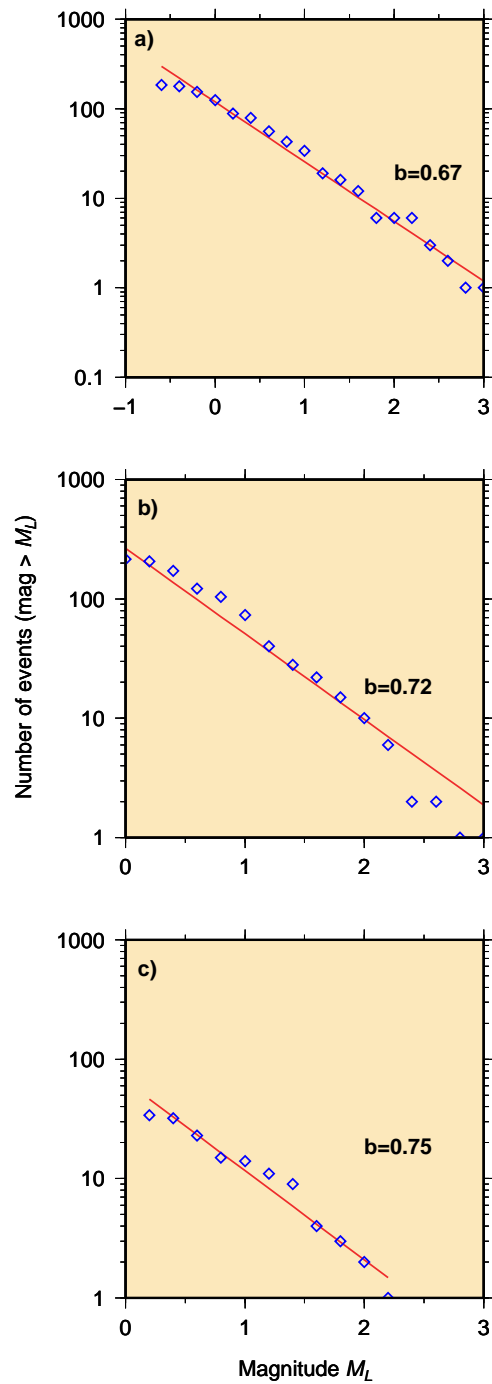


Figure 5.4: The cumulative frequency-magnitude distribution with their b -values for (a) two phases of swarm, (b) subcluster A, and (c) subcluster A'. The values are typical for tectonic plate boundaries, being the b -value for the swarm slightly low.

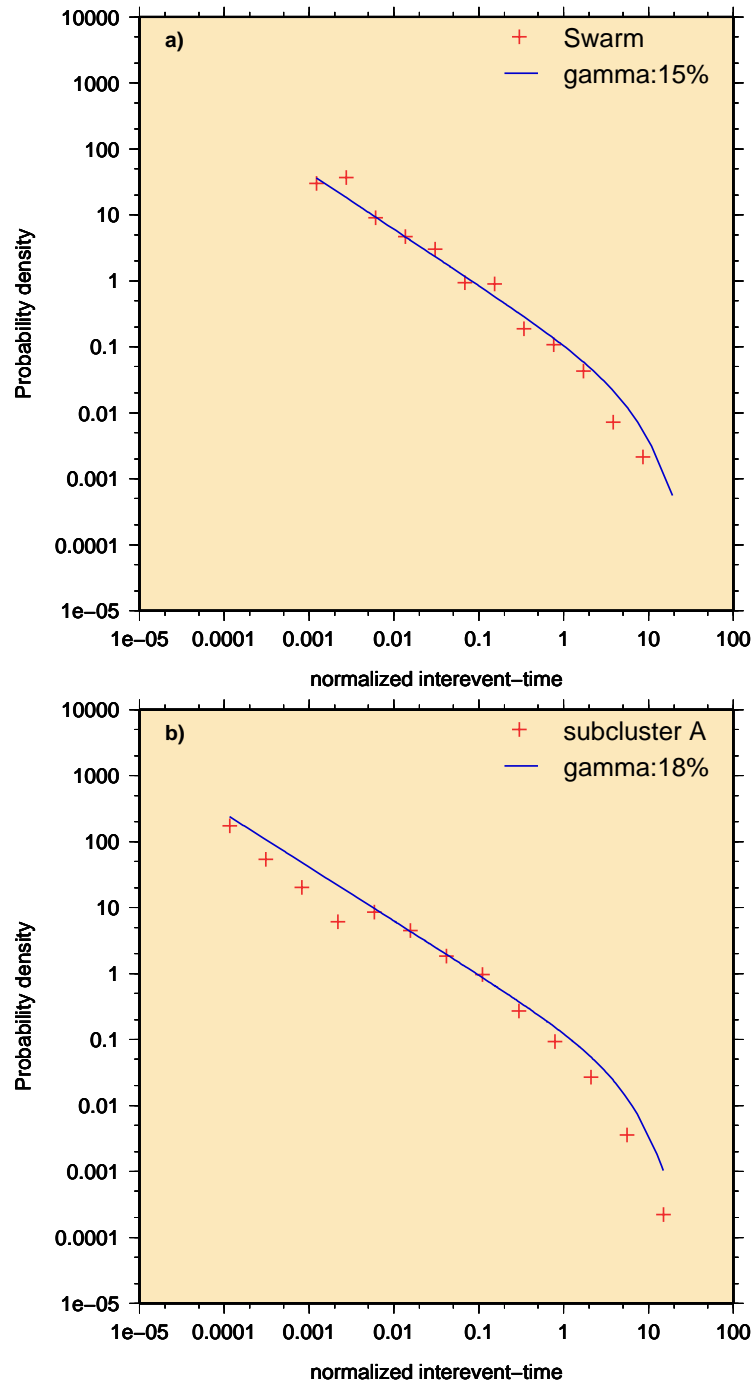


Figure 5.5: The interevent-time probability distribution for (a) swarm -where the distribution is compared with the fit of the gamma distribution that yield a mainshock fraction of 15%, and (b) subcluster A -with a gamma distribution that yield a mainshock fraction of 18%.

5.5 Spatial analysis

The hypocenters to the swarm and SW cluster (subcluster A and A') are found to be almost coplanar. I have fitted for both, swarm and SW cluster, a plane onto the 3-dimensional hypocenter cloud of the located earthquakes using PCA (Figure 5.6) (see chapter 3 for further information). The projections onto these planes are shown in the Figures 5.9 and 5.10. The origin of the coordinate system is moved to the hypocenter of the first earthquake of the swarm and subclusters, respectively.

The new coordinate system is rotated using the 3D Rotation Matrix method (see chapter 3 for further information), such that the x axis is horizontal and the z axis is perpendicular to the fitted fault plane.

Thus, in the case of the the plane that fits the events in the swarm, the x axis has a strike N90°W, the y axis dipping with 84°S and its activity preferably spreads to the west, and almost equally to above and bellow of the first earthquake. To the case of subcluster A, the plane has a x axis with a strike N25°W, the y axis dipping with 47°NE and, its activity is spreading to south-east in the horizontal and the north-east in the dipping direction. Whereas to the plane of subcluster A', the x axis has a strike N88°E, the y axis dipping with 41°SE and, its activity spreads to west-east in the horizontal and the south in the dipping direction.

The variation of the distances perpendicular to the plane (z -values) are much smaller than the variation within the plane, and the histogram of the z -values is well-defined by a Gaussian distribution with a standard-deviation of 40 m for the swarm, 300 m for the subcluster A and 340 m for the subcluster A' (Figure 5.7). Such a Gaussian distribution is expected for uncorrelated location errors [*Hainzl and Fisher, 2002*].

It can be also noted that the solutions for these fitted planes are remarkably similar to those obtained with the moment tensor analysis (Figure 4.32a and 4.32b), which confirms that the hypocenters in the swarm and subcluster A are coplanar and these are indeed defining fault planes.

Since the values of standard-deviation are by far below to the estimated location errors, the variation in z -values mainly results from inaccurate localization. Thus, it is concluded that all earthquakes occur approximately on the same plane and, therefore, the following investigations are restricted to the projections of the hypocenters onto the fitted fault plane.

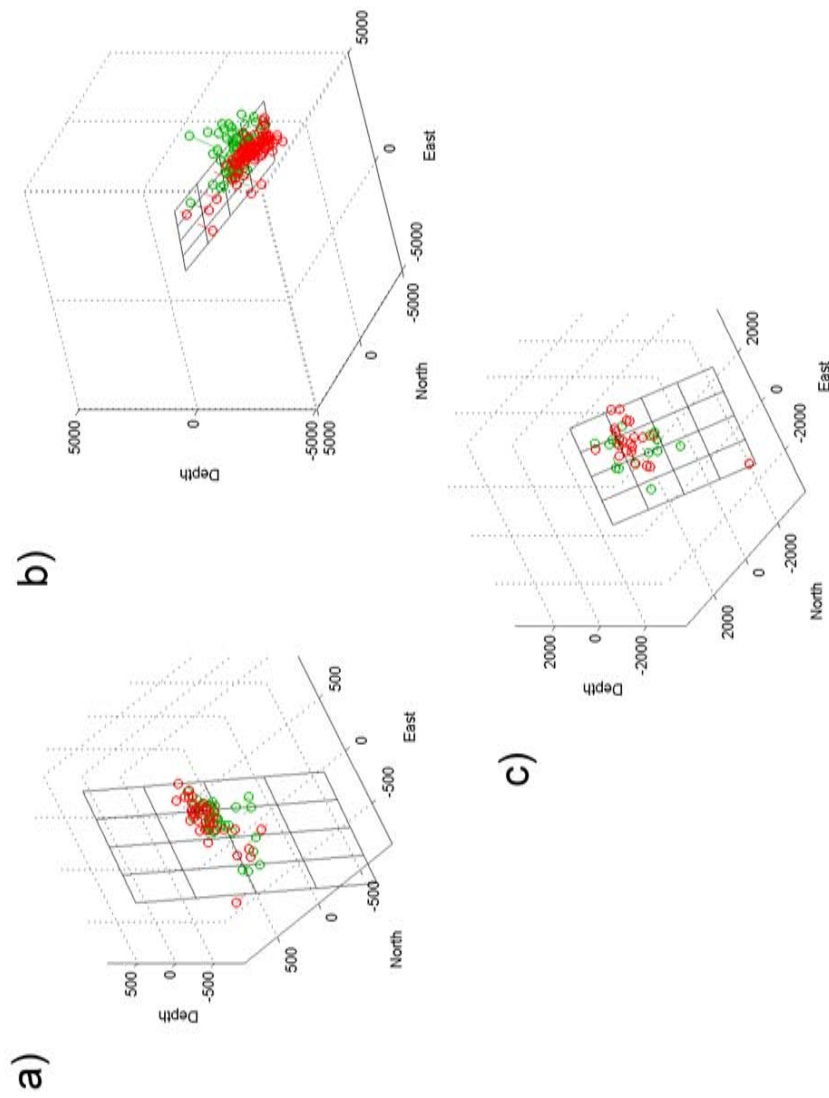


Figure 5.6: The positions of the hypocenters and the fitted fault plane in three dimensional space. (a) Swam, (b) subcluster A, and (c) subcluster A'. The red circles indicate the hypocenters that are above the plane, the green circles indicate below the plane (above and below compared with the normal to the plane in each case).

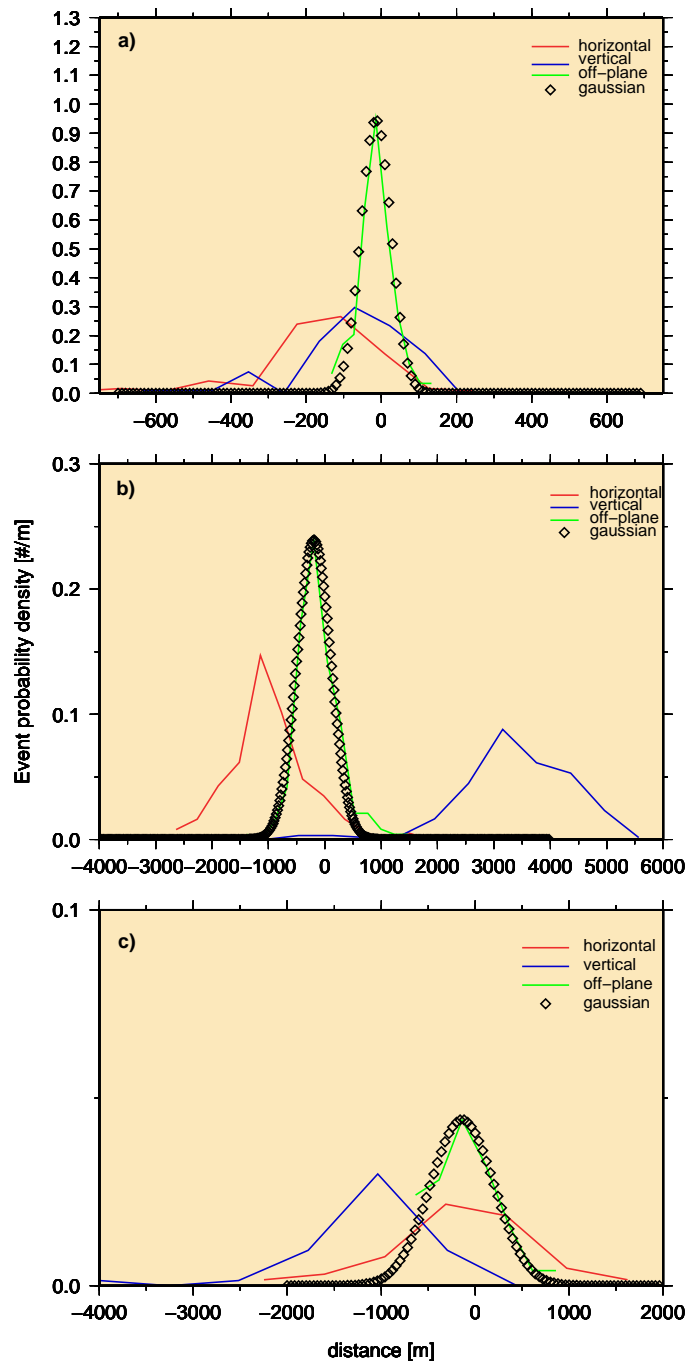


Figure 5.7: The distribution of the x -, y -, and z -values of the all hypocenters in the transformed coordinate system. (a) Swarm, (b) subcluster A and (c) subcluster A'. The variations of the distance perpendicular to the plane (z -value) are more smaller than the variation within the plane (x - and y -values). This fact indicates that all events occur approximately in the same plane.

5.6 Spatiotemporal analysis

The earthquake activity has shown to be almost confined within the planes, which probably result from a preexisting fault structure. To know about the processes which generated these clusters, the spatial evolution over time was studied, in the case of the swarm and subcluster A, respectively (see chapter 3 for further information).

At first view, the spatial growth of the swarm and subcluster A are found to be not proportional to time as would be expected if the earthquakes were triggered by the diffusion of intrusive fluids in a faults with spatially constant material properties (Figure 5.8).

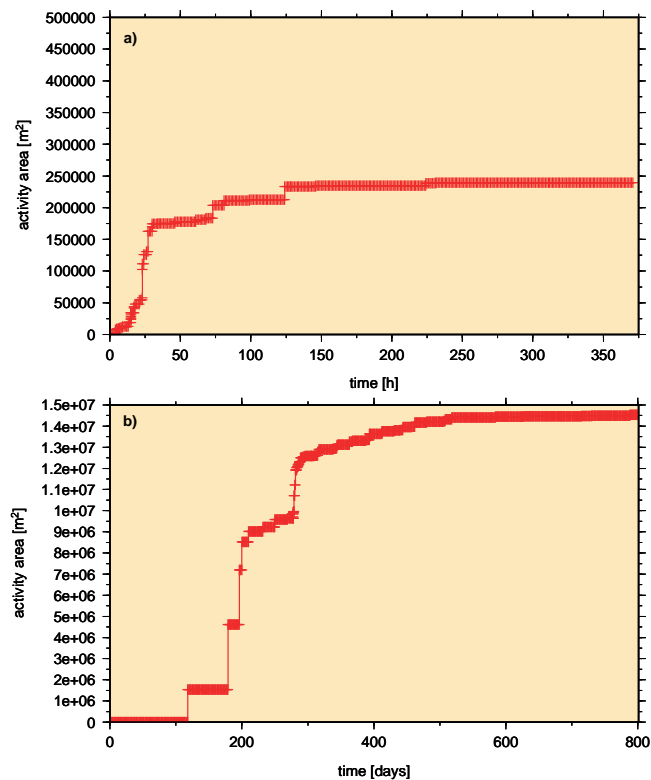


Figure 5.8: The evolution of the area A as a function of the time relative to its initiation. (a) Swarm and (b) subcluster A.

However, if the earthquake number i is used instead of the temporal evolution for characterizing the spatial evolution of the rupture, these become approximately proportional. Thus for both, swarm and subcluster A, the function $A(i)$ can be fitted well by a linear growth $A(i) \propto i$, with a spatial growth rate approximately constant.

In the case of the swarm, three phases of growth of the rupture area at a constant rate and one phase with a fast increase in the rate of growth can be detected (Figure 5.9). The events associated to the phase 1 are found in a small area, defining the beginning of the rupture. In the phases 2 and 3, the events migrate to more deeper locations, whereas in the phase 4 a reactivation of the area covers in the phase 1 and the creation of new areas of rupture are produced.

To the subcluster A, two phases of growth of the rupture area at a constant rate can be detected, separated by two phases with a fast increase in the rate of growth (Figure 5.10). In the phase 1 the activity is very scattered. However in the phase 2 the activity is concentrated in a small area. The activity in the phase 3 becomes scattered again and it is associated to the boundaries of the area defined in the phase 2. The phase 4 shows a high activity and a reactivation of the area covers in the phase 2 and the creation of new areas of rupture are produced.

To the case where the rate of the spatial growth is constant indicates that on average each earthquake leads to a similar increase of the swarm and subcluster A areas. However, this idea does not apply to the phases where the rate of growth has a fast increase producing steps in the growth of the area. Thus, it can be seen that an exactly linear behavior cannot be expected for a heterogeneous rupture growth, being A only a estimate of the real rupture area, which can be distorted by location errors. The analysis of the spatial evolution of the swarm and cluster activity permits to suppose that the earthquake nucleates near the edge of the rupture zone of preceding events.

To clarify whether the new earthquake ruptures tend to be initiated close to the edge of preceding ruptures, the spatial distance of new earthquakes (aftershocks) from their potential trigger events (master shocks) were analyzed.

Following to *Hainzl and Fisher [2002]*, each earthquake is considered a master shock if it is the largest event in the time interval $[t - T_m, t + T_m]$. For each master shock, all earthquakes occurring within $(t, t + T_m]$ are considered as aftershocks, whereas the events within $[t - T_m, 0)$ are considered as foreshocks. The length of the interval is set to $T_m = 40$ [h] for the swarm and $T_m = 550$ [h] for the subcluster A.

The results, in the cases of swarm and subcluster A, are very similar to that expected for tectonic main shocks (Figure 5.11). The aftershock probability is found to decay according to the Omori's law and, in the case of the swarm, the number of aftershocks significantly exceeds the number of foreshocks; to the subcluster A the foreshocks are not present in the chosen time window.

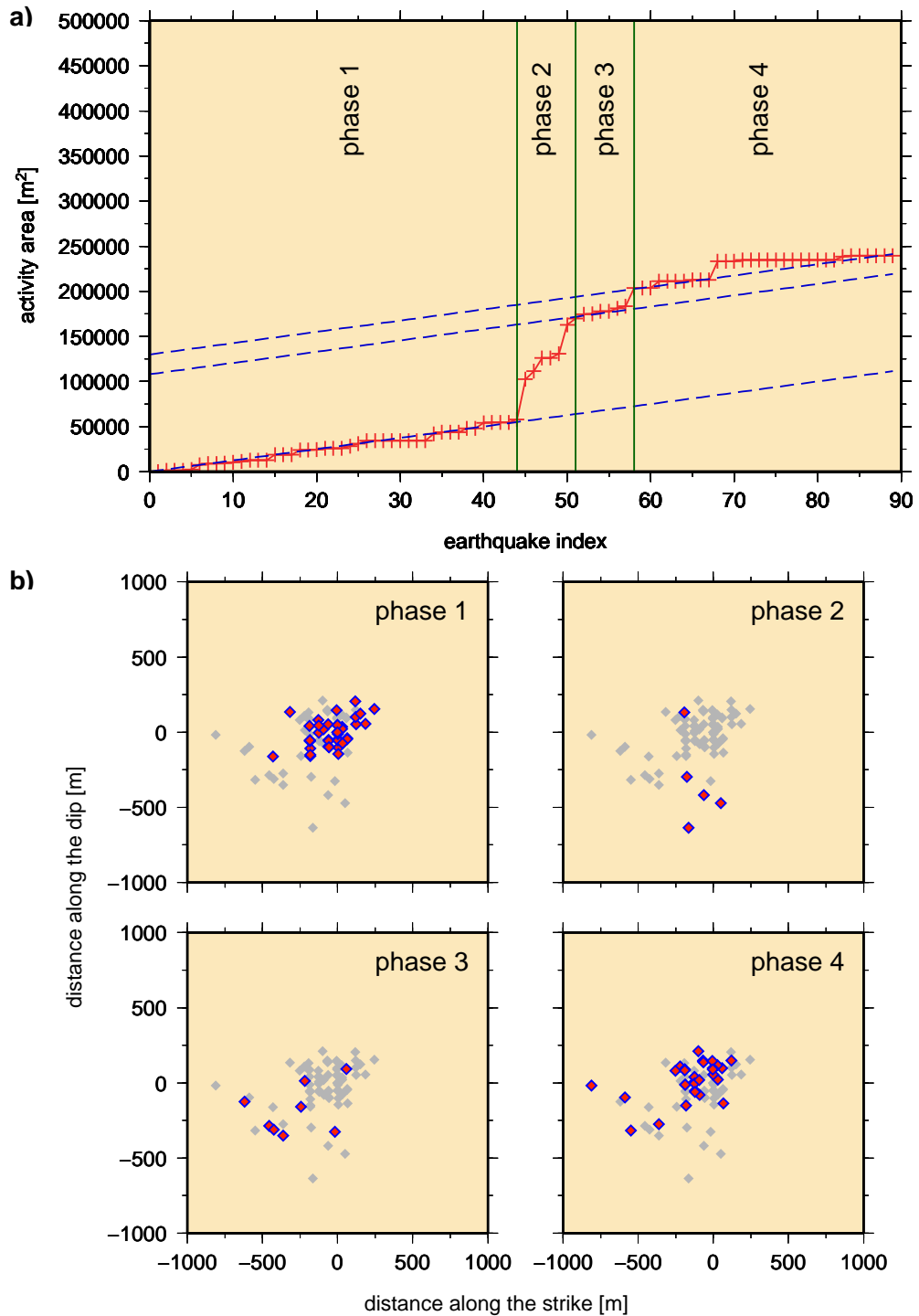


Figure 5.9: Rupture activity of the swarm. (a) The evolution of the area A as a function of the index number i , and (b) the spatial evolution of the activity for the different phases of evolution in the area.

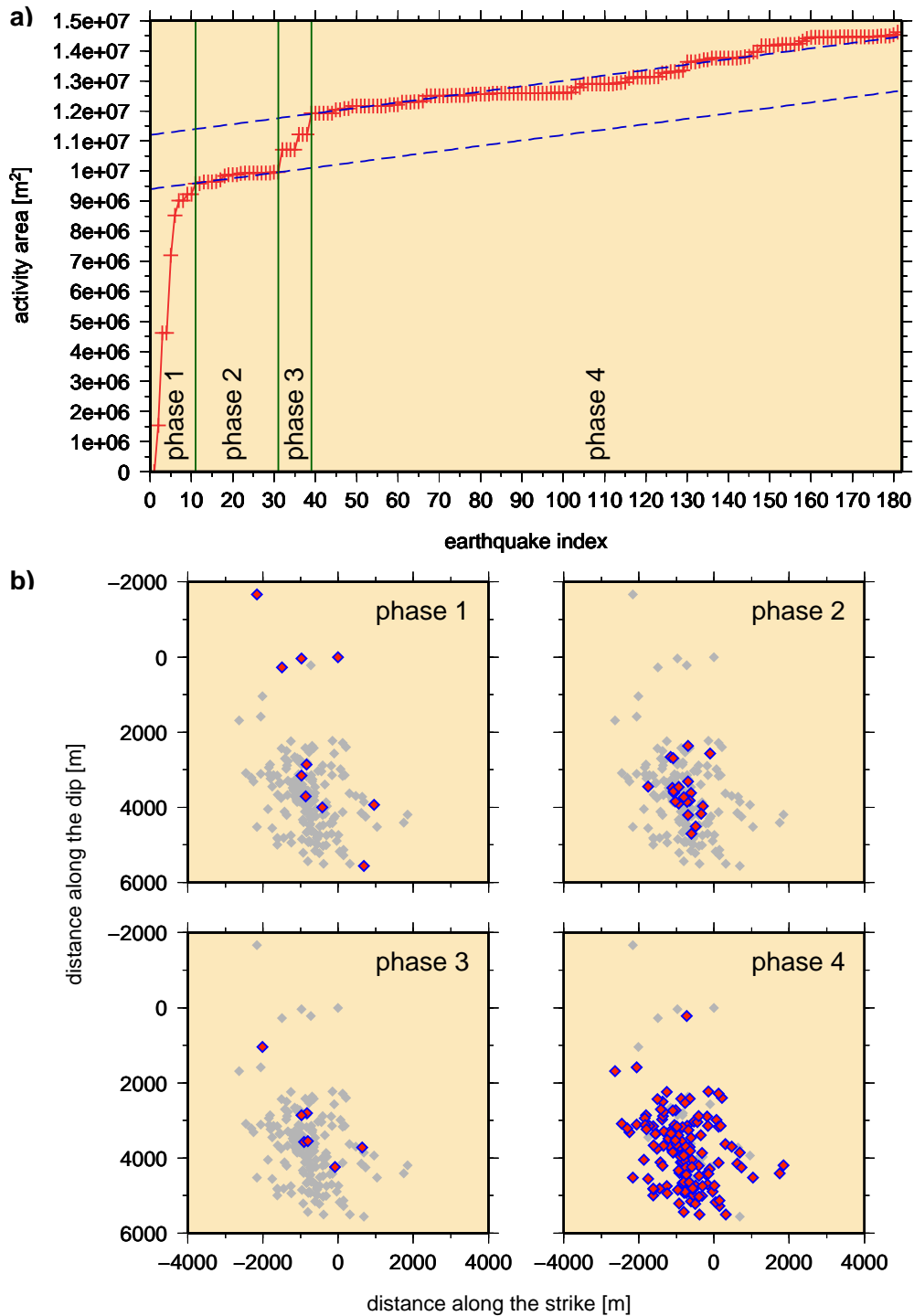


Figure 5.10: Rupture activity of the subcluster A. (a) The evolution of the area A as a function of the index number i , and (b) the spatial evolution of the activity for the different phases of evolution in the area.

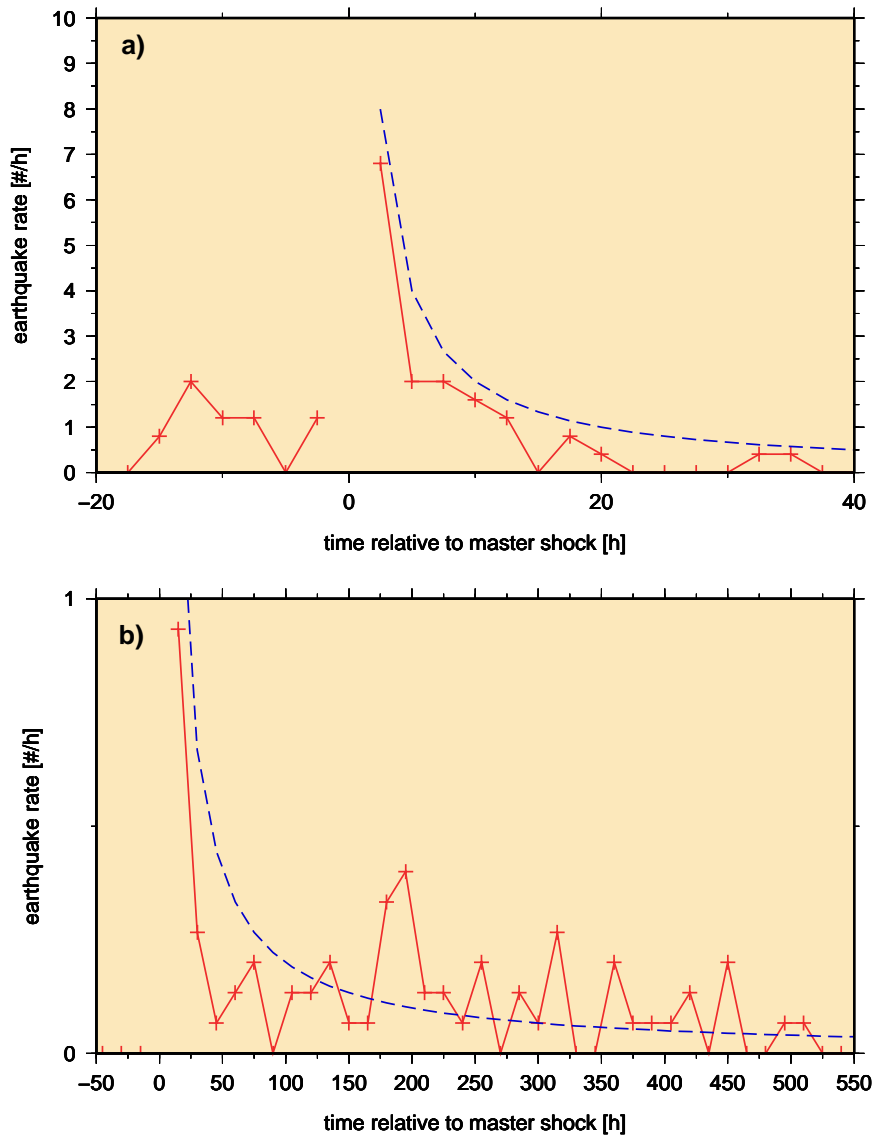


Figure 5.11: The rate of foreshocks and aftershocks is shown as a function of the time for the master shock. (a) Swarm and (b) subcluster A. The blue dashed line represents the Omori's law. The aftershock probability is found to decay according to the Omori's law.

The spatial aftershock density ρ was also calculated, which is determined by counting the number of aftershocks occurring at a distance $r \pm \Delta r/2$ from the master shock as a function of r . This number is normalized by the area $2\pi\Delta r$ to obtain the density ρ . The step width in the case of the swarm is $\Delta r = 15$ m, and to subcluster A $\Delta r = 100$ m. The results indicate that the aftershocks are preferably triggered at the edge of the rupture area (after 150

m, in the case of the swarm, and 500 m for the subcluster A) rather than within the rupture zone of the master event (Figure 5.12).

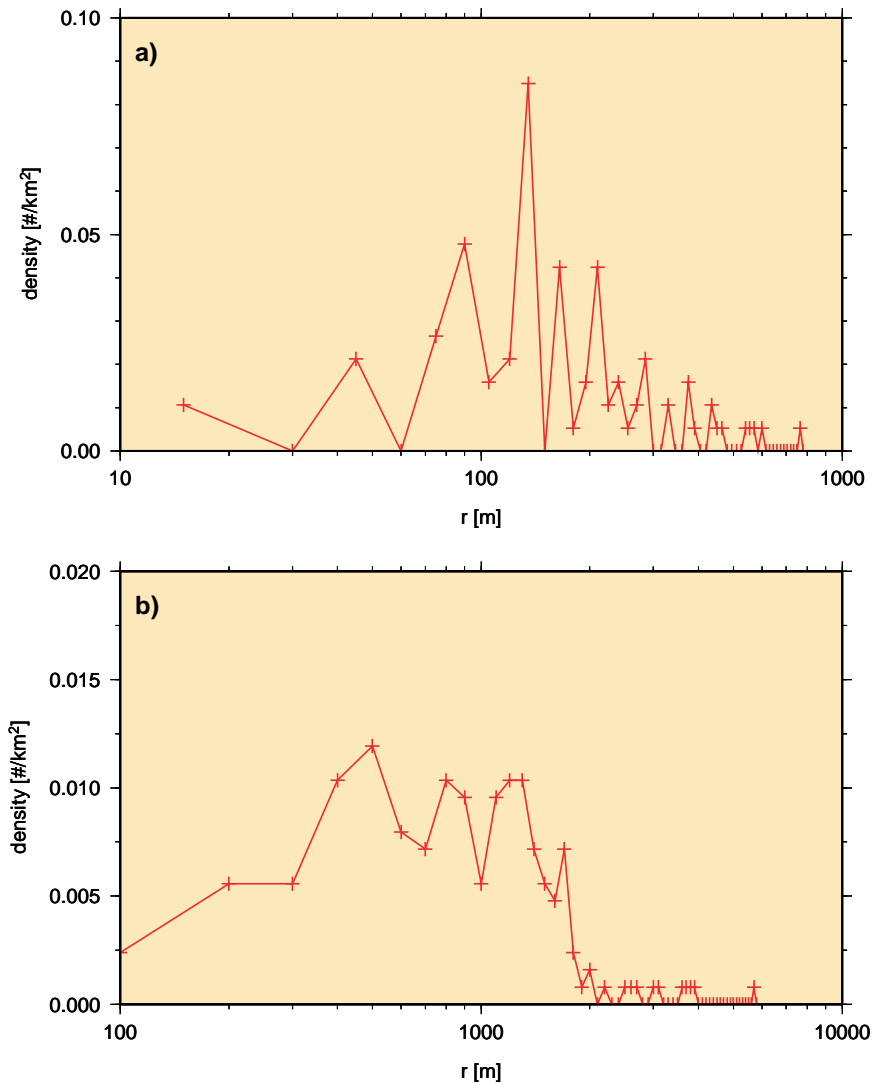


Figure 5.12: The density of aftershocks activity is plotted as a function of distance to the master shock. (a) Swarm and (b) subcluster A. In both cases the aftershocks are preferably triggered at the edge of the rupture.

In the case of the swarm, the result coincides very well with the result of the source radius obtained by spectral analysis, which defines an rupture area of 158 m for the largest event. For the subcluster A, the source radius is 225 m, which confirms that the aftershocks are preferably triggered at the edge of the rupture area.

5.7 Spatiotemporal migration

The sequence of events in the swarm and cluster are compared with the theoretical prediction for fluid induced earthquake activity in order to find a possible influence of fluids in the triggering of the seismic activity.

The hypocenters of the events were found to migrate during the swarm and subcluster A evolution. Thus, as a result of a possible fluid intrusion, the seismic activity starts at depth and spreads with time. The extension of the rupture zone can be approximated by the theoretical curve $\sqrt{4\pi Dt}$, describing the distance of the pressure front from the fluid source [Shapiro *et al.*, 1997]. Although the clustering characteristics are very different, a hypocenter migration is clearly observed in both cases, where the majority of events occur within the parabolic envelope as theoretically expected (Figure 5.13).

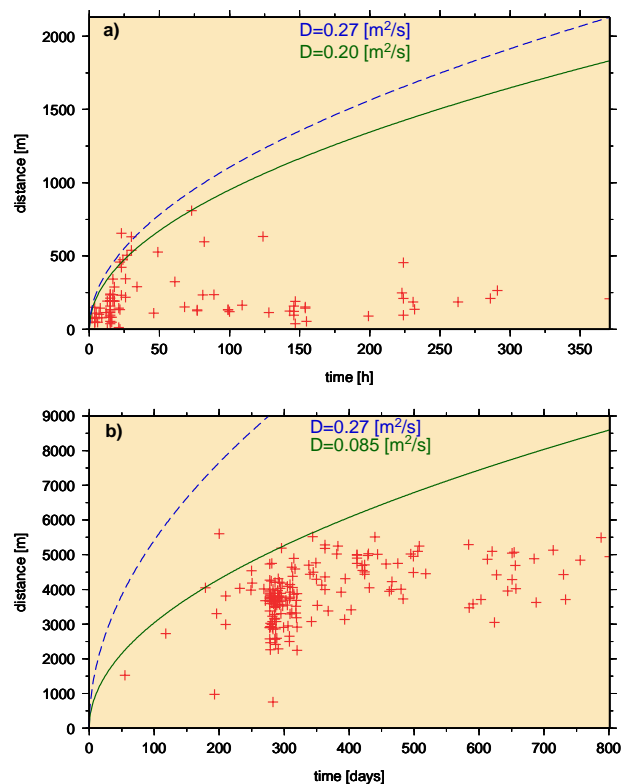


Figure 5.13: Hypocenter distances measured from the first event as a function of the earthquake occurrence times. (a) Swarm and (b) subcluster A. The extension of the rupture can be approximated by the theoretical curve (green line), which describes the distance of the pressure front from the fluid source. Blue line indicates the diffusivity value for the Vogtland swarm [Hainzl and Yosihiko, 2005].

This observation reflects the fact that the initial stress state is subcritical –an initial increase in the pore pressure is necessary to bring the fault into a critical state. The parabola marks the extension of the critical region as function of time. Within the critical loaded region, the stress transfer due to the earthquakes (stress triggering) becomes the dominant triggering process leading to earthquake clustering [Hainzl, 2004].

The values for diffusivity (D) are 0.20 [m²/s] in the case of the swarm and 0.085 [m²/s] in the case of subcluster A. The value of diffusivity in the case of the swarm is very similar to the value calculated for the Vogtland swarm [Hainzl and Yoshihiko, 2005].

5.8 Discussion of the results and the different clusterization models

5.8.1 Intrinsic differences in the earthquake clusterization

Beside structural and tectonic features are observed that some characteristics of the central cluster differ from the SW cluster. Thus, the central cluster B has characteristics of an earthquake swarm –without clear largest event and with a closed distribution in space and time, whereas the SW cluster (subclusters A and A') has typical characteristics of an earthquake cluster at tectonic plate boundaries –with a largest event detected, *b*-values according to a tectonic origin and a long-term duration.

Analyzing the cumulative seismic moment release curves either, swarm and subcluster A, show clearly the occurrence of “jumps”, which coincide with the largest event in each sequence. The last sentence is in apparent contradiction with the observations of the magnitude evolution in the case of the swarm, where there is no a clear largest event in the sequence, but many comparable events in size.

An explanation for this discrepancy is that these jumps are due to the major difference in the seismic release that produce these events with respect to the early ones –there are no another big events in the sequence that release a higher amount of seismic moment, nevertheless should have events with similar magnitude.

Thus, in the case of swarm, this jump in the seismic release does not mean that the swarm has a largest singular event as the subcluster A has, but the swarm has events comparable to the largest one, which cannot be shown in the cumulative seismic release to be a logarithmic graph. In the

case of the subcluster A, the jump reaches two order of magnitude in the cumulative moment release plot, in comparison with the early events, which is in agreement with the occurrence of a strongest event in the sequence as the magnitude distributions show.

5.8.2 Mainshock-aftershock model

In contrast, the similarities found in the swarm and subcluster A permit to infer that they could have a common origin. Thus, the swarm and subcluster A have the features typical for mainshock-aftershock sequences as causality among events, triggering due to the Coulomb stress changes, and shear faulting. Also the interevent-time distribution shows that the background activity –for subcluster A and swarm– is very low, indicating that the major amount of seismic activity would be due to aftershocks.

Also the spatial and moment tensor analysis, in the cases of swarm and subclusters A and A', confirm that the earthquakes are produced almost all coplanar, defining a clear rupture plane. The detailed spatiotemporal analysis shows that the spatial spreading for the swarm and subcluster A are not proportional to time, but they are well-approximated when we use the earthquake number i . Thus, the evolution of the activity areas shows phases with an almost constant rate of growth separated by phases with a fast increase in this growth.

It is also found that the main shocks –in the swarm and subcluster A– triggered aftershock, which preferentially occur at the edge of the rupture zone of preceding event. The analysis of the spreading of the activity area also show that this behavior –where the earthquakes preferentially occur at the edge of the rupture– is not exclusive to the aftershock occurrence, but it is a constant pattern in the all seismic activity of the swarm and subcluster A, respectively.

5.8.3 Ambiguities of the mainshock-aftershock model

There are ambiguities in the attributes pointing out the triggering and driving processes of the swarm and subcluster A. Thus, the long-term seismic activity could not be only explained as a sequence of aftershock.

A possible explanation to the long-term activity can be the diffusion of pressurized fluid, which is proved by fitting a parabolic envelope to the r vs. t plot. Thus, the spatiotemporal migration of swarm and subcluster A reveal that a possible mechanism for triggering the seismic activity is related to migration of fluid, as is shown in the temporal migration of hypocenters,

which coincide with the curve that describe the hypothetical migration of the pressure front from the fluid source.

5.8.4 Stick-slip model

A model that accounts for these ambiguities is presented by *Hainzl* [2004], which provides a hint for it. The model is based on the assumption of pressurized crustal fluids bringing a fault from the subcritical steady-state to the critical state, i.e., to the bound of nucleation. After reaching instability, self-organization of the seismic activities (swarm and subcluster A) prevails.

The relevance of crustal fluids for alteration of the fault conditions in the region in question from the subcritical to critical state was evidenced by the injection experiment at the KTB deep drilling site [*Zoback and Harjes*, 1997]. About 400 $M_L \leq 1.2$ microearthquakes were induced there by hydraulic injection at an average depth of about 9 km.

According to *Zoback and Harjes* [1997], most events were induced by very small pore pressure perturbation which corresponds to a few per cent of hydrostatic pressure at the respective depth. Consequently, *Brudy et al.* [1997] inferred that a steady-state of stress in the brittle crust in the KTB region is limited by the frictional equilibrium on pre-existing favourably oriented faults for hydrostatic pore pressure coefficients of friction $\mu = 0.6 - 0.7$, and that the brittle upper crust in the region is sufficiently strong. These properties are in fact a result of a stick-slip instability, where “stick” represents the interseismic period of the elastic strain accumulation due to creeping of stable portion of the fault, temperature changes and pore pressure variations, and the earthquake sequences represent the “slip”.

Thus, it is possible to infer that faults in the study area are in subcritical steady-state as result of the regional tectonic stress, and their permeable portions can be brought to a critical state due to pore pressure of the crustal fluids.

Fluids play a fundamental role in the transition from subcritical to critical loading of respective fault segments (i.e., in the pre-seismic phase) but during the seismic activities the fluids act mainly in the background and keep the fault segments with the seismic activity in a critical state [*Horálek and Fischer*, 2008].

Movements at the fault segments are controlled by resultant stress resolved into a shear stress τ parallel to the fault and normal stress σ_n perpendicular to it. An optimal ratio between τ and σ_n at a favourably oriented fault results in predominance of the double-couple forces, and such forces bring about the pure shears. In the case of less favourably oriented faults, much higher pore pressure is necessary to bring a portion of the fault into a

critical state. This may give rise to additional tensile forces aiding in opening of the fault and thus induce tensile earthquakes.

5.8.5 The proposed model

The moment tensor, spatial, and spatiotemporal analysis reveal that swarm and subcluster A activities result from a stick-slip type fracture propagation. Although the subcluster A is not located in the upper crust, the influence of a cold Nazca plate permits that the crust at 35 km has a brittle behaviour, which facilitates the development of a stick-slip fracture propagation.

Stick-slip rupture growth can have dynamic as well as structural reason. One possible mechanism is dynamic pore creation in a fluid-permeated fault, where the fluid is assumed to flow out of a localized high-pressure fluid compartment with the onset of earthquake rupture [Yamashita, 1999]. Another mechanism might be structural inhomogeneities combined with visco-elastic coupling due to magma-filled dikes [Hill, 1977].

However, a more probable possibility is that fluids act in a pre-existing structure with a favourable orientation, which results in a predominance of the double-couple forces as the moment tensor analysis reveal.

Thus, an increased pore pressure of the crustal fluids in the region plays a key role in bringing the faults from the subcritical to critical state. The swarm and subcluster A activities are mainly driven by stress changes due to co-seismic and post-seismic slips, which depend on the frictional conditions at the fault; crustal fluids keep the fault in a critical state.

5.8.6 Other geophysical anomalies taken in consideration

The key to understanding the role of the fluids in these processes results from the comparison with the results from other geophysical methods. The swarm and subcluster A have a very good spatial correlation with other geophysical anomalies that were found in previous research.

Yoon *et al.* [2009] based on analysis of zones of high reflectivity and its change in appearance proposed a model of fluid migration in the northern Andean subduction zone (Figures 5.14 and 5.15). Following the explanation given by [Yoon *et al.*, 2009] it is possible to understand the sources that triggered the seismic activity in the subclusters A and A'.

Thus according to Yoon's model, the change in appearance in the Nazca reflector (Figure 5.15, no.1) is attributed to the fact that the oceanic lithosphere starts to release water continuously on the way from point A down

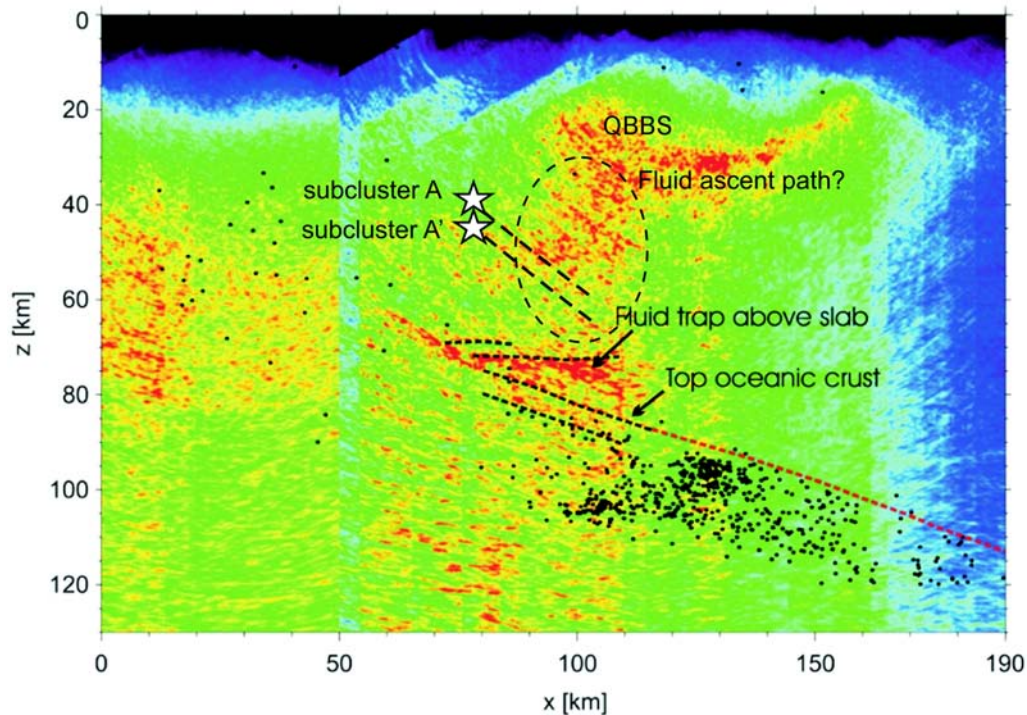


Figure 5.14: The locations of the subclusters A and A' (white stars) are superimposed on the high-frequency image in the range of 10-20 Hz (after *Yoon et al.* [2009]), the black dashed lines indicate the prolongation of the rupture planes associated to the subclusters. The hypocenters location are taken after *Rietbrock and Waldhauser* [2004]. The seismic image reveals a vertically extended heterogeneous zone which is associated with ascent path of fluids released from by the subducted plate, migrating through the overlaying mantle and crust. The internal structure of the Nazca reflector at depth larger than 70 km consists of a strong horizontal reflections indicate a wedge-shaped zone of trapped fluids above the slab. Weaker east dipping reflections below are interpreted as the top of the oceanic crust. The red dashed line shows a good correlation with the Wadati-Benioff zone.

to point B (Figure 5.15, A-B). The released fluids ascend vertically into the overlaying mantle. With the increasing amount of released and ascending fluids, a larger water volume is being trapped in the overlaying mantle wedge, forming a thick serpentinized mantle wedge. This contributes to the thick and blurred appearance of the strong Nazca reflector as observed at depths larger than 70 km (Figure 5.15, no.3). Above and east of the hydrated mantle wedge the temperatures in the forearc region become too high (higher than 500°C) and serpentinization stability breaks down which explains the sudden decrease of reflectivity. However, *Yoon et al.* [2009] link the abrupt lateral

apparent decrease of reflectivity not only to the breakdown of serpentinization, but also to the influence of the Quebrada Blanca Bright Spot (QBBS) on the seismic image (see Figure 5.14).

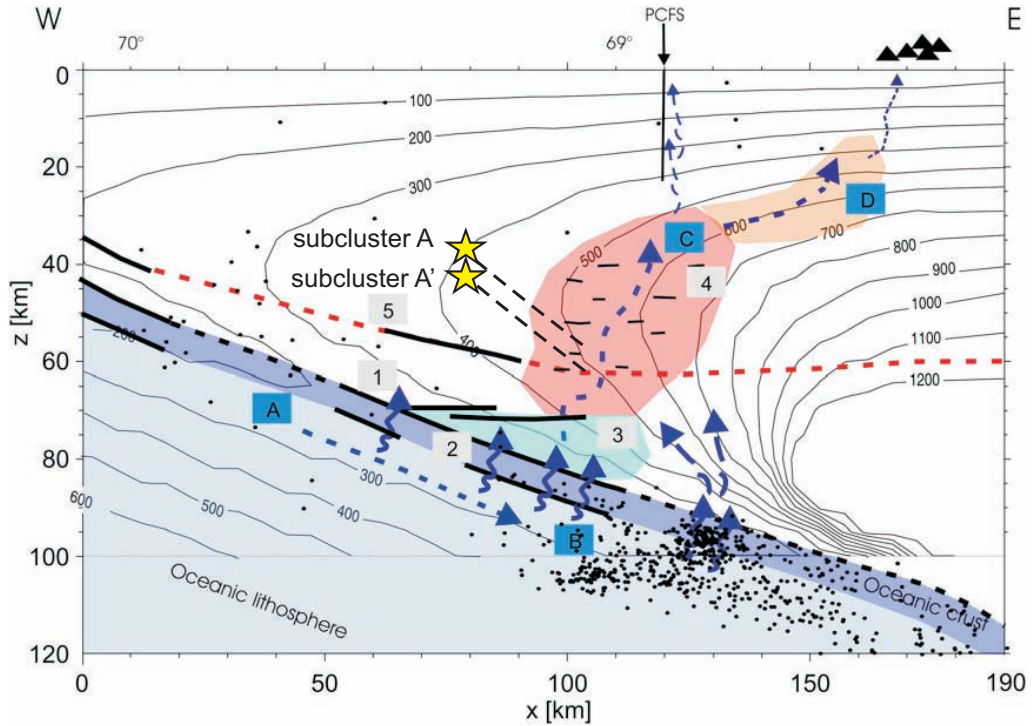


Figure 5.15: Combined results from reflectivity image, receiver function studies [Yuan *et al.*, 2000], local earthquake analysis *Rietbrock and Waldhauser* [2004], geothermal studies [Springer, 1999] and fluid migration scenario for the ANCORP profile at 21°S (after Yoon *et al.* [2009]). The yellow stars indicate the positions of the subcluster A and A', respectively. PCFS: Precordillera fault system. Black solid: verified reflectors from RIS analysis; red magenta: Moho derived from receiver function study; dashed black: top of oceanic crust; grey solid: isotherms; blue arrow: possible fluid and melt migration paths. The numbers 1-5 mark the main important features obtained from RIS, the letters A-D mark way points along the fluids path. For a detailed description of A-D and 1-5, see Figure 9 of Yoon *et al.* [2009].

Due to the breakdown of serpentine stability fluids are released again and migrate towards higher temperatures region by aqueous solutions (dashed blue arrow pointing to C in Figure 5.15). Thereby, the fluid path, eventually along pre-existing faults, are assumed to be not only vertical, but also horizontal and sub-horizontal, building a complex network of fluid and melt migration paths. The reflectivity image (Figure 5.14) reveals a vertical

extended zone of heterogeneous reflections (Figure 5.15, no.4), which is interpreted as the mentioned network of ascending fluids paths indicating that the Nazca reflector is directly linked to the QBBS (Figure 5.15, no.D).

Thus, the subclusters A and A' can be associated to the heterogeneous reflectivity zone and their seismic activity would indicate the migration of fluids through of pre-existing faults that form this complex network of fluid and melt migration paths mentioned above.

On the other hand, the resistivity model derived by magnetotelluric measurements [Brasse *et al.*, 2002] shows a good agreement between seismic and resistivity data that occur beneath the Altiplano, where strong reflections correspond spatially with the upper boundary zone of the Altiplano Conductivity Anomaly. However, there is no correlation of the downgoing slab (Nazca Reflector) nor the QBBS with a conducting zone (Figure 5.16).

The answer for this missing correlation between magnetotelluric and seismic reflections is not well-understood yet.

The more interesting point here is in the forearc, where exists only small singular high conductivity anomaly (Figure 5.16). This good conductor is beneath the Precordillera, its upper boundary is near 15 km, while the lower is not as well resolved [Brasse *et al.*, 2002].

The volcanic front itself is not connected with this conductor zone, therefore this anomaly could be a manifestation of the presence of fluids, which use the pre-existing structures of the West Fissure Fault System as fluid pathway toward the upper crust.

This high conductivity anomaly has a good spatial correlation with the swarm, which is directly located above. This fact support the idea that the source of the swarm activity is related with fluids acting in pre-existing structures of the West Fissure Fault System.

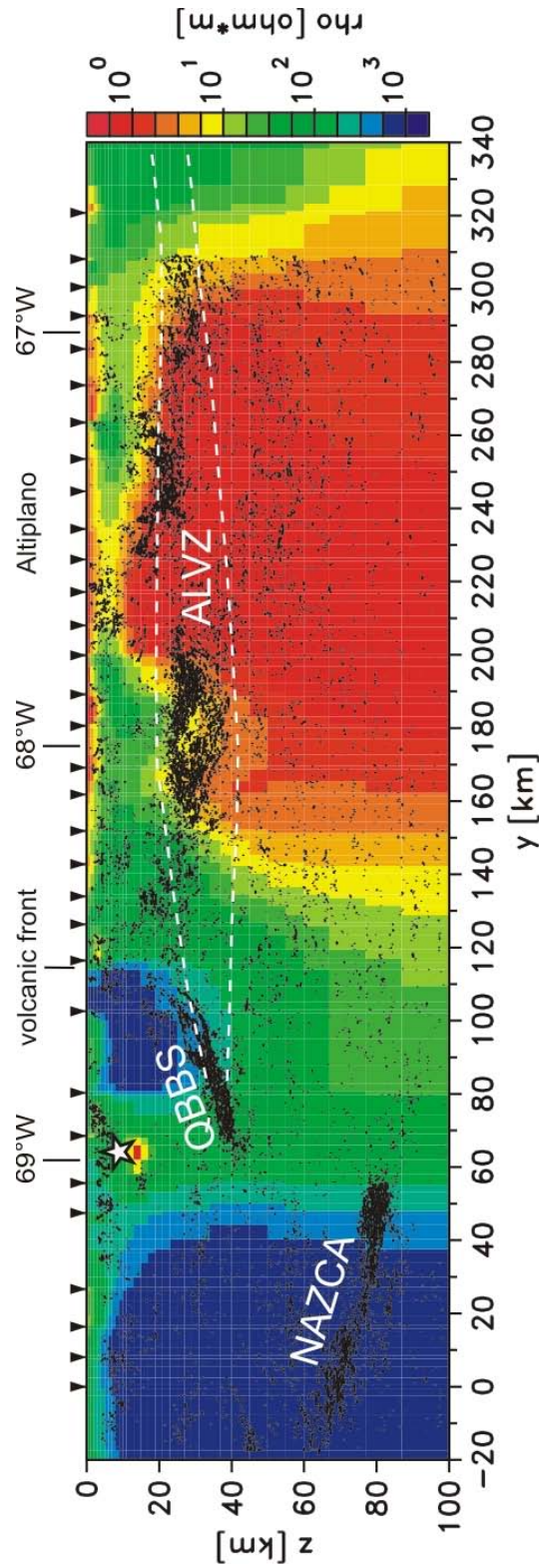


Figure 5.16: Reflection seismic result [ANCORP Working Group, 2003] and the location of the ALVZ (from Andean Low-Velocity Zone) derived from receiver function analysis (after Yuan *et al.* [2000]) are superimposed on the MT model (after Brasse *et al.* [2002]). QBBS (Quebrada Blanca Bright Spot) marks the highly reflective zone in the middle crust of the forearc. The white star indicates the location of the swarm, which is found directly above the high conductivity zone related to the West Fissure Fault System.

Chapter 6

Conclusions

In this thesis I have analyzed high quality crustal microseismicity data from West Fissure Fault System network in the Central Andes, which were recorded during the years 2005-2009.

The research focused on the crustal seismo-tectonic activity in order to specify the structures, stress regime, and the origin of the sources of the clusters. Studying these processes, especially with regard to the importance of fluid migration and stress transference gives us a viewpoint of the role that these phenomena have in the triggering of seismic activity in the crust.

6.1 Tectonic implications

The crustal seismicity in the forearc-Nazca subduction zone shows a sharp lower boundary which can be related to differences in rheological behaviour of the crust (brittle-ductile boundary, which mechanically separates an upper crust with a rigid behavior from a ductile lower one). However, this boundary is also possibly correlated to a deep reverse tectonic structure which could be part of the edges of a slab-forearc system.

Thus, geometrically is created a triangular zone (composed by the slab and the west dipping reverse structure), which is interpreted as a rigid, indenter-like backstop that has resisted the westward movement of crustal material coming from the shortened eastern foreland.

The upper part of this reverse structure could be related west vergent thrust system (WTS), which is responsible for the Late Cenozoic deformation and uplift of the western flank of the Altiplano in northern Chile [Farías *et al.*, 2005], a final tectonic interpretation is shown in Figure 4.40.

Also, some important earthquake clusterization was found in different levels of the crust, spatially related to the reverse structure mentioned above,

even one of the clusters has characteristics of an earthquake swarm.

The single solution for the regional stress field shows a tensional regime for the area. This, at first view, is contrary to what we would expect in a convergent margin zone. But this can be explained by gravitational forces, local forces related to the most elevated zones of the Andes, which influence the regional stress field.

However, when the structural patterns from geological data are taken into consideration in order to individualize tectonic signatures, the results of the stress analysis reflect the existence of a clear compressional behavior on the west side of the main trace of WFFS, whereas the east side is affected by tensional and strike-slip regimes. Thus, the state of stress in the convergence margin is related to compression, supporting the idea of this rigid, indenter-like backstop, whereas the extension is only a manifestation of local forces associated with the highest areas in the Andes.

6.2 Fluid migration implications

The analysis of the clustering data revealed that the swarm and clusters occur in a coplanar distribution, with b -value characteristic to plate tectonic boundaries in the case of subcluster A, and with a slightly low b -value in the case of the swarm, which can be explained as a cycle of seismic moment accumulation.

The low value for the background seismicity –in the swarm and subcluster A– indicate that only part of the events can be related to aftershock sequence, however an important amount of seismicity cannot be directly related to them, because the seismic activity in the swarm and subcluster A are long-term and the magnitudes for the largest events are so low to maintain this behavior over time.

The main part of the swarm and subcluster A seismic activity are seen as the result of a stick-slip type of fracture propagation triggered by the presence of fluids. Thus, the statistical characteristics and space-time distribution of the hypocenters show a dominance of the stress redistribution in running the earthquake activities in the swarm and subcluster A (b -values, gamma distributions, etc.). The spatiotemporal migration of hypocenters are in agreement with the propagation of a possible front of pressure of a fluid source. Also, the good spatial correlation that the swarm and subcluster A have with areas that were interpreted as fluid migration zones by previous research confirms our assumptions.

Thus, the source mechanism studies point out the predominance of double-couple forces and the fluids play a key role in the alteration of the pre-

existing favourably oriented fault from subcritical to critical state (exceeding the frictional equilibrium on the fault) due to pore pressure increase. After bringing the fault to instability, the swarm and subcluster activities are mainly driven by the stress changes due to co-seismic and post-seismic slips which considerably depend on the frictional conditions at the fault, thus, crustal fluids keep the fault in a critical state.

Bibliography

- Allmendinger, R., and T. Gubbels (1996), Pure and simple shear plateau uplift, Altiplano-Puna, Argentina and Bolivia, *Tectonophysics*, *259*, 1–13.
- Allmendinger, R., T. Jordan, S. Kay, and B. Isacks (1997), The evolution of the Altiplano-Puna Plateau of the central Andes, *Annu. Rev. Earth. Planet. Sci.*, *25*, 139–174.
- ANCORP Working Group (1999), Seismic reflection image revealing offset of andean subduction-zone earthquake locations into oceanic mantle, *Nature*, *397*, 341–344.
- ANCORP Working Group (2003), Seismic imaging of an active continental margin and plateau in the central Andes (Andean Continental Research Project 1996 (ANCORP'96)), *J. Geophys. Res.*, *108*(B7), 2328, doi:10.1029/2002JB001771.
- Angermann, D., J. Klotz, and C. Reiber (1999), Space-geodetic estimation of the Nazca-South American Euler vector, *Earth and Planetary Science Letters*, *171*, 329–334.
- Baby, P., P. Rochat, G. Mascle, and G. Hérail (1997), Neogene shortening contribution to crustal thickening in the back arc system of the Bolivian Orocline (central Andes), *Geology*, *25*, 883–886.
- Bak, P., K. Christensen, L. Danon, and T. Scanlon (2002), Unified scaling law for earthquakes, *Phys. Rev. Lett.*, *88*(178501).
- Barth, A., J. Reinecker, and O. Heidbach (2008), *World Stress Map Project*, chap. Stress derivation from earthquake focal mechanisms, World Stress Map Project.
- Beck, M. (1983), On the mechanism of tectonic transport in zones of oblique subduction, *Tectonophysics*, *93*, 1–11.

- Beck, S., and G. Zandt (2002), The nature of orogenic crust in central Andes, *J. Geophys. Res.*, *107*(B10), doi:10.1029/2000JB000124.
- Beck, S., P. Silver, L. Drake, G. Zandt, S. Myers, and T. Wallace (1996), Crustal-thickness variations in the central andes, *Geology*, *24*, 407–410.
- Belmonte-Pool, A. (2002), Krustale Seismizität Struktur und Rheologie der Oberplate zwischen der Präkordillere und dem magmatischen Bogen in Nordchile (22°S-24°S), Ph.D. thesis, Freie Universität Berlin, Berlin.
- Bird, P. (2003), An updated digital model of plate boundaries, *Geochem. Geophys. Geosyst.*, *4*(3), 1027, doi:10.1029/2001GC000252.
- Bock, G., B. Schurr, and G. Asch (2000), High-resolution receiver function image of the oceanic moho in the subducting nazca plate from p-s converted waves, *Geophys. Res. Lett.*, *27*(23), 3929–3932.
- Bouchon, M. (2003), A review of the discrete wavenumber method, *Pure Appl. Geophys.*, *160*, 445–465.
- Brasse, H., P. Lezaeta, V. Rath, K. Schwalenberg, W. Soyer, and V. Haak (2002), The Bolivian Altiplano conductivity anomaly, *J. Geophys. Res.*, *107*(B5), doi:10.1029/2001JB000391.
- Brudy, M., M. Zoback, K. Fuchs, F. Rummel, and J. Baumgärtner (1997), Estimation of the complete stress tensor to 8 km depth in the KTB scientific drill holes: Implication for crustal strength, *J. Geophys. Res.*, *102*(B8), 18,453–18,475.
- Brune, J. (1970), Tectonic stress and spectra of seismic shear waves, *J. Geophys. Res.*, *75*, 4997–5009.
- Cahill, T., and B. Isacks (1992), Seismicity and shape of the subducted nazca plate, *J. Geophys. Res.*, *97*(B12), 17,503–17,529.
- Campus, P., and D. Faeh (1997), Seismic monitoring of explosions: a method to extract information on the isotropic component of the seismic source, *J. Seismol.*, *1*, 205–218.
- Camus, F. (2003), *Geología de los sistemas porfídicos de los Andes de Chile*, Servicio Nacional de Geología y Minería, Santiago-Chile, 267pp.
- Coira, B., J. Davidson, C. Mpodozis, and V. Ramos (1982), Tectonic and magmatic evolution of the Andes of northern Argentina and Chile, *Earth Sci. Rev.*, *18*, 303–332.

- Comte, D., M. Pardo, L. Dorbath, H. Haessler, and L. Ponce (1992), Crustal seismicity and subduction morphology around Antofagasta, Chile, *Tectonophysics*, *205*, 13–22.
- Cordani, U., and K. Sato (1999), Crustal evolution of the south american platform, based on nd isotopic systematics on granitoid rocks, *Episodes*, *22*(3), 167–173.
- Corral, A. (2006), Dependence of earthquake recurrence times and independence of magnitudes on seismicity hitory, *Tectonophysics*, *424*, 177–193.
- Creager, K., L. Chiao, J. Winchester, and R. Engdahl (1995), Membrane strain rate in the subducting plate beneath South America, *Geophys. Res. Lett.*, *22*(16), 2321–2324.
- David, C. (2007), Comportamiento actual del ante-arco y del arco del codo de Arica en la orogénesis de los Andes centrales, Ph.D. thesis, Departamento de Geofísica, Universidad de Chile.
- David, C., J. Martinod, D. Comte, G. Hérail, and H. Haessler (2002), Intracontinental seismicity and Neogene deformation of the Andean forearc in the region of Pica (18.5°S-19.5°S), in *5th International Symposium on Andean Geodynamics*, Ins. de Rech. pour le Dév. (IRD), Toulouse-France.
- de Silva, S. (1989), Altiplano-Puna volcanic complex of the Central Andes, *Geology*, *17*, 1102–1106.
- Dregger, D., and B. Woods (2002), Regional distance seismic moment tensors of nuclear explosions, *Tectonophysics*, *356*, 139–156.
- Elger, K., O. Oncken, and J. Glodny (2005), Plateau-style accumulation: Southern Altiplano, *Tectonics*, *24*(TC4020).
- Farías, M., R. Charier, D. Comte, J. Martinod, and G. Hérail (2005), Late Cenozoic deformation and uplift of the western flank of the Altiplano: Evidence from the depositional, tectonic, and geomorphologic evolution and shallow seismic activity (northern Chile at 19°30'S), *Tectonics*, *24*(TC4001), doi:10.1029/2004TC001667.
- Fitch, T. (1972), Plate convergence, transcurrent faults, and internal deformation adjacent to southeast Asia and the western Pacific, *J. Geophys. Res.*, *77*, 4432–4460.

- Font, Y., H. Kao, S. Lallemand, C.-S. Liu, and L.-Y. Chiao (2004), Hypocentral determination offshore eastern Taiwan using the maximum intersection method, *Geophys. J. Int.*, *158*, 655–675.
- Frohlich, C. (1994), Earthquakes with non-double-couple mechanisms, *Science*, *264*, 804–809.
- García, M., G. Hérail, R. Charrier, G. Mascle, M. Fornari, and C. Perez de Arce (2002), Oligocene-Neogene tectonic evolution of northern Chile (18°–19°S), in *5th International Symposium of Andean Geodynamics*, pp. 235–237, Toulouse, France.
- Gerbault, M., G. Hérail, and J. Martinod (2002), Numerical modelling of deformation processes in the Andes, in *5th International Symposium on Andean Geodynamics*, Inst. de Rech. pour le Dév. (IRD), Toulouse, France.
- Gill, J. (1981), *Orogenic Andesites and Plate Tectonics*, Springer, New York.
- Goldstein, H. (1959), *Classical Mechanics*, Addison-Wesley, London.
- Gonzalez, G., T. Dunai, D. Carrizo, and R. Allmendinger (2006), Young displacements on the Atacama fault system, northern Chile from field observations and cosmogenic ²¹Ne concentrations, *Tectonics*, *25*(TC3006), doi:10.1029/2005TC001854.
- Gonzalez, R., and R. Woods (1992), *Digital image processing*, Addison Wesley Publishing Company.
- Graeber, F., and G. Asch (1999), Three dimensional models of P-wave velocity and P-to-S velocity ratio in the southern Central Andes by simultaneous inversion of local earthquake data, *J. Geophys. Res.*, *104*, 20,237–20,256.
- Gregory-Wodzicki, K. (2000), Uplift history of the Central and Northern Andes, *GSA Bulletin*, *112*, 1091–1105.
- Gripp, A., and R. Gordon (2002), Young tracks of hotspots and current plate velocities, *Geophys. J. Int.*, *150*, 321–361.
- Gruber, D. (2000), The Mathematics of the 3D Rotation Matrix, in *The Xtreme Game Developers Conference*, Santa Clara, California.
- Gubbels, T., L. Isacks, and E. Farrar (1993), High-level surfaces, plateau uplift, and foreland development, Bolivian central Andes, *Geology*, *21*, 695–698.

- Gutenberg, B., and C. Richter (1956), Earthquake magnitude, intensity, energy and acceleration, *Bull. Seismol. Soc. Am.*, *46*, 105–145.
- Gutscher, M.-A., W. Spakman, H. Bijwaard, and R. Engdahl (2000), Geodynamics of the flat subduction: seismicity and tomographic constraints from the Andean margin, *Tectonics*, *19*, 814–833.
- Haberland, C., and A. Rietbrock (2001), Attenuation tomography in the western central Andes: A detailed insight into the structure of a magmatic arc, *J. Geophys. Res.*, *106*(B6), 11,151–11,167.
- Hainzl, S. (2003), Self-organization of earthquake swarms, *Journal of Geodynamics*, *35*, 157–172.
- Hainzl, S. (2004), Seismicity pattern of earthquake swarms due to fluid intrusion and stress triggering, *Geophys. J. Int.*, *159*, 1090–1096, doi:10.1111/j.1365-246X.2004.02463.x.
- Hainzl, S., and T. Fisher (2002), Indications for a successively triggered rupture growth underlying the 2000 earthquake swarm in Vogtland/NW Bohemia, *J. Geophys. Res.*, *107*(B12), doi:10.1029/2002JB001865.
- Hainzl, S., and O. Yoshihiko (2005), Detecting fluid signal in seismicity data through statistical earthquake modeling, *J. Geophys. Res.*, *110*(B05S07), doi:10.1029/2004JB003247.
- Hainzl, S., F. Scherbaum, and C. Beauval (2006), Estimating background activity based on interevent-time distribution, *Bull. of the Seismol. Soc. of Am.*, *96*(1), 313–320, doi:10.1785/0120050053.
- Hartley, A., M. Geoffrey, G. Chong, S. Turner, S. Kape, and E. Jolley (2000), Development of a continental forearc: a Cenozoic example from the Central Andes, northern Chile, *Geology*, *28*, 331–334.
- Haschke, M., and A. Günter (2003), Balancing crustal thickening in arcs by tectonic vs. magmatic means, *Geology*, *31*, 933–936.
- Haschke, M. W. S., A. Günther, and E. Scheuber (2002), Repeated crustal thickening and recycling during the andean orogeny in northern chile (21°–26°S), *J. Geophys. Res.*, *107*(B1), doi:10.1029/2001JB000328.
- Havskov, J., and L. Ottemöller (2000), SEISAN earthquake analysis software, *Seism. Res. Lett.*, *70*, 532–534.

- Heit, B. (2005), Teleseismic Tomographic Images of the Central Andes at 21°S and 25.5°S: An inside look at the Altiplano and Puna Plateau, Ph.D. thesis, Fachbereich Geowissenschaften der Freien Universität Berlin.
- Heraïl, G., J. Oller, P. Baby, M. Bonhomme, and P. Soler (1996), Strike-slip faulting, thrusting and related basins in the Cenozoic evolution of the southern branch of the Bolivian Orocline, *Tectonophysics*, *259*, 201–212.
- Herrmann, R. (1985), An extension of random vibration theory estimates of strong ground motion to large distances, *Bull. Seism. Soc. Am.*, *75*, 1447–1453.
- Herrmann, R., and A. Kijko (1983), Modelling some empirical vertical component lg relations, *Bull. Seism. Soc. Am.*, *73*, 157–171.
- Hill, D. (1977), A model for earthquake swarms, *J. Geophys. Res.*, *82*, 1347–1352.
- Hoke, L., D. Hilton, S. Lamb, K. Hammerschmidt, and H. Friedrichson (1994), ³He evidence for a wide zone of active mantle melting beneath the central andes, *Earth Planet. Sci. Lett.*, *128*, 341–355.
- Horálek, J., and T. Fischer (2008), Role of crustal fluids in triggering the west Bohemia/Vogtland earthquake swarms: Just what we know (a review), *Stud. Geophys. Geod.*, *52*, 455–478.
- Husson, L., and T. Sempere (2003), Thickening the Altiplano crust by gravity-driven crustal channel flow, *Geophys. Res. Lett.*, *30*(5), doi: 10.1029/2002GL016877.
- Hutton, L., and D. Boore (1987), The M_L scale in Southern California, *Bull. Seis. Soc. Am.*, *77*, 2074–2094.
- Isacks, B. (1988), Uplift of the central Andean plateau and bending of the Bolivian Orocline, *J. Geophys. Res.*, *93*(3211–3231).
- Jacay, J., T. Sempere, L. Husson, and A. Pino (2002), Structural characteristics of the Incapuquio fault system, southern Peru, in *5th International Symposium of Andean Geodynamics*, pp. 319–321, Toulouse, France.
- Janssen, C., A. Hoffmann-Rothe, S. Tauber, and H. Wilke (2002), Internal structure of the Precordillera fault system (Chile) – insights from structural and geophysical observations, *Journal of Structural Geology*, *24*, 123–143.

- Jordan, T., B. Isacks, R. Allmendinger, J. Brewer, and V. Ramos (1983), Andean tectonics related to geometry of the subducted Nazca plate, *Geological Society of American Bulletin*, *94*, 341–361.
- Jost, M., and R. Hermann (1989), A student's guide to and review of moment tensor, *Seism. Res. Lett.*, *60*, 37–57.
- Julian, B., A. Miller, and G. Foulger (1998), Non-double-couple earthquakes 1. theory, *Rev. Geophys.*, *36*, 525–549.
- Kagan, Y. (1991), Likelihood analysis of earthquake catalogs, *Geophys. J. Int.*, *106*, 135–148.
- Kanamori, H. (1977), The energy release in great earthquakes, *J. Geophys. Res.*, *82*, 1981–1987.
- Karnik, V., Z. Schenkova, and V. Schenk (1986), Time pattern of the swarm of December 1985–March 1986 in West Bohemia, in *Proceeding of the Workshop in Lazne: Earthquake Swarm 1985/86 in Western Bohemia*, pp. 328–342.
- Kay, S., and J. M. Abbruzzi (1996), Magmatic evidence for Neogene lithospheric evolution of the central Andes "flat slab" between 30°S and 32°S, *Tectonophysics*, *259*, 15–28.
- Kay, S., C. Mpodozis, V. Ramos, and F. Munizaga (1991), Magma source variations for mid-late Tertiary magmatic rocks associated with a shallowing subduction zone and a thickening crust in the central Andes (28 to 33°S), *Spec. Pap. Geol. Soc. Am.*, *265*, 113–137.
- Kay, S., C. Mpodozis, and B. Coira (1999), *Geology and Ore Deposits of the Central Andes*, *Spec. Publ. SEPM Soc. Sediment. Geol.*, vol. 7, chap. Neogene magmatism, tectonics, and mineral deposits of the central Andes (22 to 33°S), pp. 27–59.
- Khatti, K. (1973), Earthquake focal mechanisms studies—a review, *Earth Sci. Rev.*, *9*, 19–63.
- Kikuchi, M., and H. Kanamori (1991), Inversion of complex body waves-III, *Bull. Seismol. Soc. Am.*, *81*, 2335–2350.
- Kisslinger, C., J. Bowman, and K. Koch (1981), Procedures for computing focal mechanisms from local (*SV/P*) data, *Bull. Seism. Soc. Am.*, *71*, 1719–1729.

- Kisslinger, C., J. Bowman, and K. Koch (1982), Determination of the focal mechanisms from (*SV/P*) amplitude ratios at small distances, *Phys. Earth and Planet. Inter.*, *30*, 172–176.
- Kley, J., and C. Monaldi (1998), Tectonic shortening and crustal thickness in the central Andes: How good is the correlation?, *Geology*, *26*, 723–726.
- Kley, J., C. Monaldi, and J. Salfity (1999), Along-strike segmentation of the Andean foreland, causes and consequences, *Tectonophysics*, *301*, 75–94.
- Kono, M., Y. Fukao, and A. Yamamoto (1989), Mountain building in the central Andes, *J. Geophys. Res.*, *94*, 3891–3905.
- Kröner, A., and U. Cordani (2003), African, southern Indian and South American cratons were not part of the Rodinia supercontinent: evidence from field relationship and geochronology, *Tectonophysics*, *375*(1-4), 325–352.
- Lamb, S., and L. Hoke (1997), Origin of the high plateau in the central Andes, Bolivia, South America, *Tectonics*, *16*, 623–649.
- Lamb, S., L. Hoke, L. Kennan, and J. Dewey (1997), *Orogens Through Time*, vol. 121, chap. Cenozoic evolution of the central Andes in Bolivia and northern Chile, pp. 237–264, Geol. Soc. Spec. Publ.
- Le Meur, H., J. Virieux, and P. Podvin (1997), Seismic tomography of the gulf of corinth: a comparison of methods, *Ann. Geofis.*, *60*, 1–24.
- Legrand, D., B. Delouis, L. Dorbath, C. David, J. Campos, L. Marquéz, J. Thompson, and D. Comte (2007), Source parameters of the $M_W = 6.3$ Aroma crustal earthquake of July 24, 2001 (northern Chile), and its aftershock sequence, *J. South Am. Earth Sci.*, *24*, 58–68.
- Lindsay, D., M. Zentilli, and A. Rivera (1995), Evolution of an active ductile to brittle shear system controlling mineralization at Chuquicamata porphyry copper deposit, northern Chile, *International Geology Review*, *37*, 945–958.
- Lomax, A., J. Virieux, P. Volant, and C. Berge (2000), *Advances in Seismic Event Location*, chap. Probabilistic earthquake location in 3D and layered models: Introduction of a Metropolis-Gibbs method and comparison with linear locations, pp. 101–134, Kluwer-Amsterdam.

- Lomax, A., A. Zollo, P. Capuano, and J. Virieux (2001), Precise, absolute earthquake location under somma-vesuvius volcano using a new three-dimensional velocity model, *Geophys. J. Int.*, *146*, 313–331.
- Lüth, S. (2000), Results of wide-angle investigations and crustal structure along a traverse across the central andes at 21 degrees south, *Berliner Geowissenschaftliche Abhandlungen, Band 37, Reihe B*, Institute of Geology, Geophysics and Geoinformatics, Free University of Berlin, Berlin-Germany.
- Marret, R., and M. Strecker (2000), Response of intracontinental deformation in the central Andes to late Cenozoic reorganization of South American Plate motions, *Tectonics*, *19*(3), 452–467.
- McCaffrey, R. (1996), Estimates of modern arc-parallel strain rates in fore arcs, *Geology*, *24*(1), 27–30.
- McQuarrie, N. (2002), The kinetic history of the central Andean fold-thrust belt, Bolivia: Implications for building a high plateau, *Geol. Soc. Am. Bull.*, *114*, 950–963.
- McQuarrie, N., and P. DeCelles (2001), Geometry and structural evolution of the central Andean back-thrust belt, Bolivia, *Tectonics*, *20*, 669–692.
- Meijer, P., R. Govers, and M. Wortel (1997), Forces controlling the present-day state of stress in the Andes, *Earth Planet. Sc. Lett.*, *148*, 157–170.
- Mittag, R. (2000), Statistical investigations of earthquake swarms within the Vogtland/NW-Bohemia area, *Studia Geophys. Geod.*, *44*, 465–474.
- Mogi, K. (1962), Magnitude-frequency relations for elastic shocks accompanying fractures of various materials and some related problems in earthquakes, *Bull. Earthquake Res. Inst. Univ. Tokyo*, *40*, 831–853.
- Molchan, G. (2005), Interevent time distribution in seismicity: a theoretical approach, *Pure Appl. Geophys.*, *162*, 1135–1150.
- Moser, T., T. van Eck, and G. Nolet (1992), Hypocenter determination in strongly heterogeneous earth models using the shortest path method, *J. Geophys. Res.*, *97*, 6563–6572.
- Mpodozis, C., and V. Ramos (1989), *Geology of the Andes and its Relation to Hydrocarbon and Mineral Resources*, vol. 11, chap. The Andes of Chile and Argetina, pp. 59–90, Circum-Pacific Council for Energy and Mineral Resources Earth Sciences Series.

- Muñoz, N., and R. Charrier (1996), Uplift of the western border of the altiplano on a west-vergent thrust system, northern Chile, *J. South Am. Earth. Sci.*, *9*, 171–181.
- Müller, R., W. Roest, J. Royer, L. Gahagan, and J. Sclater (1997), Digital isochrons of the world's ocean floor, *J. Geophys. Res.*, *102*, 3211–3214.
- Nuanmin, P., O. Kulhanek, and L. Person (2005), Spatial and temporal b value anomalies preceding the devastating off coastal of NW Sumatra earthquake of December 26, 2004, *Geophys. Res. Lett.*, *32*(L11307), doi: 10.1029/2005GL022679.
- Oncken, O., D. Hindle, J. Kley, K. Elger, P. Victor, and K. Schemmann (2006), *The Andes*, chap. Deformation of the Central Andean Upper Plate System -facts, fiction, and constraints for plateau models, p. 569, *Frontiers in Earth Sciences*, Springer-Verlag, Berlin Heidelberg.
- Ossandón, G., R. Fréaud, L. Gustafson, D. Lindsay, and M. Zentilli (2001), Geology of the Chuquicamata mine: A progress report, *Econ. Geol.*, *96*(249-270).
- Pardo-Casas, F., and P. Molnar (1987), Relative motion of the Nazca (Farallón) and South American plates since late Cretaceous time, *Tectonics*, *6*, 233–248.
- Parotidis, M., E. Rothert, and S. Shapiro (2003), Pore-pressure diffusion: A possible mechanism for the earthquake swarms 2000 in Volcanland/NW Bohemia, central Europe, *Geophys. Res. Lett.*, *30*(2075), doi: 10.1029/2003GL018110.
- Patzwahl, R., J. Mechie, A. Schulze, and P. Giese (1999), 2D velocity models of the Nazca plate subduction zone between 19.5°S and 25°S from wide-angle seismic measurements during the Cinca'95 project, *J. Geophys. Res.*, *104*(B4), 7293–7317.
- Peyrat, S., J. Campos, J. Chabalier, A. Pérez, S. Bonvalot, M.-P. Bouin, D. Legrand, A. Nercessian, O. Charade, G. Patau, E. Clévéde, E. Kausel, P. Bernard, and J.-P. Vilotte (2006), Tarapacá intermediate-depth earthquake (Mw 7.7, 2005, northern Chile): A slab-pull event with horizontal fault plane constrained from seismologic and geodetic observations, *Geophys. Res. Lett.*, *33*(L22308).
- Pilger, R. (1981), Plate reconstruction, aseismic ridges, and low-angle subduction beneath the Andes, *Bull. Geol. Soc. Am.*, *92*, 448–456.

- Pilger, R. (1983), Kinematics of the South American subduction zone from global plate reconstructions. Geodynamics of the Eastern Pacific Region, Caribbean and Scotia Arcs, *Am. Geophys. Union, Geodyn. Ser. 9*, 113–126.
- Podvin, P., and I. Lecomte (1991), Finite difference computations of traveltimes in very contrasted velocity models: a massively parallel approach and its associated tools, *Geophys. J. Int.*, *105*, 271–284.
- Ramos, V. (1988), *Processes in Continental Lithospheric Deformation*, vol. 218, chap. The tectonics of the central Andes: 30° to 33°S latitude, pp. 31–54, Spec. Pap. Geol. Soc. Am.
- Ramos, V. (1999), Plate tectonic setting of the Andean Cordillera, *Episodes*, *22*(3), 183–190.
- Ramos, V., E. Cristallini, and D. Pérez (2002), The Pampean flat-slab of the Central Andes, *J. South Am. Earth Sci.*, *15*, 59–78.
- Reasenberg, P. (1985), Second-order moment of central California seismicity, 1969–1982, *J. Geophys. Res.*, *90*, 5479–5495.
- Reutter, K.-J., P. Giese, J. Götze, E. Scheuber, K. Schwab, G. Schwarz, and P. Wigger (1988), *The Southern Central Andes, Notes Earth Sci.*, vol. 17, chap. Structure and crustal development of the central Andes between 21° and 25°S, pp. 231–261, Springer, New York.
- Reutter, K.-J., E. Scheuber, and D. Helmcke (1991), Structural evidence of orogen-parallel strike slip displacements in the Precordillera of northern Chile, *Geologische Rundschau*, *80*, 135–153.
- Reutter, K.-J., R. Döbel, T. Bogdanic, and J. Kley (1994), *Tectonics of the Southern Central Andes*, chap. Geological map of the central Andes between 20°S and 26°S, Springer Verlag, Berlin Heidelberg.
- Reutter, K.-J., E. Scheuber, and G. Chong (1996), The Precordilleran fault system of Chuquicamata, Northern Chile: evidence for reversals along arc-parallel strike-slip faults, *Tectonophysics*, *259*, 213–228.
- Rietbrock, A., and F. Waldhauser (2004), A narrowly spaced double-seismic zone in the subducting Nazca plate, *Geophys. Res. Lett.*, *31*(L10608), doi: 10.1029/2004GL019610.
- Riller, U., and O. Oncken (2002), Growth of the central andean plateau by tectonic segmentation is controlled by the gradient in crustal shortening, *J. Geology*, *3*, 367–384.

- Riller, U., L. Petronovic, L. Ramelow, L. Greskowiak, M. Strecker, and O. Oncken (2001), Late cenozoic tectonism, caldera and plateau formation in the central Andes, *Earth Planet. Sci. Lett.*, *188*, 299–311.
- Rivera, L., and A. Cisternas (1990), Stress tensor and fault plane solutions for a population of earthquakes, *Bull. Seismol. Soc. Am.*, *80*, 600–614.
- Roeder, D. (1988), Andean-age structure of eastern cordillera (province of la paz, bolivia), *Tectonics*, *7*, 23–39.
- Roessler, D., F. Krueger, and G. Ruempker (2007), Inversion for seismic moment tensors in anisotropic media using standard techniques for isotropic media, *Geophys. J. Int.*, *169*, 136–148.
- Rutland, R. (1971), Andean orogeny and sea floor spreading, *Nature*, *233*, 252–255.
- Scheuber, E., and K.-J. Reutter (1992), Magmatic arc tectonics in the Central Andes between 21° and 25°S, *Tectonophysics*, *205*, 127–140.
- Scheuber, E., T. Bogdanic, A. Jensen, and K.-J. Reutter (1994), *Tectonics of the Southern Central Andes*, chap. Tectonic development of the North Chilean Andes in relation to plate convergence and magmatism since Jurassic, pp. 121–139, Springer-Verlag, New York.
- Scheuber, E., D. Mertmann, H. Ege, P. Silva, C. Heubeck, K.-J. Reutter, and V. Jacobshagen (2006), *The Andes*, chap. Exhumation and basin development related to formation of the central Andean plateau, 21°S, p. 569, *Frontiers in Earth Sciences*, Springer-Verlag, Berlin Heidelberg.
- Schilling, F., G. Partzsch, H. Brasse, and G. Schwarz (1997), Partial melting below the magmatic arc in the Central Andes deduced from geoelectromagnetics field experiments and laboratory data, *Phys. Earth Planet. Inter.*, *103*(1-2), 17–31.
- Schmitz, M. (1994), A balanced model of the southern central Andes, *Tectonics*, *13*, 484–492.
- Schmitz, M., K. Lessel, P. Giese, P. Wigger, M. Araneda, J. Bribach, F. Graeber, S. Grunewald, C. Haberland, S. Lueth, P. Roewer, T. Ryberg, and A. Schulze (1999), The crustal structure beneath the Central Andean fore-arc and magmatic arc as derived from seismic studies—the PISCO 94 experiment in northern Chile (21° – 23°), *J. South Am. Sci.*, *12*, 237–260.

- Scholz, C. (1968), The frequency-magnitude relation of microfracturing in rock and its relation to earthquakes, *Bull. Seism. Soc. Am.*, *58*, 399–415.
- Schorlemmer, D., and S. Wiemer (2005), Microseismicity data forecast rupture area, *Nature*, *434*, 1086.
- Schorlemmer, D., S. Wiemer, and M. Wyss (2005), Variation in earthquake-size distribution across different stress regimes, *Nature*, *437*(22), 539–542, doi:10.1038/nature 04094.
- Schurr, B. (2000), Seismic structure of the central andean subduction zone from local earthquake data, *Tech. Rep. STR01/01*, GeoForschungsZentrum Potsdam, Potsdam-Germany, 125 pp.
- Schurr, B., G. Asch, Rietbrock, R. Kind, M. Pardo, B. Heit, and T. Monfret (1999), Seismicity and average velocities beneath the argentine puna plateau, *Geophys. Res. Lett.*, *26*, 3025–3028.
- Schurr, B., G. Asch, A. Rietbrock, R. Trumbull, and C. Haberland (2003), Complex patterns of fluid and melt transport in the central Andean subduction zone revealed by attenuation tomography, *Earth Planet. Sci. Lett.*, *215*, 105–119.
- Sempere, T., G. Hérail, J. Oller, and M. Bonhomme (1990), Late Oligocene-early Miocene major tectonic crisis and related basins in Bolivia, *Geology*, *18*, 946–949.
- Sempere, T., R. Butler, D. Richards, L. Marshall, W. Sharp, and C. Swisher (1997), Stratigraphy and chronology of upper Cretaceous-lower Paleogene strata in Bolivia and northwest Argentina, *Geol. Soc. Am. Bull.*, *109*, 709–727.
- SERNAGEOMIN (2003), *Mapa Geológico de Chile, CD-ROM versión 1.0*, vol. 4, publicación geológica digital ed., Servicio Nacional de Geología y Minería, Santiago-Chile.
- Shapiro, S., E. Huenges, and G. Borm (1997), Estimating the crust permeability from fluid-injection-induced seismic emission at the KTB site, *Geophys. J. Int.*, *131*, F15–F18.
- Sheffels, B. (1990), Lower bound on the amount of crustal shortening in the central Bolivian Andes, *Geology*, *18*, 812–815.

- Sileny, J., P. Campus, and G. Panza (1996), Seismic moment tensor resolution by waveform inversion of a few local noisy records-i. synthetic test, *Geophys. J. Int.*, *126*, 605–619.
- Singh, S., R. Apsel, J. Fried, and J. Brune (1982), Spectral attenuation of sh-waves along the imperial fault, *Bull. Seism. Soc. Am.*, *72*, 2003–2016.
- Snoke, J. A. (2003), *International Handbook of Earthquake and Engineering Seismology*, chap. FOCMEC: FOCal MECHANism determinations, 85.12, Academic Press, San Diego-USA.
- Sobolev, S., A. Babeyko, I. Koulakov, and O. Oncken (2006), *The Andes*, chap. Mechanism of the Andean Orogeny: Insight from Numerical Modeling, p. 569, *Frontiers in Earth Sciences*, Springer-Verlag, Berlin Heidelberg.
- Sokos, E., and J. Zahradník (2008), ISOLA a Fortran code and Matlab GUI to perform multiple-point source inversion of seismic data, *Computers and Geosciences*, *34*, 967–977, doi:10.1016/j.cageo.2007.07.005.
- Somoza, R. (1998), Updated Nazca (Farallon) – South America relative motions during the last 40 my: Implications for mountain building in the central Andean region, *J. S. Am. Earth Sci.*, *11*(3), 211–215.
- Springer, M. (1999), Interpretation of heat-flow density in the Central Andes, *Tectonophysics*, *306*, 377–395.
- Stein, S., and M. Wysession (2003), *An introduction to seismology, earthquakes, and earth structure*, Blackwell.
- Sylvester, A. (1988), Strike-slip faults, *Geol. Soc. Am. Bull.*, *100*, 1666–1703.
- Tarantola, A. (1987), *Inverse Problem Theory: Methods for Data Fitting and Model Parameter Estimation*, Elsevier, Amsterdam.
- Tarantola, A., and B. Valette (1982), Inverse problems=quest for information, *J. Geophys.*, *50*, 159–170.
- Tassara, A. (2005), Interaction between the Nazca and South American plates and formation of the Altiplano-Puna plateau: Review of a flexural analysis along the Andean margin (15°–34°S), *Tectonophysics*, *399*, 39–57.
- Tassara, A., C. Swain, R. Hackney, and K. J. (2007), Elastic thickness structure of south america estimated using wavelets and satellite-derived gravity data, *Earth Planet. Sci. Lett.*, *253*, 17–36.

- Tibaldi, A., C. Corazzato, and A. Rovida (2008), Miocene-quaternary structural evolution of the uyuni-atacama region, andes of chile and bolivia, *Tectonophysics*, doi:10.1016/j.tecto.2008.09.011.
- Tomlinson, A., and N. Blanco (1997a), Structural evolution and displacement history of the west fault system, Precordillera, Chile: Part 1, synmineral history, in *Actas 8th Congreso Geológico Chileno*, vol. 3, pp. 1883–1887, Antofagasta.
- Tomlinson, A., and N. Blanco (1997b), Structural evolution and displacement history of the west fault system, Precordillera, Chile: Part 2, postmineral history, in *Actas 8th Congreso Geológico Chileno*, vol. 3, pp. 1878–1882, Antofagasta.
- Vavrycuk, V. (2007), On the retrieval of moment tensors from borehole data, *Geophys. Prospect.*, 55, 381–391.
- Victor, P., O. Oncken, and J. Glodny (2004), Uplift of the western Altiplano plateau: Evidence from the Precordillera between 20° and 21°S (northern Chile), *Tectonics*, 23(TC4004), doi:10.1029/2003TC001519.
- von Huene, R., W. Weinrebe, and F. Heeren (1999), Subduction erosion along the North Chile margin, *Geodynamics*, 27, 345–358.
- Warren, N., and G. Latham (1970), An experiment study of thermal induced microfracturing and its relation to volcanic seismicity, *J. Geophys. Res.*, 75(4455-4464).
- Weaver, B., and J. Tarney (1984), Empirical approach to estimating the composition of the continental crust, *Nature*, 310, 575–577.
- Wesnousky, S. . (1994), The Gutenberg-Richter or characteristic earthquake distribution, which is it?, *Bull. Seism. Soc. Am.*, 86(6), 1940–1959.
- Whitman, D., B. Isacks, and S. Kay (1996), Lithospheric structure and along-strike segmentation of the central Andes Plateau: Seismic Q, magmatism, flexure, topography and tectonics, *Tectonophysics*, 259, 29–40.
- Wigger, P., J. Araneda, P. Giese, W.-D. Heinsohn, P. Röwer, M. Schmitz, and J. Viramonte (), The crustal structure along the Central Andean Transect derived from seismic refraction investigations, in *Global Geoscience Transect 6*, edited by H.-J. Götze and O. Omarini, ICL and AGU.

- Wigger, P., M. Schmitz, M. Aranedá, G. Asch, S. Baldzuhn, W.-D. H. P. Giese, E. Martínez, E. Ricardi, P. Röwer, and J. Viramonte (1994), *Tectonics of the Southern Central Andes*, chap. Variation of the crustal structure of the Southern Central Andes deduced from seismic refraction investigations, pp. 23–48, Springer Verlag, Berlin-Heidelberg.
- Wigger, P., J. Kummerow, P. Salazar, G. Asch, and D. Moser (2007), Microseismicity in the West Fissure fault system, Northern Chile, *Geophysical Research Abstracts*, 9(07136).
- Wittlinger, G., G. Herquel, and T. Nakache (1993), Earthquake location in strongly heterogeneous media, *Geophys. J. Int.*, 115, 759–777.
- Woodcock, N. (1986), The role of strike-slip fault systems at plate boundaries, *Philos. Trans. Royal Soc. London Abstracts*, 317, 13–29.
- Wörmer, G., K. Hammerschmidt, F. Henjes-Kunst, J. Lezaun, and H. Wilke (2000), Geochronology (Ar-Ar, K-Ar and He-exposure ages) of Cenozoic magmatic rocks from northern Chile (18–22°S): implications for magmatism and tectonic evolution of the central Andes, *Revista Geológica de Chile*, 27(2), 205.
- Yamashita, T. (1999), Pore creation due to fault slip in a fluid-permeated fault zone and its effect on seismicity: Generation mechanism of earthquake swarm, *Pure Appl. Geophys.*, 155, 625–647.
- Yoon, M., S. Buske, S. Lüth, A. Schulze, S. Shapiro, M. Stiller, and P. Wigger (2003), Along-strike variations of crustal reflectivity related to the Andean subduction process, *Geophys. Res. Lett.*, 30(4), doi: 10.1029/2002GL015848.
- Yoon, M., S. Buske, S. Shapiro, and P. Wigger (2009), Reflection Image Spectroscopy across the Andean subduction zone, *Tectonophysics*, 472, 51–61.
- Yuan, X., S. Sobolev, R. Kind, O. Oncken, and Andes Seismology Group (2000), New constraints on subduction and collision processes in the central andes from p-to-s converted seismic phases, *Nature*, 408, 958–961.
- Yuan, X., S. Sobolev, and R. Kind (2002), Moho topography in the Central Andes and its geodynamic implications, *Earth Planet. Sci. Lett.*, 199, 389–402.

- Yunga, S., A. Lutikov, and O. Molchanov (2005), Non-double-couple seismic sources, faults interaction and hypothesis of self-organized critically, *Nat. Hazards Earth Syst. Sci.*, *5*, 11–15.
- Zahradnik, J., A. Serpetsidaki, E. Sokos, and G.-A. Tselentis (2005), Iterative deconvolution of regional waveform and double-event interpretation of the 2003 Lefkada earthquake, Greece, *Bull. Seismol. Soc. Am.*, *95*, 159–172.
- Zandt, G., S. Beck, S. Ruppert, C. Ammons, D. Rock, E. Minaya, T. Wallace, and P. Silver (1996), Anomalous crust of the bolivian altiplano, central andes: Constraints from broadband regional seismic waveforms, *Geophys. Res. Lett.*, *23*, 1159–1162.
- Zoback, M., and H.-P. Harjes (1997), Injection-induced earthquakes and crustal stress at 9 km depth at the KTB deep drilling site, Germany, *J. Geophys. Res.*, *102*(B8), 18,477–18,491.

Appendix A

Focal mechanisms parameters

A.1 Events used in the stress tensor analysis

Table A.1: List of 228 focal mechanisms used in the stress tensor analysis

date	time	sec	latitude	longitude	depth	mag.	strike	dip	rake
yyyymmdd	hhmm	[s]	[°]	[°]	[m]	M_L	[°]	[°]	[°]
2005 1109	2020	33.5	-20.664	-68.887	6.2	1.8	150	80	35
2005 1109	2032	45.2	-20.667	-68.887	6.2	2.1	148	86	34
2005 1111	0919	25.9	-21.175	-69.184	33.6	2.2	343	62	11
2005 1111	1724	2.1	-21.253	-68.418	116.1	2.1	315	79	19
2005 1114	0730	42.7	-20.759	-68.821	3.9	0.7	118	55	3
2005 1119	2356	58.1	-20.938	-68.962	6.9	0.9	261	41	-20
2005 1120	0726	16.8	-20.937	-68.958	6.3	0.3	277	53	-36
2005 1122	2316	18.9	-20.749	-68.975	5.9	0.9	132	52	-26
2005 1126	0201	38.2	-20.802	-69.298	8.7	1.4	311	79	-32
2005 1126	0222	2.8	-20.801	-69.295	8.4	1.5	311	79	-32
2005 1126	0608	57.3	-20.811	-69.293	10.1	0.9	306	71	-35
2005 1128	0535	0.6	-20.856	-68.887	6.0	0.7	126	65	38
2005 1206	0545	14.7	-20.765	-69.210	18.1	1.4	167	23	-39
2005 1206	1736	13.5	-20.730	-68.767	1.6	1.2	51	90	88
2005 1214	0008	50.1	-20.832	-69.077	12.8	1.5	187	23	-86
2005 1223	0816	6.4	-20.664	-69.215	28.7	1.8	132	66	-60
2005 1224	1204	14.5	-20.769	-68.749	1.1	1.0	54	67	-31
2006 0302	1208	40.1	-20.748	-69.002	7.5	0.2	95	85	29
2006 0302	1213	18.2	-21.189	-69.196	30.6	1.2	325	33	-38
2006 0313	0602	34.8	-20.820	-69.156	12.1	1.5	293	65	-36
2006 0314	1631	9.8	-20.635	-69.164	3.2	1.5	285	53	7
2006 0320	0042	18.5	-20.755	-68.734	1.3	0.1	103	89	-82

Continued on the next page

date	time	sec	latitude	longitude	depth	mag.	strike	dip	rake
yyyymmdd	hhmm	[s]	[°]	[°]	[m]	M_L	[°]	[°]	[°]
2006 0320	0427	0.7	-20.793	-69.076	1.1	0.0	99	74	19
2006 0320	2149	3.5	-20.743	-68.828	4.9	1.0	278	83	-7
2006 0321	1146	42.4	-21.007	-68.725	1.0	0.4	106	89	-6
2006 0325	1223	26.5	-20.782	-68.947	5.5	0.8	116	85	32
2006 0327	0523	59.1	-20.896	-69.646	56.9	5.8	41	73	11
2006 0401	0054	26.7	-20.802	-68.951	7.4	0.7	276	86	-28
2006 0401	0310	43.9	-20.803	-68.952	7.5	0.5	105	54	39
2006 0401	0505	35.7	-20.803	-68.952	7.2	0.3	86	58	35
2006 0401	0517	28.0	-20.804	-68.952	7.3	0.5	103	82	28
2006 0401	0521	15.0	-20.806	-68.943	7.0	0.7	92	57	40
2006 0401	0545	21.5	-20.803	-68.950	7.5	0.7	260	59	-8
2006 0401	0550	56.4	-20.804	-68.950	7.0	0.4	280	89	-29
2006 0401	0642	12.9	-20.802	-68.954	7.1	0.2	294	64	2
2006 0401	0645	16.8	-20.803	-68.951	7.4	1.1	92	57	38
2006 0401	0733	53.5	-20.802	-68.950	7.6	0.6	102	84	28
2006 0401	0854	1.9	-20.803	-68.953	7.9	1.4	235	58	-44
2006 0401	0953	43.8	-20.804	-68.954	7.9	1.5	105	78	24
2006 0401	1018	10.8	-20.803	-68.952	7.4	0.6	102	83	29
2006 0401	1353	40.6	-20.801	-68.952	7.5	0.8	90	68	15
2006 0401	1435	57.6	-20.802	-68.953	8.2	2.1	102	56	36
2006 0401	1442	55.8	-20.806	-68.957	6.9	0.3	109	65	75
2006 0401	1553	20.4	-20.803	-68.954	8.2	3.5	99	62	42
2006 0401	1554	45.4	-20.802	-68.950	7.4	1.4	268	82	-33
2006 0401	1555	57.9	-20.802	-68.952	7.3	0.6	103	61	42
2006 0401	1559	19.6	-20.803	-68.954	8.1	3.1	85	66	43
2006 0401	1601	24.4	-20.799	-68.952	9.7	3.0	100	80	27
2006 0401	1602	38.1	-20.802	-68.950	7.4	1.8	98	64	39
2006 0401	1603	38.0	-20.802	-68.954	8.2	1.4	278	82	-37
2006 0401	1605	25.0	-20.802	-68.953	8.3	1.8	102	55	36
2006 0401	1606	1.9	-20.803	-68.955	8.1	2.0	88	67	40
2006 0401	1612	53.3	-20.803	-68.955	8.1	1.1	266	88	-31
2006 0401	1613	33.5	-20.803	-68.957	7.5	2.1	267	84	-34
2006 0401	1621	7.3	-20.802	-68.954	8.6	1.2	108	71	36
2006 0401	1627	40.9	-20.802	-68.951	8.6	0.9	254	65	-36
2006 0401	1628	44.4	-20.803	-68.953	7.6	0.8	85	58	26
2006 0401	1640	2.1	-20.802	-68.953	7.4	0.7	101	55	35
2006 0401	1739	18.1	-20.804	-68.951	7.8	0.7	130	74	37
2006 0401	1740	14.6	-20.803	-68.956	7.4	1.3	105	58	42
2006 0401	1810	18.7	-20.803	-68.956	8.2	2.7	265	89	-31
2006 0401	1816	47.4	-20.801	-68.954	7.4	0.6	78	55	37
2006 0401	1828	18.7	-20.803	-68.954	7.2	0.8	86	57	28

Continued on the next page

date	time	sec	latitude	longitude	depth	mag.	strike	dip	rake
yyyymmdd	hhmm	[s]	[°]	[°]	[m]	M_L	[°]	[°]	[°]
2006 0401	1833	27.3	-20.799	-68.952	7.7	0.7	120	54	35
2006 0401	1852	7.9	-20.802	-68.953	8.3	2.1	84	71	37
2006 0401	1901	1.9	-20.803	-68.952	7.3	0.6	71	51	-27
2006 0401	1901	58.0	-20.801	-68.952	7.6	0.6	107	74	35
2006 0401	1902	37.4	-20.801	-68.949	7.3	0.3	105	82	33
2006 0401	2202	5.6	-20.782	-68.906	6.7	0.4	286	76	-30
2006 0401	2213	23.7	-20.803	-68.951	7.3	0.3	98	55	40
2006 0401	2244	10.2	-20.802	-68.949	7.8	0.8	277	83	-36
2006 0401	2301	20.3	-20.796	-68.948	8.2	0.2	294	76	-34
2006 0401	2305	8.1	-20.802	-68.952	7.3	0.8	96	62	37
2006 0401	2310	25.8	-20.805	-68.955	7.7	0.1	264	62	4
2006 0402	0033	7.9	-20.805	-68.944	6.7	0.0	74	54	37
2006 0402	0042	41.1	-20.796	-68.954	9.9	0.3	272	89	-27
2006 0402	0051	32.0	-20.796	-68.954	10.2	0.6	90	60	19
2006 0402	0119	53.9	-20.798	-68.955	9.8	0.3	106	57	34
2006 0402	0131	3.2	-20.798	-68.954	9.4	0.6	269	60	14
2006 0402	0322	46.4	-20.795	-68.948	10.4	0.1	267	36	69
2006 0402	0323	53.0	-20.799	-68.954	9.8	0.5	250	86	-33
2006 0402	0328	54.2	-20.798	-68.954	9.7	0.6	272	89	-27
2006 0402	0403	59.2	-20.798	-68.954	9.9	1.3	274	87	-27
2006 0402	0414	7.5	-20.798	-68.954	9.7	0.3	116	80	-9
2006 0402	0511	59.5	-20.797	-68.953	9.7	1.4	109	64	38
2006 0402	0718	17.9	-20.797	-68.959	9.8	0.2	90	90	30
2006 0402	0719	52.7	-20.798	-68.954	9.3	0.2	274	86	-28
2006 0402	0846	32.2	-20.799	-68.954	9.8	0.8	87	59	33
2006 0402	1139	31.4	-20.796	-68.956	8.7	0.1	238	36	14
2006 0402	1208	30.4	-20.798	-68.952	9.7	0.6	114	57	32
2006 0402	1215	55.0	-20.798	-68.951	9.9	1.0	103	85	20
2006 0402	1217	7.4	-20.798	-68.955	9.2	0.5	88	56	23
2006 0402	1222	1.8	-20.799	-68.952	9.3	0.5	244	73	-25
2006 0402	1225	52.3	-20.798	-68.952	9.8	1.3	116	55	34
2006 0402	1608	14.9	-20.799	-68.953	9.8	2.8	273	76	-24
2006 0402	1653	54.0	-20.798	-68.953	10.0	2.1	275	79	-22
2006 0402	2311	13.6	-20.798	-68.952	10.0	2.2	105	77	24
2006 0402	2314	21.9	-20.798	-68.952	9.9	1.9	268	76	-28
2006 0402	2354	16.2	-20.803	-68.951	7.4	0.3	76	55	36
2006 0403	0001	7.3	-20.804	-68.943	9.7	0.1	216	78	33
2006 0403	0120	27.4	-20.798	-68.953	9.6	0.3	89	62	3
2006 0403	0231	20.1	-20.797	-68.956	9.8	0.2	248	62	-41
2006 0403	0306	28.7	-20.798	-68.955	9.7	0.6	205	32	-76
2006 0403	0834	48.6	-20.799	-68.954	9.5	0.3	101	57	39

Continued on the next page

date	time	sec	latitude	longitude	depth	mag.	strike	dip	rake
yyyymmdd	hhmm	[s]	[°]	[°]	[m]	M_L	[°]	[°]	[°]
2006 0404	0230	41.2	-20.798	-68.953	9.8	0.2	150	29	69
2006 0404	0620	46.3	-20.798	-68.954	9.7	1.3	106	65	39
2006 0404	0640	43.7	-20.798	-68.953	9.7	0.3	300	79	-7
2006 0404	1052	46.9	-20.797	-68.953	9.8	0.5	119	53	35
2006 0404	1101	59.0	-20.798	-68.951	9.7	0.1	107	71	35
2006 0404	1852	51.0	-20.799	-68.956	9.7	1.1	9	67	-81
2006 0405	0413	29.8	-20.797	-68.953	9.9	1.6	105	59	41
2006 0405	0428	13.0	-20.799	-68.953	9.8	0.3	259	36	69
2006 0405	0539	22.4	-20.799	-68.953	9.6	1.4	274	86	-28
2006 0406	0547	25.4	-20.799	-68.954	9.5	0.1	262	62	33
2006 0406	0931	38.0	-20.798	-68.952	9.8	1.1	88	67	9
2006 0407	0043	31.5	-20.797	-68.953	9.8	0.8	110	62	38
2006 0407	0259	52.1	-20.798	-68.952	9.6	2.7	108	55	32
2006 0407	0300	39.4	-20.797	-68.951	9.7	1.6	81	75	-23
2006 0407	0301	38.6	-20.797	-68.952	9.7	1.6	116	55	33
2006 0407	0416	27.0	-20.801	-68.950	7.4	0.9	97	61	40
2006 0407	0417	41.5	-20.802	-68.950	7.4	0.8	270	84	-34
2006 0407	1105	40.7	-20.797	-68.952	9.7	0.7	110	61	39
2006 0407	1115	36.0	-20.798	-68.952	9.6	0.9	105	60	39
2006 0407	1208	10.5	-20.798	-68.953	9.6	0.5	91	58	40
2006 0409	0848	50.6	-20.798	-68.952	9.7	0.5	100	64	36
2006 0410	0023	4.3	-20.798	-68.953	9.8	0.6	274	88	-27
2006 0410	0822	40.3	-20.798	-68.952	9.6	0.6	100	61	40
2006 0410	0848	25.1	-20.759	-68.763	4.8	0.3	140	70	83
2006 0410	0943	51.6	-20.798	-68.951	9.8	0.5	120	53	36
2006 0410	0946	27.0	-20.798	-68.954	9.7	1.5	105	60	39
2006 0410	0946	45.2	-20.797	-68.952	9.8	0.8	77	58	39
2006 0410	1647	19.2	-20.798	-68.954	9.6	1.7	105	64	38
2006 0410	1722	34.0	-20.799	-68.955	9.6	1.6	105	57	34
2006 0410	2056	7.0	-20.965	-69.642	6.4	1.6	274	80	-38
2006 0411	1202	2.0	-20.782	-68.724	3.0	0.7	77	56	-36
2006 0411	2229	57.7	-20.983	-69.646	8.0	1.9	259	72	-69
2006 0412	2346	35.1	-20.797	-68.952	9.8	0.1	112	63	40
2006 0413	0241	43.8	-20.882	-69.085	12.9	0.3	63	65	-78
2006 0413	0440	58.0	-20.797	-68.954	9.9	0.5	101	66	39
2006 0416	1154	40.5	-20.798	-68.954	9.6	0.9	90	60	12
2006 0416	2326	26.9	-20.637	-68.809	7.2	0.6	3	20	-86
2006 0418	0045	46.7	-20.798	-68.953	9.7	1.3	115	57	33
2006 0421	2244	3.9	-20.841	-69.142	14.9	1.9	302	58	-31
2006 0422	2225	5.0	-20.797	-68.953	9.9	2.1	105	57	40
2006 0422	2226	25.1	-20.797	-68.952	9.8	1.1	104	57	40

Continued on the next page

date	time	sec	latitude	longitude	depth	mag.	strike	dip	rake
yyyymmdd	hhmm	[s]	[°]	[°]	[m]	M_L	[°]	[°]	[°]
2006 0422	2234	21.1	-20.801	-68.953	8.5	1.5	106	55	42
2006 0428	2108	46.7	-20.799	-68.954	9.7	1.0	267	64	17
2006 0429	2046	44.7	-21.019	-68.771	7.1	2.6	147	57	-28
2006 0430	1234	19.6	-20.993	-68.617	1.1	1.9	189	55	-22
2006 0430	1657	35.0	-21.012	-68.786	1.1	2.2	165	60	-38
2006 0501	0438	51.7	-21.200	-69.189	35.5	0.7	158	48	65
2006 0501	2218	20.2	-20.838	-69.163	17.0	1.2	291	57	-32
2006 0504	0448	10.6	-21.217	-69.208	34.5	1.5	62	64	-54
2006 0507	2212	32.9	-21.345	-69.782	13.3	2.0	251	74	-38
2006 0508	1703	15.8	-21.025	-69.411	46.9	2.0	343	65	-1
2006 0509	0032	9.9	-20.781	-68.787	5.0	0.6	208	62	-48
2006 0509	0659	31.2	-20.782	-68.791	4.4	1.3	58	53	-27
2006 0509	0712	29.6	-20.779	-68.786	5.8	0.5	210	68	-46
2006 0509	1306	10.6	-20.781	-68.789	4.9	0.6	129	70	89
2006 0512	2246	16.0	-20.867	-68.709	3.1	0.7	109	58	-32
2006 0513	1417	30.4	-20.739	-69.099	14.8	3.8	123	64	39
2006 0629	0203	41.0	-20.779	-68.786	5.7	0.5	289	55	-44
2006 0629	2129	36.6	-21.277	-68.826	6.2	1.2	316	54	37
2006 0629	2255	2.1	-20.764	-69.002	8.7	0.0	96	75	42
2006 0630	0702	41.3	-20.779	-68.587	17.8	0.6	193	63	32
2006 0702	0209	49.1	-20.850	-68.754	6.2	0.4	119	58	7
2006 0702	2253	32.0	-21.278	-68.828	7.5	1.4	341	72	41
2006 0702	2346	49.0	-21.256	-68.851	9.6	0.4	269	56	10
2006 0704	0142	24.7	-20.779	-68.789	5.2	-0.2	281	49	-52
2006 0704	1248	53.6	-21.184	-69.183	36.1	0.8	182	47	40
2006 0704	2144	7.1	-20.778	-68.786	5.5	0.5	267	17	49
2006 0704	2305	7.8	-20.776	-68.790	5.5	0.0	165	66	44
2006 0705	0356	36.2	-20.776	-68.792	5.4	-0.3	201	54	-31
2006 0705	0556	5.8	-20.790	-68.811	0.0	0.2	17	49	83
2006 0707	1157	44.5	-20.779	-68.788	4.9	-0.3	106	63	-41
2006 0707	1209	44.9	-20.798	-68.954	9.9	1.0	97	57	37
2006 0707	1616	51.6	-21.278	-68.825	6.2	1.2	336	76	36
2006 0707	2243	42.0	-21.282	-68.840	7.4	0.2	265	50	3
2006 0709	1346	55.7	-20.792	-68.806	0.2	-0.3	71	74	-29
2006 0713	0809	14.6	-21.188	-68.787	3.6	-0.2	352	30	57
2006 0715	1132	35.0	-21.205	-69.192	36.0	1.0	168	55	19
2006 0715	1821	30.4	-20.727	-69.129	15.5	1.4	117	64	40
2006 0716	1337	7.0	-20.558	-69.066	10.3	0.5	90	84	85
2006 0718	2252	13.6	-21.201	-69.199	34.6	0.4	316	60	3
2006 0719	1640	43.4	-20.503	-68.982	8.0	0.7	140	71	36
2006 0721	1945	56.9	-21.278	-68.823	5.0	0.9	335	75	36

Continued on the next page

date	time	sec	latitude	longitude	depth	mag.	strike	dip	rake
yyyymmdd	hhmm	[s]	[°]	[°]	[m]	M_L	[°]	[°]	[°]
2006 0721	2256	13.2	-21.205	-69.193	36.0	1.1	189	40	81
2006 0722	0925	40.9	-20.811	-68.820	0.5	-0.1	182	31	88
2006 0723	1215	54.3	-20.850	-68.753	6.3	1.3	118	58	1
2006 0723	1216	49.5	-20.848	-68.751	6.5	0.4	91	72	-1
2006 0724	0820	39.4	-20.772	-68.748	3.8	-0.4	103	71	-32
2006 0725	0740	54.3	-21.242	-69.115	24.9	0.4	322	56	41
2006 0725	2132	53.1	-21.188	-69.169	34.5	0.9	5	66	26
2006 0726	1418	25.0	-20.779	-68.751	1.0	0.3	283	65	81
2006 0727	0503	43.6	-20.776	-68.753	1.0	0.1	246	37	-87
2006 0728	0244	39.5	-20.783	-68.767	0.6	-0.3	121	83	-5
2006 0728	1859	53.7	-20.933	-68.728	2.3	1.7	237	72	-87
2006 0729	0959	13.7	-20.781	-68.755	1.0	1.7	206	25	-89
2006 0729	1118	20.4	-20.782	-68.766	1.0	0.2	107	84	-37
2006 0729	1300	4.3	-20.786	-68.779	0.2	0.0	291	41	76
2006 0729	1441	44.2	-20.782	-68.758	1.1	0.6	113	70	-3
2006 0730	0845	19.3	-20.778	-68.762	1.3	-0.3	308	53	-32
2006 0730	0938	9.2	-20.779	-68.754	1.0	0.9	283	71	-2
2006 0801	0204	38.4	-20.782	-68.787	1.1	0.4	110	54	-9
2006 0802	1034	54.2	-20.800	-68.797	1.0	0.5	19	51	89
2006 0802	1554	26.1	-20.889	-68.896	1.6	-0.1	149	54	-19
2006 0803	0516	33.0	-21.177	-69.133	36.4	1.7	307	64	-5
2006 0804	0654	28.3	-21.181	-69.162	33.9	0.4	318	57	43
2006 0804	0836	11.9	-20.781	-68.757	1.0	0.2	120	49	87
2006 0804	0844	8.2	-20.607	-69.113	3.2	0.5	340	66	-36
2006 0804	1133	46.9	-20.481	-69.188	20.8	1.3	123	71	41
2006 0804	2255	14.3	-21.180	-69.169	33.0	0.7	62	66	-49
2006 0806	1337	12.6	-21.230	-68.834	8.0	0.3	316	57	40
2006 0808	0949	49.7	-20.812	-68.800	1.0	-0.6	289	81	0
2006 0808	1421	38.5	-21.001	-69.137	11.6	1.0	328	67	83
2006 0808	2338	18.5	-21.240	-68.833	7.3	1.3	304	54	33
2006 0809	0946	42.6	-20.790	-68.793	1.1	-0.3	80	65	-20
2006 0810	0458	57.2	-20.768	-69.037	8.6	0.3	85	61	6
2006 0810	0524	8.7	-20.864	-68.598	3.3	0.4	311	10	-28
2006 0810	1907	24.2	-20.876	-68.589	1.4	0.9	252	60	19
2006 0812	0112	29.0	-20.870	-68.571	1.1	1.1	94	78	-25
2006 0814	0941	10.8	-20.806	-69.233	11.3	0.4	100	85	34
2006 0816	2156	37.1	-20.947	-68.722	1.5	0.1	114	59	3
2006 0816	2319	59.1	-20.813	-68.805	2.1	0.0	291	43	-6
2006 0817	0009	51.0	-20.812	-68.804	1.0	-0.5	163	52	35
2006 1011	1023	47.9	-21.187	-69.168	34.1	4.2	324	65	2
2006 1011	1027	6.6	-21.187	-69.163	34.4	1.2	167	56	43

Continued on the next page

date	time	sec	latitude	longitude	depth	mag.	strike	dip	rake
yyyymmdd	hhmm	[s]	[°]	[°]	[m]	M_L	[°]	[°]	[°]
2006 1011	1028	10.0	-21.187	-69.164	34.5	0.9	36	54	-63

Appendix B

Location parameters

B.1 Events used in the swarm analysis

Table B.1: List of 90 events used in the swarm analysis

date	hour	sec	lat	long	depth	mag.	mag.	Exp.
yymmdd	hhmm	ss.ss	[°]	[°]	[m]	M_L	M_W	M_0
2006 04 01	00 54	27.183375	-20.795949	-68.946626	9565.53	0.2	0.7	10.1
2006 04 01	03 10	44.391238	-20.795418	-68.946032	9614.16	-0.1	0.6	10.0
2006 04 01	05 05	36.129317	-20.795949	-68.946626	9614.16	-0.2	0.3	9.6
2006 04 01	05 17	28.508667	-20.795949	-68.946626	9614.16	0.1	0.6	9.9
2006 04 01	05 21	15.253922	-20.797012	-68.947815	9468.26	0.2	0.7	10.1
2006 04 01	05 45	22.016440	-20.796211	-68.946325	9638.48	0.2	0.8	10.3
2006 04 01	05 50	56.869209	-20.795156	-68.946333	9541.21	-0.1	0.3	9.6
2006 04 01	06 42	13.316878	-20.795426	-68.947228	9662.79	-0.2	0.2	9.5
2006 04 01	06 45	17.328464	-20.795945	-68.946027	9614.16	0.6	1.0	10.5
2006 04 01	07 33	54.029364	-20.795949	-68.946626	9516.9	0.1	0.6	10.0
2006 04 01	08 54	2.454905	-20.796477	-68.946622	9662.79	0.9	1.2	10.9
2006 04 01	09 53	44.314070	-20.795949	-68.946626	9711.43	1.0	1.2	10.9
2006 04 01	10 18	11.267694	-20.795953	-68.947224	9614.16	0.2	0.5	9.9
2006 04 01	13 53	41.046796	-20.795953	-68.947224	9662.79	0.3	0.7	10.1
2006 04 01	14 35	58.241113	-20.795949	-68.946626	9565.53	1.6	1.6	11.4
2006 04 01	14 42	56.275337	-20.795937	-68.944831	9516.9	-0.1	0.5	9.9
2006 04 01	15 53	21.026485	-20.796481	-68.947220	9614.16	3.0	2.6	12.9
2006 04 01	15 54	45.905844	-20.796477	-68.946622	9614.16	1.0	1.2	10.9
2006 04 01	15 55	58.376845	-20.795957	-68.947823	9565.53	0.1	0.8	10.2
2006 04 01	15 59	20.256484	-20.796219	-68.947522	9541.21	2.6	2.3	12.6
2006 04 01	16 01	24.989960	-20.795941	-68.945429	9516.9	2.5	2.3	12.5
2006 04 01	16 02	38.562896	-20.795941	-68.945429	9468.26	1.3	1.4	11.3

Continued on the next page

date	hour	sec	lat	long	depth	mag.	mag.	Exp.
yymmdd	hhmm	ss.ss	[°]	[°]	[m]	M_L	M_W	M_0
2006 04 01	16 03	38.605590	-20.795953	-68.947224	9662.79	0.9	1.4	11.1
2006 04 01	16 05	25.583702	-20.796211	-68.946325	9638.48	1.3	1.4	11.2
2006 04 01	16 06	2.436756	-20.796489	-68.948417	9711.43	1.5	1.6	11.5
2006 04 01	16 12	53.862066	-20.796489	-68.948417	9662.79	0.6	1.0	10.6
2006 04 01	16 13	34.026913	-20.796489	-68.948417	9614.16	1.6	1.6	11.5
2006 04 01	16 21	7.919397	-20.796211	-68.946325	9541.21	0.7	1.2	10.9
2006 04 01	16 27	41.540297	-20.795414	-68.945433	9371	0.5	1.0	10.5
2006 04 01	16 28	44.924173	-20.795961	-68.948421	9614.16	0.4	0.8	10.3
2006 04 01	16 40	2.618170	-20.795961	-68.948421	9614.16	0.2	0.9	10.5
2006 04 01	17 39	18.654132	-20.795426	-68.947228	9516.9	0.2	0.7	10.1
2006 04 01	17 40	15.127470	-20.795949	-68.946626	9516.9	0.8	1.1	10.8
2006 04 01	18 10	19.348120	-20.795961	-68.948421	9711.43	2.2	2.0	12.1
2006 04 01	18 28	19.200276	-20.795969	-68.949618	9419.63	0.3	0.9	10.4
2006 04 01	18 52	8.499577	-20.796203	-68.945128	9443.94	1.6	1.6	11.5
2006 04 01	19 01	2.354203	-20.795961	-68.948421	9516.9	0.1	0.6	10.0
2006 04 01	19 01	58.496701	-20.795961	-68.948421	9614.16	0.1	0.8	10.2
2006 04 01	19 02	37.900482	-20.795933	-68.944232	9419.63	-0.2	0.4	9.6
2006 04 01	22 02	5.314251	-20.797004	-68.946618	9565.53	-0.1	0.5	9.9
2006 04 01	22 13	24.208739	-20.795949	-68.946626	9419.63	-0.2	0.4	9.7
2006 04 01	23 01	20.769338	-20.795977	-68.950815	9711.43	-0.2	0.4	9.7
2006 04 01	23 05	8.564558	-20.795957	-68.947823	9516.9	0.3	0.7	10.2
2006 04 01	23 10	26.352312	-20.795949	-68.946626	9565.53	-0.3	0.4	9.7
2006 04 02	00 33	8.192251	-20.796489	-68.948417	9419.63	-0.4	0.5	9.8
2006 04 02	00 42	41.589753	-20.795961	-68.948421	10197.8	-0.1	0.4	9.7
2006 04 02	00 51	32.507135	-20.797405	-68.947363	9966.75	0.1	0.6	9.9
2006 04 02	01 31	3.677474	-20.797266	-68.946317	10027.5	0.1	0.5	9.9
2006 04 02	03 22	46.901533	-20.795961	-68.948421	9857.32	-0.4	0.3	9.6
2006 04 02	03 23	53.633122	-20.796227	-68.948719	9541.21	0.0	0.4	9.6
2006 04 02	04 14	7.977806	-20.795973	-68.950217	9905.96	-0.2	0.2	9.4
2006 04 02	07 18	18.477211	-20.796243	-68.951112	9833.01	-0.3	0.2	9.4
2006 04 02	07 19	53.127391	-20.796517	-68.952606	9662.79	-0.3	0.1	9.3
2006 04 02	11 39	31.803462	-20.796493	-68.949016	9711.43	-0.4	0.1	9.2
2006 04 02	23 54	16.741631	-20.796473	-68.946023	9468.26	-0.2	0.3	9.6
2006 04 03	02 31	20.564556	-20.796505	-68.950811	9857.32	-0.4	0.3	9.5
2006 04 03	13 59	25.252863	-20.796742	-68.946919	9881.64	-0.2	0.3	9.5
2006 04 03	21 07	52.904946	-20.795418	-68.946032	9711.43	0.2	0.7	10.1
2006 04 04	02 30	41.684631	-20.794946	-68.954414	9565.53	-0.4	0.1	9.3
2006 04 04	06 20	46.899545	-20.796485	-68.947819	9516.9	0.8	1.0	10.6
2006 04 04	06 40	44.250533	-20.794902	-68.947831	9565.53	-0.2	0.4	9.6
2006 04 04	10 52	47.474631	-20.796219	-68.947522	9346.68	0.0	0.5	9.8
2006 04 04	11 01	59.470251	-20.796251	-68.952309	9638.48	-0.3	0.1	9.3

Continued on the next page

date	hour	sec	lat	long	depth	mag.	mag.	Exp.
yymmdd	hhmm	ss.ss	[°]	[°]	[m]	M_L	M_W	M_0
2006 04 04	18 52	51.521477	-20.795961	-68.948421	9711.43	0.6	0.9	10.4
2006 04 05	04 13	30.366501	-20.796485	-68.947819	9516.9	1.1	1.2	10.9
2006 04 05	04 28	13.599832	-20.795957	-68.947823	9614.16	-0.2	0.4	9.7
2006 04 05	05 39	22.920335	-20.796219	-68.947522	9638.48	0.9	1.0	10.6
2006 04 05	14 52	27.972316	-20.795426	-68.947228	9419.63	0.0	0.5	9.9
2006 04 06	05 47	25.879127	-20.796513	-68.952008	9857.32	-0.3	0.3	9.5
2006 04 06	09 31	38.601813	-20.795945	-68.946027	9468.26	0.7	0.9	10.5
2006 04 07	00 43	32.067264	-20.795957	-68.947823	9565.53	0.3	0.8	10.3
2006 04 07	02 59	52.657888	-20.796211	-68.946325	9443.94	2.2	1.8	11.7
2006 04 07	03 00	39.940094	-20.795953	-68.947224	9419.63	1.1	1.3	11.0
2006 04 07	03 01	39.222198	-20.795949	-68.946626	9468.26	1.1	1.3	11.0
2006 04 07	04 16	27.457697	-20.796211	-68.946325	9541.21	0.4	0.8	10.2
2006 04 07	04 17	42.019825	-20.795941	-68.945429	9419.63	0.3	0.6	10.0
2006 04 07	11 05	41.234443	-20.796481	-68.947220	9419.63	0.2	0.6	10.0
2006 04 07	11 15	36.637783	-20.795949	-68.946626	9419.63	0.4	0.8	10.2
2006 04 07	12 08	11.021569	-20.795422	-68.946630	9516.9	0.0	0.5	9.9
2006 04 09	08 48	51.173071	-20.796477	-68.946622	9468.26	0.0	0.6	10.0
2006 04 10	08 22	40.890091	-20.796227	-68.948719	9443.94	0.1	0.7	10.1
2006 04 10	09 43	52.136575	-20.795961	-68.948421	9468.26	0.0	0.6	9.9
2006 04 10	09 46	27.602187	-20.796219	-68.947522	9541.21	0.9	1.1	10.7
2006 04 10	09 46	45.704192	-20.797556	-68.950205	9808.69	0.3	0.7	10.1
2006 04 10	16 47	19.734317	-20.796489	-68.948417	9565.53	1.2	1.3	11.1
2006 04 10	17 22	34.607830	-20.796485	-68.947819	9614.16	1.0	1.2	10.9
2006 04 11	23 57	55.096224	-20.796489	-68.948417	9565.53	0.1	0.6	9.9
2006 04 12	23 46	35.674872	-20.795961	-68.948421	9468.26	-0.4	0.2	9.4
2006 04 13	04 40	58.639968	-20.796493	-68.949016	9468.26	0.0	0.5	9.9
2006 04 16	11 54	41.027821	-20.796489	-68.948417	9468.26	0.4	0.7	10.2

B.2 Events used in the subcluster A analysis

Table B.2: List of 182 events used in the subcluster A analysis

date	hour	sec	lat	long	depth	mag.	mag.	Exp.
yymmdd	hhmm	ss.ss	[°]	[°]	[m]	M_L	M_W	M_0
2006 01 06	00 04	2.234648	-21.229496	-69.204409	34757.3	0.9	1.1	10.8
2006 03 02	12 13	17.779575	-21.242126	-69.198932	34562.8	0.7	1.1	10.7
2006 05 04	04 48	11.020218	-21.246926	-69.209108	32860.6	0.9	1.4	11.1
2006 07 04	12 48	53.768546	-21.217983	-69.171768	36921.5	0.9	1.2	10.9
2006 07 18	22 52	13.812984	-21.237123	-69.200462	34392.6	0.4	0.9	10.4
2006 07 21	22 56	13.445039	-21.236741	-69.177956	36459.5	1.1	1.2	11.0
2006 07 25	21 32	53.051112	-21.220558	-69.160349	38040	0.7	1.1	10.8
2006 08 04	06 54	27.873458	-21.235398	-69.173462	36775.6	0.4	0.9	10.4
2006 08 04	22 55	13.830025	-21.234900	-69.178867	36143.4	0.7	1.1	10.7
2006 08 26	12 34	46.100624	-21.231434	-69.171986	37043.1	0.7	0.9	10.4
2006 09 12	11 20	22.692472	-21.230916	-69.173790	37189	0.7	1.1	10.8
2006 09 13	22 21	14.052656	-21.231140	-69.166286	37164.6	0.7	1.0	10.6
2006 09 14	11 45	31.527128	-21.230370	-69.170192	37091.7	0.9	1.1	10.7
2006 10 02	08 55	59.322992	-21.236984	-69.174053	37116	0.7	1.1	10.7
2006 10 04	23 54	21.437158	-21.233295	-69.174676	36775.6	0.8	1.2	10.9
2006 10 11	10 23	47.694624	-21.233550	-69.173173	36897.2	4.1	3.5	14.3
2006 10 11	10 27	6.381968	-21.236709	-69.171954	36799.9	1.2	1.5	11.3
2006 10 11	10 28	9.773764	-21.234599	-69.171967	37334.9	1.0	1.2	10.8
2006 10 11	10 34	13.552550	-21.237540	-69.179452	35900.2	0.1	0.7	10.2
2006 10 11	10 35	24.984223	-21.237514	-69.174650	36775.6	0.5	0.8	10.3
2006 10 11	10 36	29.912825	-21.234343	-69.173469	35316.6	0.3	0.6	10.0
2006 10 11	10 39	53.288250	-21.230628	-69.169290	35754.3	0.3	0.8	10.4
2006 10 11	10 54	25.686316	-21.233256	-69.167473	37553.7	0.8	1.0	10.7
2006 10 11	10 58	27.718879	-21.237514	-69.174650	36581.1	0.4	0.9	10.4
2006 10 11	10 59	11.720221	-21.234075	-69.172570	36897.2	1.6	1.6	11.5
2006 10 11	12 02	28.359533	-21.235379	-69.169861	36192	0.1	0.5	9.8
2006 10 11	12 12	24.463654	-21.236466	-69.175857	36678.3	0.6	1.1	10.7
2006 10 11	20 30	35.728106	-21.229389	-69.184003	36264.9	0.9	1.2	10.9
2006 10 12	00 31	27.626104	-21.234401	-69.184272	35997.5	0.3	1.1	10.7
2006 10 12	01 11	14.600034	-21.234337	-69.172268	36678.3	0.2	0.8	10.2
2006 10 12	02 09	22.159408	-21.241177	-69.169225	35948.8	0.2	0.5	9.9
2006 10 12	03 18	1.796902	-21.234369	-69.178270	35997.5	0.1	0.6	10.0
2006 10 12	05 09	37.972997	-21.247110	-69.193800	35122.1	0.2	0.8	10.3
2006 10 12	07 22	36.850050	-21.236485	-69.179458	36192	0.2	0.6	10.0
2006 10 13	06 47	12.606278	-21.227994	-69.169906	37164.6	0.8	1.1	10.7
2006 10 13	08 26	40.378807	-21.235398	-69.173462	36581.1	0.5	1.0	10.6

Continued on the next page

date	hour	sec	lat	long	depth	mag.	mag.	Exp.
yymmdd	hhmm	ss.ss	[°]	[°]	[m]	M_L	M_W	M_0
2006 10 13	09 37	21.202071	-21.220623	-69.172352	36678.3	0.1	0.8	10.3
2006 10 14	03 06	22.486626	-21.233275	-69.171074	36289.3	1.0	1.3	11.1
2006 10 14	08 15	23.226446	-21.226991	-69.179516	36386.5	0.3	0.6	9.9
2006 10 14	10 42	34.958778	-21.210048	-69.167616	37164.6	0.2	0.6	10.0
2006 10 15	10 09	27.719687	-21.228033	-69.177109	35997.5	0.4	0.7	10.2
2006 10 15	10 53	56.337656	-21.234369	-69.178270	36483.8	0.6	0.9	10.4
2006 10 15	21 12	22.137750	-21.230124	-69.173495	35802.9	0.7	1.1	10.8
2006 10 16	08 50	58.453412	-21.237770	-69.173148	36945.8	2.4	2.1	12.2
2006 10 16	10 37	34.920785	-21.232342	-69.193888	33954.9	0.3	0.9	10.4
2006 10 16	13 09	27.530464	-21.239656	-69.180639	35802.9	0.6	0.9	10.4
2006 10 16	23 35	16.916555	-21.237514	-69.174650	36775.6	1.4	1.4	11.2
2006 10 17	13 29	14.449774	-21.238569	-69.174643	36386.5	0.6	1.0	10.6
2006 10 18	03 22	41.676563	-21.229094	-69.178302	36483.8	0.3	0.6	10.0
2006 10 18	08 11	31.136386	-21.239637	-69.177038	36094.7	0.4	0.9	10.5
2006 10 18	10 45	29.363251	-21.225923	-69.177121	36386.5	0.4	0.8	10.3
2006 10 18	10 51	0.874870	-21.224325	-69.174130	36727	0.1	0.8	10.4
2006 10 18	12 54	51.830384	-21.237508	-69.173449	36678.3	1.0	1.2	10.8
2006 10 18	16 23	26.094201	-21.233288	-69.173475	36775.6	1.2	1.4	11.2
2006 10 18	23 20	9.943553	-21.234874	-69.174066	36727	0.6	1.0	10.5
2006 10 19	02 44	39.733041	-21.236459	-69.174656	36386.5	0.6	1.1	10.7
2006 10 19	04 17	29.142994	-21.234912	-69.181268	35754.3	0.2	0.6	10.0
2006 10 19	11 45	18.741542	-21.225930	-69.178322	36483.8	0.4	0.7	10.1
2006 10 19	12 43	15.982064	-21.221671	-69.171146	37164.6	0.2	0.5	9.9
2006 10 19	13 22	29.657217	-21.238301	-69.173745	36799.9	0.8	1.1	10.7
2006 10 19	22 48	16.906779	-21.239145	-69.183644	35754.3	0.4	0.8	10.3
2006 10 20	01 32	31.099999	-21.240711	-69.180633	35705.7	0.3	0.6	10.0
2006 10 20	08 26	17.027788	-21.224894	-69.181929	35802.9	0.2	0.3	9.6
2006 10 20	13 39	9.743930	-21.238317	-69.176746	36508.1	1.2	1.3	11.1
2006 10 20	23 36	14.930451	-21.239605	-69.171036	35997.5	0.6	1.0	10.6
2006 10 21	18 04	16.420938	-21.230667	-69.176492	36143.4	0.9	1.2	10.8
2006 10 22	00 14	0.960038	-21.242006	-69.176123	36264.9	0.6	1.0	10.6
2006 10 22	00 24	41.775600	-21.246017	-69.186603	35122.1	0.1	0.5	9.9
2006 10 23	01 16	6.775766	-21.234330	-69.171068	36775.6	0.2	0.8	10.4
2006 10 23	06 57	55.092847	-21.237501	-69.172249	36775.6	0.4	0.8	10.3
2006 10 23	10 22	45.151651	-21.234330	-69.171068	36386.5	0.6	0.9	10.4
2006 10 24	03 43	47.127026	-21.220079	-69.169355	37116	0.3	0.7	10.1
2006 10 24	06 25	7.927359	-21.224888	-69.180729	35511.1	0.1	0.6	10.0
2006 10 24	07 09	13.431812	-21.238569	-69.174643	36678.3	0.3	0.8	10.2
2006 10 24	11 28	55.492403	-21.236194	-69.174358	36848.5	1.1	1.4	11.1
2006 10 26	01 11	50.354450	-21.236984	-69.174053	36727	0.7	1.0	10.6
2006 10 26	07 50	58.603115	-21.236459	-69.174656	36483.8	0.5	0.9	10.5

Continued on the next page

date	hour	sec	lat	long	depth	mag.	mag.	Exp.
yymmdd	hhmm	ss.ss	[°]	[°]	[m]	M_L	M_W	M_0
2006 10 26	07 53	50.965358	-21.237508	-69.173449	36678.3	0.8	1.1	10.7
2006 10 26	12 57	35.454228	-21.236181	-69.171957	37189	0.9	1.3	11.0
2006 10 27	03 33	21.971460	-21.234330	-69.171068	36872.9	0.3	0.9	10.4
2006 10 28	06 30	46.106118	-21.238301	-69.173745	36799.9	1.3	1.4	11.2
2006 10 28	09 16	7.708780	-21.236466	-69.175857	36192	0.5	0.9	10.4
2006 10 28	12 40	8.058311	-21.235405	-69.174663	36678.3	0.5	0.9	10.5
2006 10 29	16 25	29.338521	-21.235372	-69.168661	38331.8	1.1	1.2	10.9
2006 10 29	22 51	34.142193	-21.236453	-69.173456	36678.3	1.2	1.4	11.2
2006 10 30	01 19	29.290107	-21.235385	-69.171061	37067.4	0.7	0.9	10.5
2006 10 31	18 29	16.263150	-21.235667	-69.174361	36410.8	1.1	1.1	10.7
2006 11 01	12 57	56.754774	-21.236485	-69.179458	35997.5	0.3	0.6	10.0
2006 11 05	08 02	47.329318	-21.238569	-69.174643	36581.1	0.5	0.9	10.5
2006 11 07	06 29	5.932518	-21.232214	-69.169880	36872.9	0.2	0.5	9.8
2006 11 07	22 56	17.462494	-21.240698	-69.178232	36678.3	0.3	0.9	10.4
2006 11 08	06 57	55.082241	-21.237009	-69.178855	35948.8	0.6	0.9	10.5
2006 11 10	00 05	21.153099	-21.232803	-69.181281	35754.3	0.3	0.6	10.0
2006 11 10	12 26	35.408369	-21.222739	-69.173540	36775.6	0.1	0.6	10.1
2006 11 10	13 01	9.287422	-21.238122	-69.189652	36824.2	0.8	1.1	10.8
2006 11 11	05 35	27.326528	-21.233544	-69.171973	36605.4	0.8	1.3	11.0
2006 11 11	06 36	57.909074	-21.234592	-69.170766	36994.4	1.5	1.5	11.4
2006 11 11	06 44	51.765884	-21.220623	-69.172352	36872.9	0.2	0.8	10.3
2006 11 11	07 50	58.646251	-21.234887	-69.176467	36337.9	0.4	0.8	10.3
2006 11 14	04 03	14.587955	-21.217970	-69.169368	37505.1	0.2	0.6	10.0
2006 11 14	09 32	21.804314	-21.233301	-69.175876	36386.5	0.4	0.8	10.3
2006 11 15	00 45	55.941219	-21.235385	-69.171061	36872.9	0.8	1.1	10.8
2006 11 15	08 22	57.186731	-21.234324	-69.169868	37261.9	1.0	1.2	10.9
2006 11 17	06 49	43.891293	-21.226907	-69.163911	37456.4	0.5	0.8	10.2
2006 11 17	22 13	11.549867	-21.232751	-69.171678	36727	0.4	1.0	10.5
2006 11 19	01 42	10.359986	-21.212203	-69.176005	37748.2	0.4	0.7	10.2
2006 11 20	01 07	8.543701	-21.236472	-69.177057	36386.5	0.3	0.8	10.3
2006 11 20	01 28	5.501089	-21.233301	-69.175876	36678.3	0.3	0.6	10.1
2006 11 21	04 13	42.891080	-21.239643	-69.178238	36094.7	0.2	0.8	10.3
2006 11 21	10 17	6.319585	-21.237521	-69.175850	36775.6	0.5	1.0	10.6
2006 11 22	04 37	7.375535	-21.230117	-69.172294	36872.9	0.3	0.5	9.9
2006 11 22	05 42	47.061046	-21.232278	-69.181884	36483.8	0.5	0.9	10.4
2006 11 22	09 18	33.595205	-21.228596	-69.183707	35754.3	0.3	0.7	10.1
2006 12 10	08 33	51.225759	-21.228234	-69.165403	37334.9	2.1	2.0	12.1
2006 12 12	04 44	22.593078	-21.228506	-69.166902	37116	0.6	1.1	10.7
2006 12 14	06 04	34.023605	-21.238582	-69.177044	35802.9	0.4	0.9	10.5
2006 12 16	03 23	0.774290	-21.232181	-69.163879	38331.8	1.0	1.2	10.9
2006 12 17	07 37	30.813656	-21.234298	-69.165066	36872.9	0.6	0.9	10.5

Continued on the next page

date	hour	sec	lat	long	depth	mag.	mag.	Exp.
yymmdd	hhmm	ss.ss	[°]	[°]	[m]	M_L	M_W	M_0
2006 12 21	02 56	17.109944	-21.233000	-69.168975	37772.6	2.1	2.0	12.1
2006 12 22	07 55	13.719878	-21.229056	-69.171100	37359.2	0.8	1.0	10.5
2006 12 23	02 39	50.590986	-21.237514	-69.174650	36386.5	0.7	1.2	10.9
2006 12 30	14 13	43.626181	-21.226153	-69.170818	37091.7	1.5	1.7	11.6
2007 01 04	01 46	23.459196	-21.236434	-69.169855	36581.1	0.7	1.0	10.6
2007 01 04	13 26	47.521644	-21.236919	-69.162049	36143.4	1.0	1.2	10.9
2007 01 04	14 33	23.975342	-21.226913	-69.165111	38137.3	1.8	1.8	11.8
2007 01 04	14 35	13.417462	-21.226638	-69.163012	37772.6	1.4	1.6	11.5
2007 01 09	09 48	44.892565	-21.242795	-69.175818	35802.9	0.3	0.8	10.2
2007 01 22	14 29	22.672480	-21.231408	-69.167184	37967.1	2.0	1.9	11.9
2007 01 24	02 44	3.090131	-21.233515	-69.166571	38210.3	1.2	1.4	11.2
2007 01 29	03 12	50.756522	-21.239081	-69.171639	36532.4	0.3	0.6	10.0
2007 02 03	17 24	2.850436	-21.245947	-69.173398	33857.6	0.9	1.3	11.1
2007 02 04	09 13	50.385748	-21.234324	-69.169868	37164.6	0.6	0.9	10.5
2007 02 13	01 22	56.722099	-21.229062	-69.172301	36192	0.6	1.3	11.0
2007 02 22	19 33	59.960705	-21.236165	-69.168956	37675.3	2.8	2.5	12.8
2007 02 22	22 31	31.285389	-21.235094	-69.165961	37723.9	1.7	1.7	11.7
2007 02 22	22 32	26.146257	-21.232981	-69.165374	37723.9	1.9	1.8	11.8
2007 02 22	22 35	47.043416	-21.238517	-69.165040	37359.2	1.0	1.2	10.9
2007 03 02	12 32	57.543839	-21.234045	-69.167168	37432.1	1.3	1.4	11.2
2007 03 03	12 12	19.138593	-21.232712	-69.164475	36921.5	0.7	1.0	10.7
2007 03 06	02 14	11.477995	-21.235638	-69.168959	37626.7	0.9	1.2	10.9
2007 03 06	03 00	41.014077	-21.234298	-69.165066	36775.6	0.8	1.0	10.6
2007 03 06	05 49	28.130765	-21.233249	-69.166273	37067.4	0.7	1.4	11.1
2007 03 11	18 51	4.517455	-21.234566	-69.165965	37723.9	1.5	1.5	11.3
2007 03 12	07 20	32.752022	-21.240627	-69.165027	37456.4	0.5	0.9	10.4
2007 03 13	09 40	2.598430	-21.240660	-69.171029	36581.1	1.3	1.5	11.3
2007 03 22	01 13	55.790784	-21.224522	-69.161825	38113	1.4	1.6	11.4
2007 03 26	00 48	43.938703	-21.246963	-69.166188	37164.6	0.4	0.5	9.8
2007 04 08	20 27	1.854290	-21.228253	-69.169004	37772.6	1.6	1.6	11.5
2007 04 13	08 56	57.451889	-21.249118	-69.174579	35997.5	0.3	0.6	10.0
2007 04 16	11 03	30.681447	-21.238517	-69.165040	35802.9	0.4	0.7	10.1
2007 04 17	08 59	19.514482	-21.230360	-69.168391	36945.8	1.5	1.6	11.5
2007 04 26	04 00	29.898378	-21.231153	-69.168687	37748.2	1.0	1.2	11.0
2007 05 01	13 10	3.356448	-21.245397	-69.169199	35754.3	0.7	1.2	10.9
2007 05 04	08 45	44.954519	-21.244892	-69.173404	35900.2	0.3	0.9	10.5
2007 05 16	09 28	55.223275	-21.233249	-69.166273	37845.5	0.9	1.3	11.0
2007 05 20	06 08	28.598863	-21.234029	-69.164167	37480.8	1.8	1.8	11.8
2007 05 20	11 36	45.644858	-21.231153	-69.168687	37359.2	0.9	1.2	10.9
2007 05 27	03 50	50.976486	-21.237443	-69.161445	37261.9	0.6	0.8	10.2
2007 05 29	06 00	55.815310	-21.241669	-69.162619	37456.4	0.8	1.0	10.6

Continued on the next page

date	hour	sec	lat	long	depth	mag.	mag.	Exp.
yymmdd	hhmm	ss.ss	[°]	[°]	[m]	M_L	M_W	M_0
2007 06 08	17 00	46.302981	-21.242743	-69.166214	36483.8	1.0	1.3	11.0
2007 08 13	13 07	35.301777	-21.235333	-69.161458	37651	1.1	1.3	11.1
2007 08 14	19 15	35.986969	-21.239585	-69.167434	35024.8	1.0	1.3	11.0
2007 08 20	13 31	53.673042	-21.240660	-69.171029	35705.7	0.7	1.1	10.7
2007 09 01	16 54	11.969830	-21.241203	-69.174027	36337.9	1.0	1.2	10.8
2007 09 11	18 34	20.450017	-21.233256	-69.167473	37748.2	1.9	1.9	11.9
2007 09 18	17 36	48.157725	-21.241676	-69.163820	37359.2	1.4	1.5	11.4
2007 09 22	01 49	44.662110	-21.240711	-69.180633	36094.7	0.5	0.8	10.3
2007 09 25	02 52	36.635719	-21.239592	-69.168635	36970.1	1.2	1.5	11.3
2007 10 12	12 07	14.777287	-21.244860	-69.167402	35413.9	0.6	1.0	10.6
2007 10 19	05 54	11.837855	-21.232466	-69.167778	38064.4	1.6	1.6	11.5
2007 10 19	06 17	19.757384	-21.233007	-69.170176	37189	1.4	1.5	11.4
2007 10 22	09 46	31.300322	-21.240608	-69.161425	37067.4	1.0	1.3	11.0
2007 10 24	01 14	47.225508	-21.234052	-69.168369	37578	1.1	1.3	11.0
2007 10 25	10 42	58.430260	-21.234062	-69.170169	36751.3	2.0	1.8	11.9
2007 11 22	17 08	21.142001	-21.240601	-69.160225	36581.1	0.9	1.2	10.9
2007 11 25	12 59	35.842387	-21.240647	-69.168628	35413.9	1.0	1.4	11.2
2007 12 21	05 21	38.097873	-21.227719	-69.167807	38210.3	1.4	1.5	11.3
2008 01 06	22 18	12.900021	-21.229849	-69.171396	37578	2.2	2.1	12.2
2008 01 09	04 05	9.183703	-21.242782	-69.173417	36094.7	0.7	1.1	10.7
2008 02 01	06 26	39.376018	-21.232188	-69.165079	37456.4	1.1	1.2	10.9
2008 03 04	12 58	18.366658	-21.234272	-69.160264	37845.5	1.3	1.5	11.3
2008 03 17	01 38	18.028644	-21.236945	-69.166850	37699.6	2.2	2.0	12.1

B.3 Events used in the subcluster A' analysis

Table B.3: List of 38 events used in the subcluster A' analysis

date	hour	sec	lat	long	depth	mag.
yymmdd	hhmm	ss.ss	[°]	[°]	[m]	M_L
20061019	11 18	23.409452	-21.241766	-69.180626	44848.6	0.9
20070124	08 24	55.853206	-21.247053	-69.182995	44556.8	0.4
20070424	05 13	16.073153	-21.244892	-69.173404	45626.8	0.7
20070427	11 48	48.751269	-21.258670	-69.185326	43584.2	0.7
20070427	23 54	40.141129	-21.255486	-69.181744	45335.0	0.3
20070515	22 46	32.270446	-21.247533	-69.173988	45091.8	0.6

Continued on the next page

date	hour	sec	lat	long	depth	mag.
yymmdd	hhmm	ss.ss	[°]	[°]	[m]	M_L
20070608	15 21	15.571087	-21.252328	-69.182963	44362.3	1.5
20070609	22 41	20.639914	-21.253318	-69.170952	44751.4	0.8
20070610	00 54	29.935455	-21.248070	-69.175786	45043.2	0.7
20070610	00 56	32.008948	-21.249125	-69.175779	44848.6	0.6
20070611	02 43	38.755921	-21.252283	-69.174560	45335.0	1.2
20070613	02 05	24.121426	-21.253351	-69.176954	44070.5	0.7
20070613	21 32	22.370739	-21.259706	-69.181718	44654.1	0.7
20070614	09 08	49.783858	-21.254354	-69.167343	44945.9	1.7
20070622	05 26	31.373280	-21.255473	-69.179343	45043.2	0.8
20070624	23 47	35.591509	-21.253913	-69.183554	44119.1	0.5
20070630	11 46	31.627630	-21.256522	-69.178136	44167.8	0.6
20070703	12 08	40.058827	-21.253849	-69.171549	44702.7	1.5
20070704	04 05	6.125373	-21.255473	-69.179343	44654.1	1.2
20070705	19 51	39.581522	-21.252276	-69.173359	45335.0	2.0
20070713	00 35	11.393137	-21.251176	-69.164962	44945.9	1.3
20070807	01 01	0.671634	-21.245953	-69.174598	45140.4	1.1
20070815	08 58	11.964625	-21.251241	-69.176967	43584.2	0.5
20070910	04 44	7.396119	-21.252302	-69.178161	45237.7	1.5
20071001	13 02	24.351917	-21.249092	-69.169777	44556.8	1.5
20071025	00 08	3.650016	-21.249226	-69.194988	44654.1	0.5
20071027	06 54	33.894737	-21.254476	-69.190154	44848.6	0.6
20071031	06 17	19.121515	-21.250192	-69.178174	45237.7	2.3
20071101	12 59	7.625820	-21.249157	-69.181782	45335.0	1.1
20071115	19 28	33.903628	-21.272478	-69.203254	42611.5	1.1
20071216	02 00	47.985081	-21.246005	-69.184202	45237.7	0.5
20071222	09 10	18.929242	-21.250205	-69.180575	45043.2	1.1
20080108	01 39	58.445406	-21.251292	-69.186572	45043.2	0.7
20080117	05 20	17.122557	-21.253414	-69.188960	44848.6	1.3
20080118	04 45	4.408543	-21.244905	-69.175805	45724.0	1.0
20080130	08 32	44.475006	-21.252315	-69.180562	44945.9	1.6
20080227	16 01	43.597345	-21.251241	-69.176967	45237.7	2.1
20080313	01 29	18.310591	-21.254444	-69.184151	45335.0	1.5

Appendix C

Acknowledgments

The first and foremost thanks go to Dr. Peter Wigger for accompanying this work, always giving his friendly support and who beside Dr. Guillermo Chong gave me the opportunity to come to Berlin and to know this little piece of paradise called Schlachtensee.

Special thanks to Prof. Dr. Serge Shapiro for opening the doors to the Geophysical Department of Freie Universität Berlin and for his time and dedication as referee of this thesis.

Particular thanks go to PD Dr. Günter Asch for serving as the co-referee, for his friendship and his very good advices about the instrumentation and maintenance of the seismological network.

Further appreciation go to my committee members Dr. Peter Wigger, Prof. Dr. Georg Kaufmann, PD Dr. Ekkehard Scheuber, Prof. Dr. Serge Shapiro and PD Dr. Günter Asch.

I am also thankful to Dr Jörn Kummerow who gave valuable help and guidance throughout this work and also read the entire manuscript.

I also want to thank Dr Bernd Schurr for his help in the moment tensor analysis.

I would like to thank to Lars Houpt for his friendship, advices given all these years and for his help in the translation of the abstract.

Many thanks to Juan Thomas for his help in the field campaigns in Northern Chile.

I want to thank the members of the Geophysical Department of the Freie Universität Berlin for their friendly hospitality in all these years.

I am grateful to my colleagues of the Geological Department and the authorities of the Universidad Católica del Norte for allowing me to study in Deutschland.

Very special thanks to my friends Daniel Chalbaud and Lis Torres for always be there and for open the doors of their home to Liey-si and me.

Muchísimas gracias!

To Daniel Diaz and Michelle Muñoz for their friendship and invitations to taste good Chilean food.

I like to thank to my family, especially to my parents for their love, support and understanding.

Last but not least, I want to thanks very specially to my wife Liey-si for her love, patience and for always be there when I needed her. Thanks my little Chinese girl!

This research was funded by the FU Berlin and by the Deutsche Forschungsgemeinschaft in the frame of the project “Physics and structure of subduction-induced geodynamic transients in terms of reflection seismic and micro-seismological signatures” (DFG SH 55/10-1). The personal financial support was through the Universidad Católica del Norte. The field campaigns were supported by the Geological Department of the Universidad Católica del Norte.

Appendix D

Curriculum Vitae

For reason of data protection,
the curriculum vitae is not included in the online
version

For reason of data protection,
the curriculum vitae is not included in the online
version

For reason of data protection,
the curriculum vitae is not included in the online
version